GRAPH-SPECTRAL TECHNIQUES FOR ANALYZING RESTING STATE FUNCTIONAL NEUROIMAGING DATA

Thesis submitted in partial fulfillment
of the requirements for the degree of

MS in CSE
by Research

by

SRINIVAS GOVINDA SURAMPUDI
201550821
GOVINDA.SURAMPUDI@RESEARCH.IIIT.AC.IN

International Institute of Information Technology
Hyderabad - 500 032, INDIA
SEPTEMBER 2018

International Institute of Information Technology
Hyderabad, India

CERTIFICATE

It is certified that the work contained in this thesis, titled "Graph-Spectral Techniques for Analyzing Resting State Functional Neuroimaging Data" by Srinivas Govinda Surampudi, has been carried out under my supervision and is not submitted elsewhere for a degree.

Date	Adviser: Dr. AVINASH SHARMA
Date	Co-Adviser: Dr. DIPANJAN ROY

To The Cause of All Causes

Acknowledgments

First and foremost, I deeply pay my obeisances to my mother, father and my dearest brother for their wholehearted love and attention for having trust in me and to allow me to pursue my dreams and keeping me lifted in all possible ways at all times. Since I was pursuing under-graduation, I have been supported by my parents. I was never technically, emotionally, and financially let down. I was fortunate to have home in the same city during my Masters making me comfortable to go home almost every weekend. I am glad to have so much caring grand-parents spending time with whom makes me rejoiced. Luckily being in Hyderabad made me acquainted with many of Uncles and Aunts. At times of no research progress interacting with their families has made me comfortable and sociable.

Next I show my gratitude towards my advisors, Dr. Avinash Sharma and Dr. Dipanjan roy, who went beyond just a mentor and played a fatherly role at IIIT-H and at NBRC Delhi. since I joined as a research assistant with Dr. Avinash Sharma, it has been adventurous every time. He has always been supportive inspite of many academically challenging situations. Even though he warned me of lack of funds in this thread, he somehow managed to provide me my monthly stipends. Coming to my co-advisor, I used to enjoy long hours yet motivating phone calls on the research problems I used to face. When my poster was accepted in BrainModes, Dr. Dipanjan took care of me at NBRC in all respects. I was surprised to see that he himself came to ensure that I am given a hostel accommodation that too late night. I really thank him to introduce me to Prof. Viktor Jirsa, Peter Robinson and Karl Friston.

Further I pay my special thanks to Prof. Bapi Raju for all the technical and informal discussions we had had during my Masters. I had been introduced to ever charming Prof. Bapi Raju after a semester. Since then, none of my meetings have gone without laughter. His keen technical insights have provided direction and his witty jokes have made research enjoyable. I used to call my advisors and Prof. Bapi any time in the day and night. I am very grateful to them not to throw any annoyance on me. Our meetings used to be for hours together and still there were so many points left out that made their way through phone calls. There came a time when we were better off at churning ideas and solutions while on phone!

When I joined CVIT, I was struggling with basic bash commands like ‘ls’ and ‘cd’. I pay my special thanks to my dearest friends Joyneel Misra, Abbhinav Venkat, Abhijeet Halwai, Sukesh Adiga, Chetan Srinidhi, Neeraj Battan, Karthik Gopinath and many others. Working, playing, hanging out, etc. with them has become a memorable time at IIIT-H. Along with them, ‘extra-research’ activities like swimming, badminton, table-tennis were enervating yet enjoyable. I cannot forget the guidance and assistance given be Shruti Naik starting from understanding the data, reading relevant papers and critical thinking. Pritish

Mohapatra has been the source to discuss all mathematical formulations. I extend my gratitude to my seniors Shruti Naik, Pritish Mohapatra, Saurabh Saini, Vijay Kumar, Saurabh Daptardar and all the lab members of CVIT and Cognitive Science if forgotten. All of the above have helped me out of their way to improve my knowledge base and skills.

During NIPS2016 at Barcelona, Dr. Dipanjan gave me a chance to meet Prof. Gustavo Deco at his office. I thank Prof. Deco to suggest me to look into the work of connectome harmonics, which resulted into my contributions. Prof. Viktor's comments have been beneficial in taking this work forward. He had attested the formulations and told that this work has a lot of potential in future. This gave me immense confidence. I received similar appreciations from Prof. Peter Robinson and Prof. Karl Friston at BrainModes2017 for which I am grateful to them.

I extend my gratitude to all the staff members of IIIT-H and NBRC for helping me in administrative and financial processes. Especially, R.S. Satyanarayan, Mahinder Reddy, Venu who ensured I am getting my regular stipend checks and other student benefits. Mutiyalu and other cleaning staff have been cooperative in keeping my table and surroundings always clean and tidy.

Abstract

Human brain is undoubtedly the most magnificent yet delicate arrangement of tissues. This serves as the seat of such a wide span of cognitive functions and behaviors. The neuronal activities within every neuron, collectively observed over network(s) of these interconnected neurons, manifest themselves into patterns at multiple scales of observations. Many brain imaging techniques such as fMRI, EEG, MEG etc. measure these patterns as electro-magnetic responses. These patterns supposedly play the role of unique neuronal signatures of the vast repertoire of cognitive functions. Experimentally, it is observed that different neuronal populations participate coherently to generate a signature for a cognitive function. These signatures could be investigated at the micro-scale corresponding to responses of individual neurons to external-current stimuli, at the meso-scale related to populations of neurons that show similar metabolic activities and in turn these populations, also known as regions of interest (ROIs), communicate via complex arrangement of anatomical fiber pathways leading to signatures at the macro-scale. The holy grail of neuroscience is thus to computationally decipher the interplay of this complex anatomical network and the complex functional patterns corresponding to the cognitive behaviors at various scales/levels.

Each scale of observation, depending on the instruments of measurement, has its own rich spatio-temporal dynamics that interacts with higher and lower levels in complex ways. Large-scale anatomical fiber pathways are represented in a matrix that accounts for inter-population fiber strength known as structural connectivity (SC) matrix. One of the popular modalities to capture large-scale functional dynamics is resting-state fMRI, and statistical dependence between these inter-population BOLD signals is captured in functional connectivity (FC) matrix. There are many models that provide computational accounts for the relationship between these two matrices as deciphering this relationship will provide the mechanism by which cognitive functions arise over the structure. On one hand, there are many non-linear dynamical models that describe the biological phenomenon well but are expensive and intractable. On the other hand there are linear models that compromise on the biological richness but are analytically feasible. This thesis is concerned with the analysis of the temporal dynamics of observed resting-state fMRI signals over the large-scale human cortex. We provide a model that has a bio-physical explanation as well as an analytical expression for FC given SC.

Reaction-diffusion systems provide a computational framework for the emergence of excitatory-inhibitory activities at the populations as reactions and their interactions as diffusion over space and time. The spatio-temporal dynamics of the BOLD signal governed by this framework is constrained with respect to the anatomical connections thereby separating the spatial and temporal dynamics. Covariance

matrix of this signal is estimated thus getting an estimate of the functional connectivity matrix. The covariance matrix or the BOLD signal in general is expressed in terms of the graph-diffusion-kernels thus forming an analytically elegant expression. Most importantly, the model for FC abstracts out biological details and works in the realm of spectral graph theoretic constructs providing the necessary ease for computational analysis. As this model learns the combination parameters of multiple diffusion kernels and kernels themselves, it is called Multiple Kernel Learning (MKL) model. Apart from superior quantitative performance, the model parameters may act as biomarkers for various cognitive studies.

Albeit, the model parameters are learned for a cohort, the model preserves subject-specificity. These parameters can be used as a measure for inter-group differences and dissimilarity identification as has been employed for age-group identification as an example in this thesis. Essentially MKL model partitions FC into two constituents: influence of the underlying anatomical structure into diffusion kernels and the cognitive theme of temporal structure into the model parameters, thus predicting FCs specific to subjects within the cognitive conditions of the cohort. Even though MKL is a cohort based model, it maintains sensitivity towards anatomy. Performance of the model drastically drops down with alterations in SC and model parameters, but does not overfit to the cohort.

Resting state fMRI BOLD signals have been observed to show non-stationary dynamics. Such multiple spatio-temporal patterns, represented as dynamic FC matrices, are observed to be cyclically repeating in time motivating use of a generic clustering scheme to identify latent states of dynamics. We propose a novel solution that learns parameters specific to the dynamic states using a graph-theoretic model (temporal-Multiple Kernel Learning, tMKL) and finally predicts the grand average FC of the unseen subjects by leveraging a state transition Markov model. We discover the underlying lower-dimensional manifold of the temporal structure which is further parameterized as a set of local density distributions, or latent transient states. tMKL thus learns a mapping between anatomical graph and the temporal structure. Unlike MKL, tMKL model obeys state-specific optimization formulation and yet performs at par or better than MKL for predicting the grand average FC. Like MKL, tMKL also shows sensitivity towards subject-specific anatomy. Finally, both tMKL and MKL models outperform the state-of-the-art in their own ways by providing bio-physical insights.

Contents

List of Figures

List of Tables

Chapter *1*

Introduction

1.1 The human brain

The human brain (see Figure 1.1[1]) is the central organ of the human nervous system. With the spinal cord, it forms the complete central nervous system. The brain is responsible for coordinating the entire body. It receives information from senses, integrates them, processes and then releases decisions to control all the activities in the body. The soft constituent tissues are contained and protected by the bones of the skull in the head. Grey matter neurons form the thin outer layer, also called cortex, of the brain responsible for major cognitive tasks. These neurons are connected by the neurons in the white matter. These neurons are long fibers that can connect thalamus region with cortex. These two tissues are placed inside the cerebrospinal fluid.

Neurons are arranged into groups or populations that are locally densely connected, and in turn these populations are globally sparsely connected. Neurons process information and communicate though this arrangement. This becomes key for the cognitive abilities of humans beings. In this arrangement, different populations specialize in their functional properties that are responsible for processing a kind of stimulus. Different brain areas communicate and coordinate their roles in successfully completing a higher-order task. A growing body of researchers is suggesting that the brain areas are anatomically well connected within themselves facilitating higher-order tasks.

1.2 Resting state activity

Functional Magnetic Resonance Imaging (fMRI) studies are based on blood oxygen level dependent (BOLD) signal which is very active even in the absence of any perceptible input. A vast majority of functional neuroscience studies focus on task-based inferences of the brain's functional organization. The blood oxygen level dependent (BOLD) signal is modulated based on the experimental variables and these changes are observable in specific regions thereby allowing inferences that can be related to brain's

[1] please go to this link https://www.youtube.com/watch?v=dAIQeTeMJ-I for a video of the same.

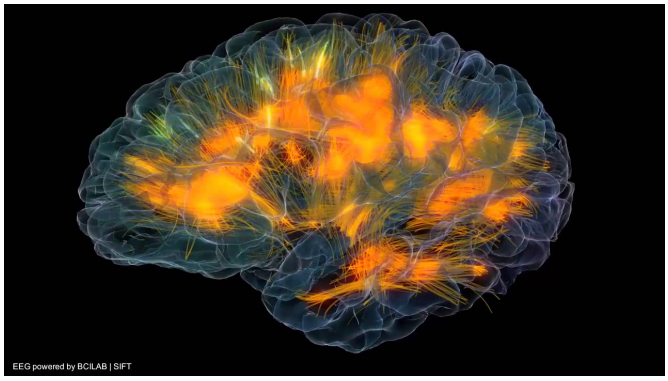

Figure 1.1: **The human brain**. The picture depicts a glass visualization of human brain replacing many of the biological details. The fibers seen carry neural information to the grey cells present on the outer layers of brain tissue. Adapted from https://www.youtube.com/watch?v=dAIQeTeMJ-IYoutube.

cognitive functions. Intriguingly, task-positive (and -negative) activations of regions are only less than 5% higher (and lower) in energies than spontaneous fluctuations in brain activity over those regions [42].

These spontaneous fluctuations were considered as 'noise' before a decade. Even though these signals are slow ($\leq$ 0.1 Hz) in nature, they consume upto 20% of body's energy [84, 71]. This spontaneous activity, which is not related to any task, is called *resting state activity* of the brain. When a participant is lying down with his eyes closed or fixated at a point without falling asleep, she is said to be in resting state. BOLD signals captured in such a state are called resting state fMRI signals. Many groups around the world have repeatedly reported that spontaneous activities of specific regions correlate in their signal variations. For example, left and right somatomotor cortices are functionally correlated with right medial cortex in the absence of any task [17]. Such empirical observations, one of them depicted in figure 1.2, have been suggesting that indeed this resting state activity has a well defined functional organization whose understanding and analysis would provide insights into functional topography of the brain.

After scanning, the raw data undergoes several pre-processing steps to isolate the spontaneous fluctuations from physiological parameters or in general non-neuronal noise sources [26]. After emphasizing on the neurobiologically meaningful BOLD signals, next step towards understanding this activity is to find spatial patterns of synchrony. In this regard, the simplest way is to look at how the regional activities correlate with each other, i.e forming a functional connectivity matrix and identifying communities within. A competitive method, known as independent component analysis (ICA) [102], finds spatial maps that are statistically independent of each other.

The topographical pattern of spontaneous activity is used to predict response of the participant in a task condition and/or disease states [30, 107, 41, 40]. In addition, it is also used to predict the quality of task preformance. Moreover, these spatial patterns may also predict the behavior of a participant. These spatial patterns are related to the temporal patterns originating from signals of frequencies less than 0.1Hz. In recent years it had been found that the spontaneous activity is not temporally consistent, it

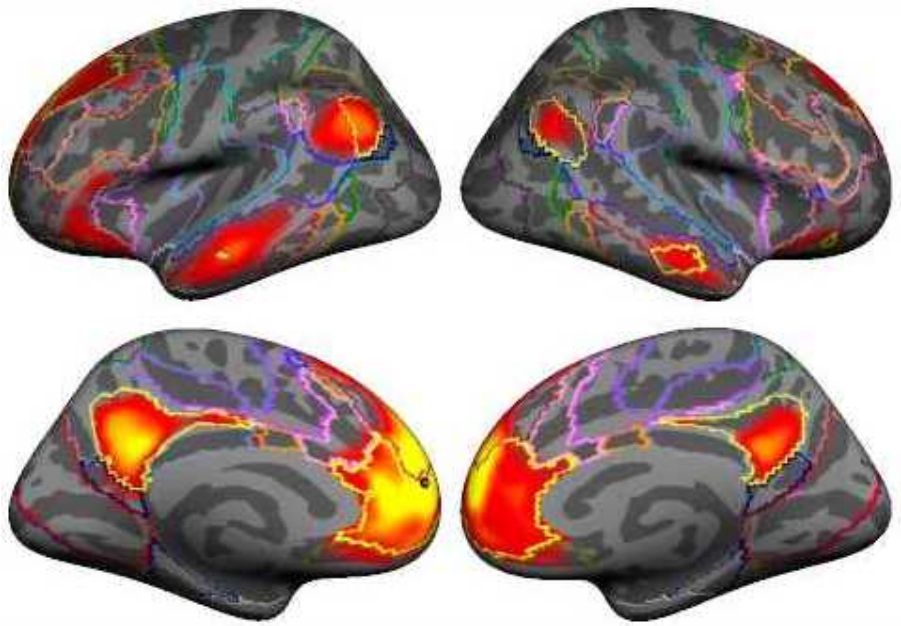

Figure 1.2: **Activities persistent in the human brain in the absence of any particular task**. Neural activities measured by fMRI at each voxel is depicted with color. The hotter(cooler) the color, the positive(negative) the activity value. Tremendous amount of topological synchronization of these resting state patterns is observed across the brain. Modified from [99].

shows non-stationary behavior [60, 61]. The spontaneous activity influences a participant's behavior in a task condition and vice versa [42].

A major bottleneck is interpreting this spontaneous activity. A natural question to ask is whether this activity is related to the structural connectivity. Studies show indeed it is so [29, 58], but the exact relations are still not understood. Regions that have no direct anatomical connection also show functional correlations. Studies have shown that it is better to segregate spontaneous activity into two layers [43]: one, occurring due to conscious mentation, and second, due to intrinsic activity which persists across different resting state conditions. Activity in the first layer may be considered as task-evoked modulations, and the activity in the second layer, underlying the first, is related to temporal fluctuations over the anatomical connections.

Apart from such conceptual layers of activities, an observation from imaging is that some regions are activated more at rest and de-activate themselves during a task-condition [93, 83]. This organization during rest was termed as default mode of brain function. This default mode, unique with respect to task conditions is considered to mediate necessary processes at rest, but there are other networks at rest which play their respective roles.

1.3 Diffusion MRI

There are many ways of capturing the structural human brain network; invasive technique such as tract tracing or non-invasive ones such as structural Magnetic Resonance Imaging (MRI), Diffusion Tensor Imaging (DTI) , Diffusion Spectrum Imaging (DSI), etc. Different brain tissues respond to the magnetic signals differently. This is the basis of any MRI scan. Structural MRI maps the 3-dimensional arrangement of structural subdivisions on the brain. Depending on the variations in the volume and/or surface area regional subdivisions, structural MRI allows inference of structural connectivity by correlating the region-specific volume sizes [55].

As the connections between the cortical neurons are provided by the white matter fibers, it becomes apt to measure the number and direction these fibers between two cortical regions. Brain tissue contains water molecules abundantly. Changes in the orientation of the magnetic signals does not change the direction of water molecules' movement much in the grey matter, but result significant changes in the white matter. In the grey matter, diffusion of water molecules is isometric, whereas that in the white matter it is dependent on the fiber orientation. In the direction of fibers, rate of diffusion will be maximum, thus becoming a viable measure for non-invasively tracing the white matter fibers [64, 11, 95, 63]. This phenomenon is called *diffusion anisotropy*. This technology, called *diffusion tensor imaging* (DTI), provides information about the direction of the fibers in each voxel. Instead of only one direction in a voxel, technology has improved to provide multiple directions by improving the angular resolution. These techniques are called q-ball [100], DSI [110] etc.

There are broadly two types of DTI technologies. Probabilistic DTI [12] provides a statistical estimate of the probable direction of the fiber, and deterministic DTI find optimal streamlines within the tensor field. Finally, after getting the estimates of fibers, between two voxels and /or large-scale regions density of the fibers connecting them is usually considered as the anatomical or structural connection, thus becoming an entry in the SC matrix [51]. DTI provides a symmetric weighted connectivity matrix and is often thresholded to get a binary pattern.

1.4 Network Science

1.4.1 Networks

In the contemporary period, the two fields of neuroscience and complex networks are merging together providing insights into both the fields that earlier was never possible. Over the last decade, with the increase of data, spread of the field of complex systems is seen evolving into many domains and hence linking them. The connectivity between the individual elements comes in many natural ways: through synapses between neurons, web hyper-links, co-author connections, etc. These connectivity patterns depict highly organized geometries of interactions between the elements. All these individual elements have their own specialized functions, but but the complexity of the phenomenon produced by their selective interactions is tremendous. Over this complex system lie the vast repertoire of functional

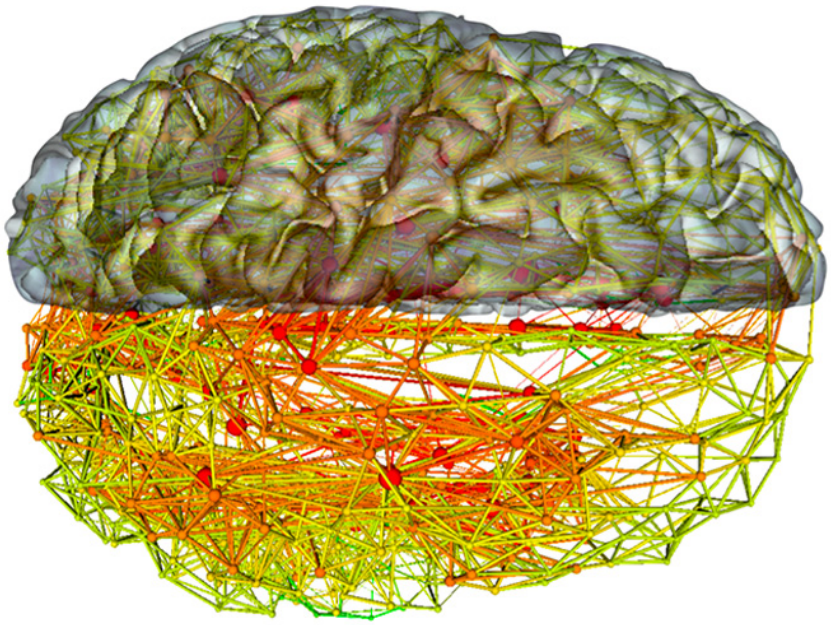

Figure 1.3: **From tissues to a network representation of a human brain**. Neural activities of millions of interconnected neurons can be efficiently described in terms of networks that are further mathematically treated to infer about the cognitive phenomena over this complex biological system. Each area of the brain, a region of interest, is a node in the network representation and the edges represent anatomical connections between them. Adapted from [103].

patterns resulting into cognition. All the cognitive functions displayed are possible because of interactions of individual neurons by a dense web of complex connectivity. This system of neuronal interactions is the seat of consciousness. Every system can be analyzed through multiple scales. Especially brain networks span from the micro-scale of cellular interactions through the large-scale functional interactions of regions to the macro-scale of cognitive systems. In the multi-scale analysis, no level operates in isolation, but in highly coordinated ways of inter-level dependence; both from the lower and higher levels. Dynamics happening at the cellular level travel above through these multi-scale interactions to manifest themselves as cognition and behavior.

Formally, the field of network science is expanding to study much larger systems and statistically characterize their structure and functional dynamics as shown in figure 1.3. Further this description can be used to predict global phenomenon over the network. The core mathematical field that studies such complex networks is called *graph theory*.

1.4.2 Brain Networks

As there are many modalities for observing the brain, there are these many ways for describing the brain connectivity [70]. The following are the three main connectivity representations of the brain:

- *Structural connectivity*, SC, is literally a 'wiring diagram' of the physical links present in the brain. These physical connections link the neural elements at multiple scales of observation; from single-cell connections to large-scale networks of interregional pathways. This patten is considered as relatively stable over short time periods of say few minutes but is *plastic* - changes the pattern - over few years. This information is captured from the dMRI modality.

- *Functional connectivity*, FC, captures the statistical dependence between the temporal measures of neural activities of two regions. The regions may be topologically very far from each other. The timeseries data is captured by non-invasive measures such as EEG, MEG, and fMRI. FC is highly time dependent and exhibits statistical non-stationarity. This matrix is measured using a symmetric measure, hence does not provide any causal relationships between the regions.

- *Effective connectivity*, EC, describes the effect on a region's activity due to another region's that may vary with time. There is no direct measure for estimating this matrix and can to come from generative models such as DCM [45] or through temporal ordering which model-free.

This thesis will be focusing on large-scale networks where nodes are the functionally grouped neural populations, also called *regions of interest* (ROI)s, and edges will be white matter fiber tracts connecting these ROIs in case of SC and correlation coefficient between the BOLD timeseries in case of FC.

1.5 Research Problem and Contributions

The holy grail in cognitive neuroscience is understanding how the static brain structure gives rise to dynamic function both during rest and task conditions. SC and FC matrices capture the above two parts and are generated from different modalities, hence necessitating a computational model that links the two matrices. Several models have been proposed to characterize the structure-function relationship [23, 77, 36, 104, 81]. Simple linear diffusion models [2, 89] as well as complex non-linear, whole-brain computational models [36] have been proposed. Linear graph models [2] admit closed form deterministic and testable solution to macroscopic interactions of brain activity without requiring any details of neural coding or their biophysical substrate. On the other hand nonlinear complex drift-diffusion models based on excitatory and inhibitory neuronal populations, though not analytically tractable, give rise to rich dynamics [36].

Research problem statement this thesis deals with is - '*relating the relatively static structural connectivity matrix to the functional connectivity dynamics obtained from the resting state fMRI time series*'. Primary contributions of this thesis are the following:

- *Model*: The model uniquely links SC to FC spectral graph theoretic constructs, especially combines multiple diffusion kernels, retaining subject-specificity in prediction of FC. The proposed model possesses the analytical beauty of linear models and yet is complex enough to capture the biological details.

- *Hypothesis*: We hypothesize that the presence of regional multi-scale co-activations that initiate diffusion would be necessary to bridge the gap between structurally confined diffusion phenomenon and empirically observed FC and that these co-activations would be common across the cohort.
- *Formulation*: We further provide a plausible mathematical reasoning for the existence of these co-activations along with diffusion kernels by linearizing a variant of reaction-diffusion model and extending it to generate FC. Moreover, we also describe a succinct multiple kernel learning (MKL) procedure to retrieve these co-activations by formulating it as an optimization problem.
- *Temporal dynamics*: The proposed model is also extended to characterize temporal non-stationarity and relates it to the underlying structure. The model discovers temporal topology and relates it to the structural topology.
- *Robustness*: Our detailed empirical results demonstrate the validity of the proposed model on a larger dataset. This is a generalized scheme that incorporates the existing large-scale diffusion models for characterizing temporal dynamics over SC.

1.6 Thesis Overview

The outline of the thesis is as follows. Next chapter provides the required background regarding the preprocessed data, and methods used. Chapter 3 introduces the notion of diffusion over a graph and motivation for combination of multiple diffusion kernels. Chapter 4 details out the multiple kernel learning (MKL) model, a vital contribution towards understanding the relationship between structure and function. Chapter 5 extends the MKL model to incorporate temporal dynamics. Finally chapter 6 summarizes the main contributions of the thesis and directs towards future investigations.

Chapter *2*

Background

This chapter introduces the reader to the basic concepts and the dataset used in the thesis.

2.1 Data Description and pre-processing

All participants were asked to give diagnostic psychiatric interviews in order to acquire comprehensive phenotypic information for the purpose of exploring brain/behavior relationship. We used the data comprising of 47 healthy participants (age: 18-80; mean: 41.55 years; 19 males) scanned at the Berlin Centre for Advanced Imaging, Charité University, Berlin, Germany. All participants gave written informed consent and the study was performed under compliance of laws and guidelines approved by the ethics committee of Charité University, Berlin. Participants did not show any sign of age-related neurodegenerative diseases under clinical testing procedures at the time of imaging. Details of preprocessing are mentioned in Vattikonda et al. [104].

2.1.1 Empirical DTI data and tractography

Images were taken with the following parameters: acquisition time=13:32, TR=10000ms, TE=91ms. Images have 64 diffusion directions with b_values=1000s/mm^2. DTI data was corrected for motion and eddy current, skull stripped, and fiber assignment was done using (FACT) algorithm [73]. Fractional anisotropy map was registered to MNI152 template. voxels were parcellated into 188 regions using Craddock's spectral clustering parcellations [27]. We downloaded data from the website whose details are in [20]. The empirical SC matrix of second dataset is generated by using an automated pipeline [90] for reconstruction of fiber tracks from T1 structural MR images and Diffusion-weighted images (DWI). Diffusion-Tensor-Imaging (TR 7500 ms, TE 86 ms, 61 transversal slices (2.0 mm), voxel size $2.3 \times 2.3 \times 2.3$ mm, FoV 220 mm, 96×96 matrix) and GRE field mapping (TR 674 ms, TE1 5.09 ms, TE2 7.55 ms, 61 transversal slices (2.3 mm), were measured directly after the anatomical scans. The images obtained from these scans are used as input to the reconstruction pipeline to generate the SC matrix for each subject (Please refer to [90] for a detailed outline of the pipeline for generating SC matrix). In

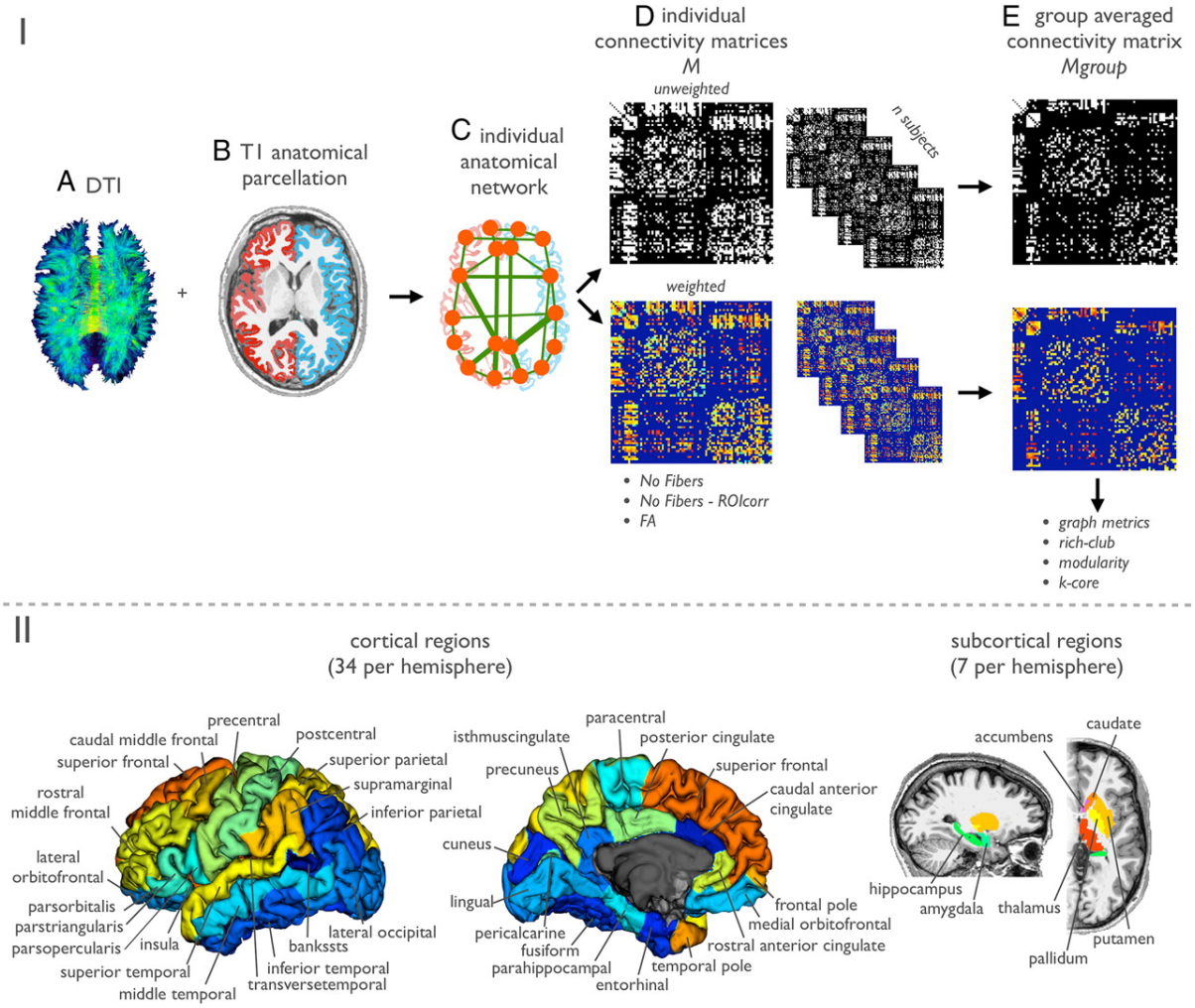

Figure 2.1: **Formation of structural connectivity matrix**. (I) Basic outline and the intermediate data files, after preprocessing, required for SC generation. Processed DTI data file is registered onto the subject's anatomical T1 image on which the tractograms are aggregated and collected into SC matrix. We only consider individual weighted SC matrices as the graph would possess more information. (II) The parcellation scheme used is known as Desikan Killiany atlas consisting of 34 cortical regions and 7 sub-cortical regions per hemisphere. The figure also consists of the names of all regions. Adapted from [103].

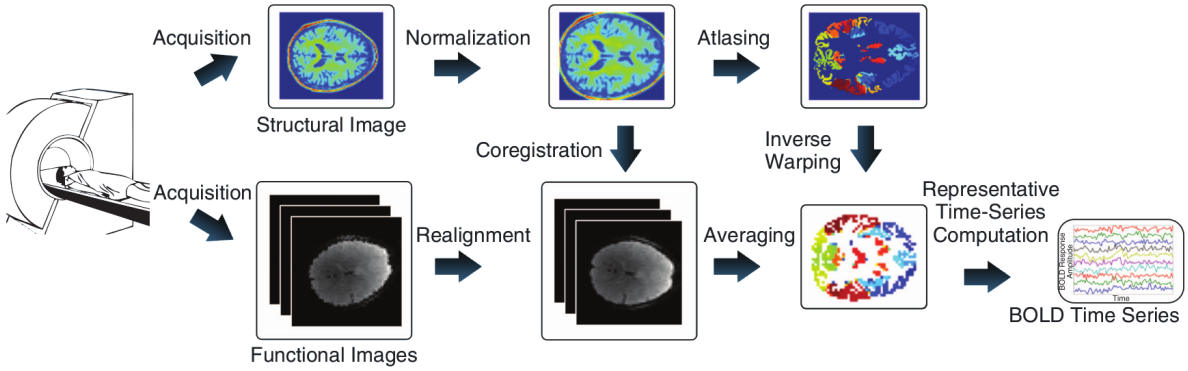

Figure 2.2: **An overview of the processing steps of raw fMRI data to BOLD time series**. From the scanner to collecting average BOLD time series of each individual region-of-interest, this pipeline gives an outline of the important steps. Modified from [85].

this pipeline, high resolution T1 anatomical images are used to create segmentation and parcellation of cortical and subcortical gray matter. For each subject, binary white matter(WM) masks were used to restrict tracking to WM voxels. dw-MRI data are pre-processed using FREESURFER after extracting gradient vectors and values (known as b-table) using MRTrix. Upon extraction of gradient vectors and values using MRTrix, dw-MRI data are pre-processed using FREESURFERs Using the registration rule created by FREESURFERs function dt-recon we transform the high-resolution mask volumes from the anatomical space to the subjects diffusion space, which will be used for fiber tracking. The cortical and subcortical parcellations contained in aparc+aseg.nii are resampled into diffusion space, one time using the original 1 mm isotropic voxel size (for subvoxel seeding) and one time matching that of our dw-MRI data, i.e., 2.3 mm isotropic voxel size. Based on that, a fractional anisotropy (FA) and an eigenvector map are computed and masked by the binary WM mask created previously. In order to improve existing methods for capacities estimation the approach makes use of several assumptions with regard to seed-ROI selection, tracking and aggregation of generated tracks [90]. Upon tractography the pipeline aggregates generated tracks to structural connectome. The normalized weighted distinct connection counts used here contain only distinct connections between each pair of regions yielding a symmetric matrix. Major preprocessed data files and the atlas used are depicted in figure 2.1.

2.1.2 Imaging Protocol and Functional Connectivity Matrices

Resting-state fMRI for the dataset was performed on a Siemens Trio 3T with acquisition time = 10:55, TR = 2500 ms, TE = 30 ms, on 38 slices with a voxel size = 3 mm3. fMRI data was slice time corrected, linearly registered, skull stripped, and spatially smoothed. All samples were registered to MNI152 atlas template. Residual BOLD data analyzed with the method elaborated in [27]. Time series of all pairwise ROIs were correlated to calculate FC matrix. Functional MRI and T1-weighted scans for second dataset were acquired using using a 3 Tesla Siemens Trim Trio MR scanner and a 12-channel Siemens head coil.

BOLD time-series were acquired at TR 1940 ms lasting 22 minutes (TE 30 ms, FA 78°, 32 transversal slices (3 mm), voxel size 3 x 3 x 3 mm, FoV 192 mm). For functional imaging, subjects were asked to keep awake and keep their eyes closedno other controlled task had to be performed. In addition a localizer, DTI and T2 sequence were recorded for each subject. Each scan session started a localizer sequence (TR 20 ms, TE 5 ms, 3 slices (8 mm), voxel size $1.9 \times 1.5 \times 8.0$ mm, FA 40°, FoV 280 mm, 192×192 matrix). For each participant anatomical T1-weighted scans (TR 1900 ms, TE 2.25 ms, 192 sagittal slices (1.0 mm), voxel size $1 \times 1 \times 1$ mm, FA 9°, FoV 256 mm, 256×256 matrix) as well as T2-weighted scans (TR 2640 ms, TE1 11 ms, TE2 89 ms, 48 slices (3.0 mm), voxel size $0.9 \times 0.9 \times 3$ mm, FA 150, FoV 220 mm, 256×256 matrix) were acquired. The Virtual Brain pipeline was used for the preprocessing of the data. Further details regarding the preprocessing steps and image acquisition parameters can be found in [90].

2.1.3 FMRI connectivity

Figure 2.2 outlines the major steps to generate clean BOLD region wise time series. In order to generate the functional connectivity (FC) matrices, raw fMRI DICOM files are first converted into a single 4D Nifti image file. After this step, FSLs FEAT pipeline is used to perform the following operations: deleting the first five images of the series to exclude possible saturation effects in the images, high-pass temporal filtering (100 seconds high-pass filter), motion correction, brain extraction and a 6 DOF linear registration to the MNI space. Functional data is registered to the subjects T1-weighted images and parcellated according to FREESURFERs cortical segmentation. By inverting the mapping rule found by registration, anatomical segmentations are mapped onto the functional space. Finally, average BOLD signal time series for each region are generated by computing the mean over all voxel time-series of each region. From the region wise aggregated BOLD data, FC matrices are computed within MATLAB using pairwise mutual information (on z-transformed data), and Pearsons linear correlation coefficient as FC metrics. Any pre-processing technique, which implies a normalization of data must be avoided when using our analytic operation, for this reason it is important to stress that we did not perform global signal regression on data. Global regression, in fact, changes the distribution of the eigenvalues of the FC and, in particular, shifts the correlations towards negative values. In resting- state BOLD data, this means that zero and negative correlations are introduced. While the debate on the meaning of these negative correlations and on the appropriateness of the use of global regression is open, this procedure must absolutely be avoided when using the analytical operation here presented as the introduction of zero eigenvalues leads to the impossibility of inverting FC to obtain SC. This, not only causes the loss of some information, but it is also based on the assumption that the distribution of the positive eigenvalues is unaffected by global regression, which is not the case as all the eigenvalues become more negative. The major steps involved in generating rs-FC matrix are brain extraction, motion correction, six-degrees of freedom (DOF) linear registration to the MNI space and high pass temporal filtering. Each participants functional images were registered to pre-processed T1-anatomical images and parcellated into 68 regions of interest (ROIs) using FREESURFERs Desikan-Killiany atlas [38]. Regional time-series were obtained

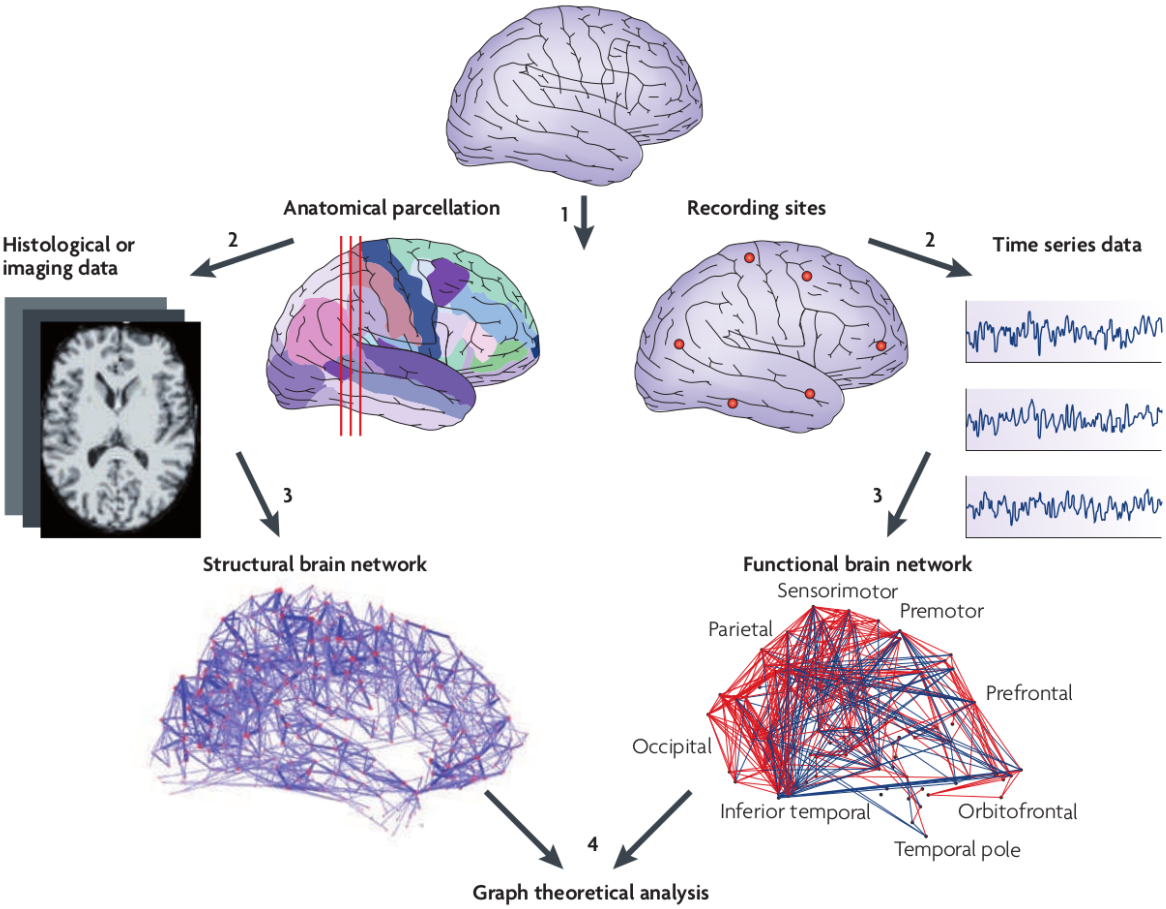

Figure 2.3: **Exploration of structural and functional networks through graph theory**. Following the four steps leads to brain networks: 1. Define network nodes, 2. Define a measure of node-association (edge), 3. Generate the association matrices, and 4. Calculate the network properties. Adapted from [21].

by considering weighted average from voxel-wise time-series. Subject-specific resting state functional connectivity (rs-FC) matrices were obtained by applying z-transformed pairwise Pearson correlation between each pairs of regional BOLD time-series.

2.2 Network Theory

After the data is preprocessed, SC and FC matrices are considered as the structural and functional networks and their properties have been extensively studied. Figure 2.3 highlights the scheme for constructing structural and functional networks of the human brain.

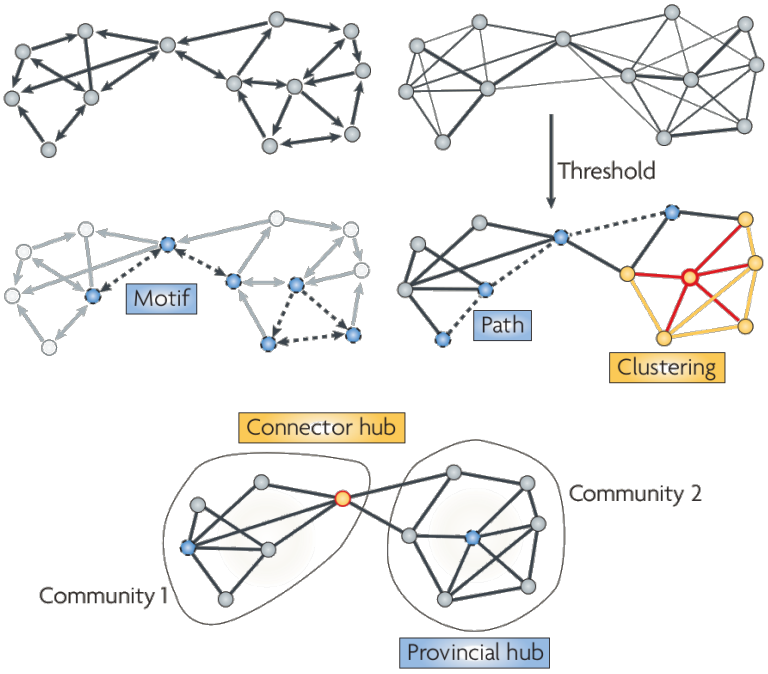

Figure 2.4: **Network properties**. Visualization of the network properties defined for analyzing human brain. Modified from [21].

2.2.1 Network properties of a graph

Figure 2.4 depicts some of the key network properties. One of the elementary properties of the graph is the *degree distribution* of the nodes. This is important to observe as it tells the importance of each node to connect to its neighbors, i.e. the number of nodes that maintain the topology of the graph. Two nodes may be directly connected with an edge or indirectly through a path via intermediate nodes. Such paths determine the flexibility of information exchange between two nodes. Longer the paths, lesser the effect of communication. Adjacency matrix, $\mathbf{W}$, provides a succinct representation of all the possible paths.

Functional interactions diminish away between nodes that are topologically far apart, i.e. large path lengths. Hence this defines a natural way to segregate nodes into clusters containing local neighborhoods [109]. Different neighborhoods may have different patterns of connectivity, thus forming the elemental units of sub-graphs called *motifs*. Besides segregating nodes into communities, there are measures of integration of information between these communities measuring the capacity of network to pass and distribute information. One of them is the characteristic path length - global average of the graph's distance matrix. A short path length indicates that nodes are reachable with small paths. Another measure is the *global efficiency* [69] computed as the average of the inverse of the distance matrix. Low efficiency means that nodes are disconnected, and large efficiency means nodes can be easily reached. Segregation and integration act as two opposing forces for constructing the network.

The above global measures tell about the overall arrangement of the graph, but do not describe the importance of each node in the communication mechanisms. The impact of each node may be different, and the nodes that are most influential are called *hubs* of the network. Degree of the nodes can be a measure to identify the strongly connected nodes. In case of modular architectures, the intra-module and inter-modules connectivity determines the hub nodes. Nodes that facilitate inter-modules communication are termed as hubs, and this is measured via participation coefficient [49]. A related notion to hubs is the *centrality* of a node in terms of it control over the information flow [44]. There are many ways of measuring centrality. One of them is the betweenness centrality that describes how many edges intersect at a given node. The higher this number, the central the node is. Consequently this measure can be associated with an edge as well. The measures of centrality are based on underlying assumptions of the dynamics over the network [18]. Another relatively recent centrality measure takes into consideration of the indirect influences and makes nodes close to central nodes central themselves. This is called eigenvector centrality. Categorizing nodes and edges based on centrality is important as nodes that are structurally central may participate in a large number of functional processes.

2.2.2 Network architectures

Networks in the real world fall into distinct classes of architectural constructs, and these constructs play a major role in shaping the dynamics over the graphs.

- **Random vs. Regular** Random graphs are attributed to ErdsRnyi. First a set of disconnected nodes is taken. With a uniform probability distribution, two nodes are randomly connected. Random graphs do not have any order in the connections. Because of uniform probability, degree distribution has a characteristic scale. Two connected nodes may not be sharing the same neighbors. In contrast, in a regular graph, nodes are connected in an orderly fashion. An example is the regular lattice. Two connected nodes are highly likely to share the same neighbors. These graphs are locally dense. Many real world graphs do not show such ideal behaviors. Degree distribution of such graphs is spread out in a wide range, but two nodes can be reached with a average path length of 6 hops. Such networks are called *small-world-networks* with a measure defined by Humphries et al. [59]. Small-worldness is a global property satisfied by many real-world networks, thus architectural design in particular cannot be determined.

- **Scale-freeness** Another property of real-world networks is the broad width of non-homogeneous degree distribution. This distribution is called a power law. It can be understood as follows - if x is a possible degree with a probability $p(x)$, then the ratio $\frac{p(2x)}{p(x)}$ is a constant. This implies that the nature of the distribution does not change when zoomed in at any degree location, thus suggesting non-presence of any *scale* of connectivity in the network [8, 7].

Small-worldness and scale-freeness are the two major properties of real-world networks, and thus also manifested by brain networks. Almost all fields are respecting the abstract representation of a physical

system as a network, but the subtleties in the meanings of nodes and edges need to be clearly understood requiring us to understand these physical systems in some depth. The same goes for networks of the brain. As a fact, there are many representations of brain as a network coming from multiple modalities used to capture it!

2.3 Spectral Graph Theory

A graph is defined as a set of elements and their pairwise connections. These elements are mathematically abstracted as *nodes* (or vertices) and their connections as *edges*. The set of nodes is denoted as $V = (v_1, \cdots, v_n)$ and set of edges as $E = \{(v_i, v_j)|(v_j \sim v_i) = w_{i,j} \geq 0\}$. An edge exists only if two nodes have a relationship, $w_{i,j}$ is the weight of the relationship between nodes v_i, and v_j. These nodes on themselves can be lying in a Euclidean space, but because of their pairwise relationships, the graph defines an underlying non-Euclidean space for the nodes. An edge can represent many sorts of relationships; similarity, dis-similarity, or a constraint (that two nodes should not be related!). Here we consider the relationships that capture similarity as such graphs have been analyzed in depth. A graph can be represented by a matrix, called weighted adjacency matrix, $\mathbf{W}_{n\times n}$ whose $(i,j)^{th}$ entry $w_{i,j}$ is the similarity between vertices v_i and v_j, n being the number of nodes. Such an underlying non-euclidean topology is analyzed in terms of eigenvalue-eigenvector spectrum of graph in the field of *spectral graph theory* [24]. Spectral analysis of a graph starts first by constructing its Laplacian matrix $\mathbf{L}_{n\times n}$. $\mathbf{L}$ is the gram matrix of the incidence matrix of the graph. If $\mathbf{D}_{n\times n}$ is the degree matrix of the graph with its diagonal entries $d_{i,i}$ representing the degree of node i, then $\mathbf{L}$ is defined as $\mathbf{L} = \mathbf{D} - \mathbf{W}$.

In order to understand the graph Laplacian, consider a regular grid, i.e. nodes, $v_{m,n}$ at the spatial location (m, n), are points on a regular two-dimensional plane connected to their four neighbors with a weight say $\frac{1}{(\delta x)^2}$. Then the graph Laplacian is the five-point stencil approximation of the continuous Laplacian operating over a function, $f = f(m, n)$ at (m, n), defined over the nodes of this regular mesh (*abusing the notations*) [53].

$$\mathbf{L}f(m,n) = \frac{4f(m,n) - f(m+1,n) - f(m-1,n) - f(m,n+1) - f(m,n-1)}{(\delta x)^2}. \tag{2.1}$$

The continuous Laplacian on a function is approximated in this standard way. Laplacian matrix represents the second-order derivative operator on the functions on a graph. In this respect it captures the topology of the graph and becomes a basis for defining all the operators over the graph.

Laplacian matrix provides a link between discrete graph representations and vectors in continuous Euclidean space. Mathematical operators defined in the continuous space are extended in the discrete space via the graph Laplacian matrix. Continuous-space kernels operate on vector valued functions defined by physical processes in that space. The discrete counterparts of these operators are the kernels defined as functions of the graph Laplacian. These kernels operate on functions or signals defined on the nodes of the graph.

An important random process over a graph is diffusion. The kernel that captures the spatio-temporal extent of diffusion is the diffusion kernel $\mathbf{H}$. These graph kernels operate on the real valued functions $f : V \to \mathbf{R}$ on the set V of the graph. Diffusion of a function on a graph captures the spatial extent of spread of the function with time - at node v_i the time evolution of the function will be as follows:

$$\begin{aligned}\frac{d}{dt}f_{v_i} &= -\gamma \sum_{j=1}^{n} w_{i,j}(f_{v_i} - f_{v_j}) \\ &= -\gamma\Big(f_{v_i}\sum_{j=1}^{n} w_{i,j} - \sum_{j=1}^{n} w_{i,j} f_{v_j}\Big) \\ &= -\gamma \sum_{j=1}^{n} \Big(\delta[i]d_{i,i} - w_{i,j}\Big) f_{v_j},\end{aligned} \tag{2.2}$$

where γ is a scalar constant and $\delta[i]$ is the impulse function:

$$\delta[i] = \begin{cases} 1 & \text{when at node } i \\ 0 & \text{otherwise.} \end{cases}$$

Writing Equation 2.2 for all the nodes,

$$\frac{d}{dt}f = -\gamma \mathbf{L} f, \tag{2.3}$$

graph Laplacian plays a crucial role in the differential equation. Being a linear first order differential equation, its closed form solution is:

$$f(t) = e^{-\mathbf{L}\gamma_i t} f(0). \tag{2.4}$$

The exponential function of the graph Laplacian is the kernel over the graph that represents the extent of diffusion of the function f at the *diffusion scale* γt. Diffusion (or heat) kernel is uniquely defined at its scale given the graph.

One of the important properties of Laplacian matrix is that it is a positive semi-definite matrix, hence it is eigen-decomposable:

$$\begin{aligned}\mathbf{L} &= \mathbf{\Psi}_{n\times n}\mathbf{\Lambda}_{n\times n}\mathbf{\Psi}^{\top}_{n\times n}, \\ \mathbf{H}_i &= \mathbf{\Psi} e^{-\mathbf{\Lambda}\gamma_i}\mathbf{\Psi}^{\top} = e^{-\mathbf{L}\gamma_i}.\end{aligned} \tag{2.5}$$

$\mathbf{L}$ has a complete set of orthonormal eigenvectors $\mathbf{\Psi} = [\psi_1, \cdots, \psi_n]$, a column being one, and their corresponding non-negative eigenvalues $\mathbf{\Lambda} = diag(\lambda_1, \cdots, \lambda_n)$ arranged in non-decreasing order from top to bottom rows. Specific to the solution of Equation 2.3, function at time t is a linear combination of the eigen-functions with their amplitudes modulated by the exponential kernel:

$$f(t) = \sum_{i=1}^{n} (e^{-\gamma\lambda_i}\psi_i)(\psi_i^{\top} f(0)). \tag{2.6}$$

All these kernels can be principly put in another framework also. This framework extends the conpcets of signals and systems onto irregular domains such as graphs.

2.4 Graph Signal Processing

In the signal processing domain, a function is treated as a signal, now if on every node of the graph there is a signal, this combined signal over the entire graph is called a graph-signal $\mathbf{u} \in \mathbf{R}^n$. This graph-signal forms a pattern over the graph-topology. The emerging field of *graph-signal-processing* analyzes such graph-signals in terms of their components on defined *harmonics* based on the algebraic and spectral properties of graph-topologies [94].

We will first conceptualize the notion of frequency over a graph and the corresponding Fourier basis defining the transform. For a 1-dimensional signal $u(t)$ varying with time t, the Fourier transform is as follows:

$$\mathcal{U}(\omega) =< u(t), e^{j\omega t} >= \int_{\mathbf{R}} u(t) e^{-j\omega t} dt, \tag{2.7}$$

where ω is the angular frequency of the complex exponential basis signal and $j = \sqrt{-1}$. Every component of the signal on a Fourier basis signal is the inner product between the two. Consider the eigenfunctions of the 1-dimensional Laplacian operator:

$$\Delta(e^{j\omega t}) = \frac{\partial}{\partial t}\Big(\frac{\partial}{\partial t}(e^{j\omega t})\Big) = j\omega \frac{\partial}{\partial t}(e^{j\omega t}) = -\omega^2 e^{j\omega t}. \tag{2.8}$$

These eigenfunctions are the Fourier basis signals with their corresponding eigenvalues as the square of the frequency. Thus the graph Fourier transform is defined as the expansion of a graph-signal in terms of the eigenvectors of graph-Laplacian:

$$\begin{aligned} \hat{\mathbf{u}}_i &=< \mathbf{u}, \psi_i >= \sum_{k=1}^{n} \mathbf{u}_k \psi_i^*(k) \\ \hat{\mathbf{u}}_{n\times 1} &= \mathbf{\Psi}^{\top}_{n\times n} \mathbf{u}_{n\times 1} \end{aligned} \tag{2.9}$$

$\mathbf{\Psi}^{\top}$ representing the conjugate of the eigenvectors and $\mathbf{\Lambda}$ representing the square of the frequencies of the graph-topology.

In the classical Fourier analysis the angular frequencies ω carry a specific meaning of frequency. The smaller the ω the slower the oscillation of the Fourier basis signal and vice versa. And for $\omega = 0$ the basis signal takes a constant value. Similarly in the case of graphs, the graph Laplacian eigenvectors corresponding to lower (higher) λ_i's vary slowly (rapidly) on the graph, introducing the concept of graph harmonics. If there is a strong edge between two nodes, the dissimilarity between the values of the eigenvector on the two locations will increase with λ.

The inverse graph Fourier transform is also easily deducible:

$$\begin{aligned} u(t) &=< \mathcal{U}(\omega), e^{-j\omega t} > \\ \mathbf{u}(t) &= \mathbf{\Psi}\hat{\mathbf{u}}. \end{aligned} \tag{2.10}$$

In the above equation, the graph-signal $\mathbf{u}$ is represented as a linear combination of graph harmonics (columns of $\mathbf{\Psi}$) where elements of $\hat{\mathbf{u}}$ form the coefficients of linear combination which represent contribution of each component graph harmonic.

Filtering of signals form an important aspect in signal processing with their applications ranging from noise-removal, compression, communication etc. Filtering operations in spatial domain require convolution operations. Euclidean spaces such as time-signals and images have a notion of a regular neighborhood of every point in the space, which aids spatial convolution by simply sliding the window to every point and compute the integral of the point-wise multiplication of the signal and the filter. Following equation is example of convolution of a signal g and a filter h, both defined in time-domain.

$$(f \star g)(t) = \int_{-\infty}^{\infty} f(t) * g(\tau - t) d\tau \tag{2.11}$$

The symbol $\star$ defines the convolution operation. However in case of a graph, neighborhood at each vertex $v \in V$ is not constant. Coming up with a spatial filter for a graph is hence not trivial. It is important to see that the convolution operation in the original domain, or the vertex domain, is easily becoming a multiplication in the graph Fourier domain. Frequency filtering of graph signals preserves this notion of convolution by modulating the contribution coefficients of the component graph harmonics, which can be mathematically expressed as follows:

$$\hat{\mathbf{y}} = \hat{\mathbf{h}} \odot \hat{\mathbf{u}}. \tag{2.12}$$

Here $\hat{\mathbf{u}}$, $\hat{\mathbf{h}}$ and $\hat{\mathbf{y}}$ are the graph signal, filter and the filtered output defined in spectral domain respectively. The low (high) valued elements in the function $\hat{\mathbf{h}}$ attenuate (amplify) the contribution of the component graph harmonics thereby filtering the graph signal. The operator $\odot$ defines Hadamard product / element-wise product of two vectors. The above operation can be generalized by considering spectral domain signals as functions over the eigenvalues of the graph, which carry the notion of frequency of the component graph harmonics.

$$\hat{y}(\lambda) = \hat{h}(\lambda)\hat{u}(\lambda). \tag{2.13}$$

We can take an inverse graph Fourier transform of $\hat{y}$ to get the final filtering output in vertex domain:

$$\begin{aligned} \mathbf{y} &= \mathbf{\Psi}\hat{y} \\ &= \mathbf{\Psi}\left(\hat{h}(\mathbf{\Lambda})\hat{\mathbf{u}}\right) \\ &= \mathbf{\Psi}\hat{h}(\mathbf{\Lambda})\mathbf{\Psi}^{\top}\mathbf{u} \\ &= \hat{h}(\boldsymbol{L})\mathbf{u} \end{aligned} \tag{2.14}$$

The graph filtering approach can be used to conduct various techniques such as smoothing, translation, diffusion etc. As a special case, if $\hat{h}$ is considered to be an exponential function, we get a diffusion kernel or heat kernel over the graph Laplacian as defined in Equation 2.5.

2.5 Computational Models of the Large-Scale Brain Dynamics

Processes happen at the cellular level, impulses are generated and transmitted to other nerve cells. This phenomenon is expressed via connectivity, i.e. the way neurons demonstrate mutual functional

dependence allowing each neuron to function independently *and* collectively. All the cognitive functions such as memory, attention, etc require this large-scale integrative coordination manifest as complex patterns. At the same time, cognitive processes are better captured in large-scale indirect measurements such as functional MRI (fMRI), DTI, Electroencephalography (EEG) and Magnetoencephalography (MEG), etc. This demands urgent necessity for *computational models* to decipher these patterns and map them to neural and/or regional functions.

To understand the rich spatio-temporal nature of brain's complex system, computer simulations become inevitable. The data is rich enough that neither only theoretical analysis nor only empirical experimentation would match the complexity of data. Computer simulations rather provide the middle ground between mathematical underpinnings and experimentations. In order to explain the neuroscience data and to make predictions from them requires computational modeling. In a computational model, each unit and their interactions must be well parameterized. The parameters must clearly describe the qualitative concepts; either implicitly or explicitly [76]. Typically a computational model is described as a set of coupled partial differential equations. Each individual partial differential equation takes different forms and describes the rate of change of a system variable. Coupling between these equations is given by the anatomical connectivity. This setup represents the *state* in which the system is currently in, hence also called state equations. Solution of this coupled system is via integrating the equations, which is usually numerical in nature. This process, carried out through a computer, results into time-series that can be analyzed after embedding in a geometric *phase space* or loosely the space of the model parameters.

The system variables combined together become a vector lying in a trajectory in this space. Each point in this space becomes a state of the system. In this space, the system moves towards some points called *attractors*. An attractor may be a single point or a grand geometric shape. An attractor is stable if the system maintains a certain balance under perturbations and returns to the attractor. With changes in the parameters of the model and initial states the model traverses different trajectories towards different attractors. These trajectories are called attractor *basins*. This dynamics in the phase space is mapped to the empirically observed time-series data such as BOLD activity facilitating tuning of the model parameters. This allows relating the various dynamic regimes attained by the system with the variations in the parameters, making them possess a bio-physical meaning.

Most of the modeling techniques are composed of non-linear differential equations that require computer simulations. Some of the models are linear in nature, such as in Galan [46]. Such models can be analyzed with relative ease. Such linear models provide a fair estimate of large-scale functional patterns over structural patterns, but do not resemble any direct relationship with the underlying bio-physics. For an overview of all the classes of models, please refer to Nakagawa et al. [76]. Broadly, there are dynamic mean field models that consider a neuronal activity obeying a coupled differential equation that is generated as a stable oscillating noise. Another broad class is the reaction-diffusion systems that uses the spectral analysis of structural connectome. Both the models generate rs-fMRI time series over the SC.

2.6 Discussion

This chapter introduces the reader to the dataset used in this thesis and the methods applied to develop the models. We have a set of SC-FC pairs of 47 healthy subjects. The models developed will be based on the concepts of spectral graph theory and graph signal processing. The subsequent chpater introduces the reader to the notion of diffusion over a brain graph thus motivating the proposed models.

Chapter *3*

Diffusion over a Brain-graph

In this chapter we describe the basic diffusion models, their advantages and limitations and directions for extensions.

3.1 Diffusion over a graph

This model is developed by Abdelnour et al. [2] where authors propose a diffusion scheme to explain the relationship between SC and FC. This model is connected to a linear first-order system over the SC.

3.1.1 Model

Consider an isolated region, r_i, in the brain. Let the aggregate neuronal activity of all the neurons within the region be denoted by $x_i(t)$ at time t. If a simple linear damped system is assumed to govern the evolution of this activity, the activity at time t is the solution of the following:

$$\frac{d}{dt}x_i(t) = -\gamma x_i(t). \tag{3.1}$$

Largely possible due to the refractory period of the neuronal activities, the large-scale regional activity damps down with a decay rate of γ. Now consider an isolated pair of regions r_i and r_j with the anatomical connectivity strength of $w_{i,j}$ between them. Activity of r_i is affected by that of r_j and vice versa through the anatomical connectivity. The regions obey the following equation:

$$\frac{d}{dt}x_i(t) = \gamma \left(w_{i,j}x_j(t) - x_i(t)\right). \tag{3.2}$$

For the sake of simplicity it is assumed that the decay rate is constant for all the regions. Now consider all the n regions in the large-scale brain graph and their interactions as follows:

$$\frac{d}{dt}x_i(t) = \gamma \left(\sum_{j=1}^{n} w_{i,j}x_j(t) - x_i(t)\right). \tag{3.3}$$

When such linear differential equations for all the regions are combined the final equation takes the following form:

$$\frac{d}{dt}\mathbf{x}(t) = -\gamma \mathbf{L}\mathbf{x}(t), \tag{3.4}$$

where $\mathbf{L}$ is the graph Laplacian. The solution of this equation is the graph diffusion kernel, $\mathbf{H}$:

$$\mathbf{x}(t) = \exp\left(-\gamma \mathbf{L} t\right) \mathbf{x}(0), \tag{3.5}$$

with the diffusion scale being γt. The evolution of the graph signal $\mathbf{x}$ from $t = 0$ to $t = t$ is governed by the diffusion kernel.

Now consider that only node, node i, is the heat source and others are sink nodes, i.e. one of the elements of $\mathbf{x}(0)$ is non-zero. At time $t = t$ the graph signal of mean regional activities is the i^{th} column of diffusion kernel. This column of diffusion kernel tells about the amount of heat reached to other regions, or the statistical dependence between the two regions, when r_i is the source. This points to the hypothesis that i^{th} column of diffusion kernel resembles the i^{th} column of FC:

$$\mathbf{x}(0) = \mathbf{e}_i, \tag{3.6}$$

where $\mathbf{e}_i$ is the cardinality vector in i^{th} direction or node. Intuitively, the diffusion kernel represents the influence of a source node onto its neighbors and the diffusion scale encodes the extent over the node space. As the diffusion kernel is symmetric, r_i also receives the same amount of heat it provides to others when those regions are heat sources. Considering that each node is independently a heat source, the collective matrix resembles the FC:

$$FC = \exp\left(-\gamma \mathbf{L} t\right) \left[\mathbf{e}_1, \cdots, \mathbf{e}_n\right] = \exp\left(-\gamma \mathbf{L} t\right) \mathbf{I}_{n\times n} = \exp\left(-\gamma \mathbf{L} t\right), \tag{3.7}$$

thus providing the diffusion kernel a meaning that resembles the functional connectivity. There are two aspects to the model:

- representation of functional integration in terms of graph kernels, especially modeling temporal dynamics as a diffusion process over the graph, and
- the provision of identity matrix governing independent heat sources that initiates the diffusion process.

As the diffusion kernel is uniquely defined by its scales of diffusion, Abdelnour et al. iterate over the space of scales, and plot the Pearson correlation between the empirical FC and the predicted FCs, or the diffusion kernels. We will be calling this model as Single Diffusion Kernel (SDK) model from now on.

3.1.2 Major claims and limitations of the model

Their results suggested the possibility of a single-scale of diffusion that enables maximum correlation between observed FC and estimated FC in experiments with eight subjects. Consequently we investigated

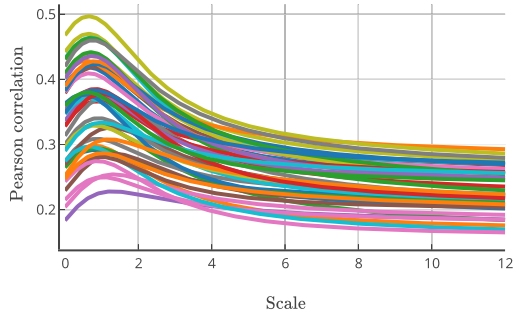

(a) Pearson correlation curves with thresholding

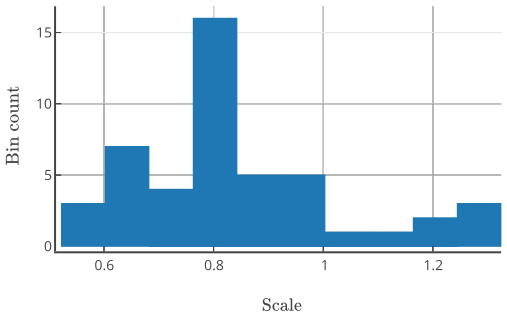

(b) Distribution of scales with thresholding

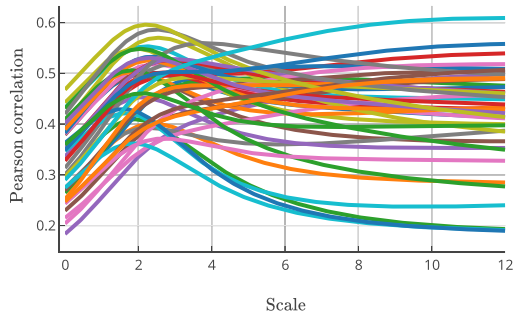

(c) Pearson correlation curves without thresholding

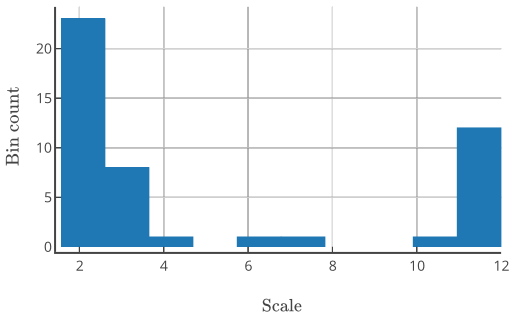

(d) Distribution of scales without thresholding

Figure 3.1: **Variation in the Optimum Scale across all Subjects in the Single Scale Diffusion Kernel (SDK) Model.** We simulated the SDK model for the Berlin dataset and found that there is a variation in the subject-wise optimum scale. When the SC matrices are pruned by removing edges less than 0.07% of the maximum edge value (in the adaptation of Abdelnour et al.'s implementation code [2]), there seems to be a unique scale for the cohort. (a) shows the Pearson correlation curves for all the subjects. The histogram of the optimum subject-specific scales also has some variations as shown in (b). But, when the SCs are not thresholded, the correlation is higher but there seems to be significant variation in the optimum scale required for the SDK model; as shown in (c) and (d). This experiment motivated us to investigate diffusion at multiple scales, resulting in the current proposal of a multi-scale diffusion model. We thank the authors for kindly providing their code which was used for reproducing the results with SDK model.

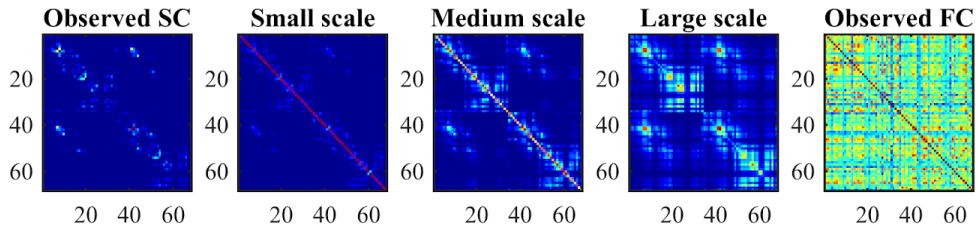

Figure 3.2: **Multiple diffusion kernels**. Shown here is the similarity between diffusion kernels and the empirical FC. The kernels are derived from the empirical SC at three diffusion-scales. It can be seen that each kernel shares some similarity with FC and these similarities are complementary among the kernels. Small (large) diffusion-scales contribute to local (global) diffusion. Both of these aspects seem to be present in the FC.

the viability of this hypothesis over a larger subject pool [97]. In our simulation experiments we found that the diffusion scale for maximal correlation (between the empirical and observed FCs) varies widely across subjects as shown in Fig. 3.1.

On the other hand, we also observed that for an individual subject, diffusion at different scales reveals multiscale relationships among various ROIs. Thus, multiple scale dependent diffusion kernels over SC can be interpreted as components of FC at different scales (see Figure 3.2).

According to the model, functional connections are explainable via a single diffusion kernel which is scale dependent. This forces all the regions to participate in the diffusion phenomenon with the same extent of their influences. Additionally, the identity matrix may mean that prior to diffusion all regions are independent sources not modulated by any factor(s), but we hypothesize that even in resting state, non-physically connected regions may modulate initial source configurations at multiple diffusion scales. Moreover, the model *hand-picks* the optimal diffusion scale for each subject. This makes their claim of existence of single-diffusion-scale weaker as it might be only an empirical artifact.

3.2 Combining multiple diffusion kernels

3.2.1 Model

We extend the linear graph-theoretic dynamic model proposed in [2] for learning the structure-function relationship using a novel MKL formulation. The model represents FC as a linear combination of multiple diffusion kernels as shown in Eq. 3.8:

$$\mathbf{C}_f = \sum_{i=1}^{m} \mathbf{H}_i \alpha_i. \tag{3.8}$$

As diffusion kernels transform SC into nonlinear spaces, we hypothesize that the linear combination of these nonlinear mappings would give rise to a good estimation of FC. Let $\boldsymbol{\tau} = \{\gamma_1, \cdots, \gamma_m\}$ be the set of m diffusion scales. For each γ_i a corresponding $\mathbf{H}_i$ is obtained. Let $\boldsymbol{\alpha} = \{\alpha_1, \cdots, \alpha_m\}$ be the

set of coefficients of linear combination (also called here as mixing coefficients) for the corresponding m kernel matrices. These mixing coefficients are subsequently learned while solving an optimization formulation that minimizes the squared error between empirical FC and predicted FC.

Let the number of subjects for whom SC-FC pair is considered during the training phase be p. We can write the optimization function as:

$$\begin{aligned}\hat{\boldsymbol{\alpha}} &= \underset{\boldsymbol{\alpha}}{argmin} \sum_{j=1}^{p} \|\text{FC}^j - \mathbf{C}_f^j\|_{L_2}^2 \\ &= \underset{\boldsymbol{\alpha}}{argmin} \sum_{j=1}^{p} \|\text{vec}(\text{FC}^j) - \sum_{i=1}^{m} \text{vec}(\mathbf{H}_i^j)\alpha_i\|_{L_2}^2,\end{aligned} \tag{3.9}$$

where, vec$(\cdot)$ converts an $n \times n$ matrix into an ${}^{n(n-1)}/_2 \times 1$ vector.

Let $\mathbf{X}^j = \left(\text{vec}\left(\mathbf{H}_1^j\right), \ldots, \left(\mathbf{H}_m^j\right)\right)_{n^2 \times m}$, $\mathbf{Y}^j = \text{vec}\left(\text{FC}^j\right)_{n^2 \times 1}$, $\boldsymbol{\Psi} = \left(\mathbf{X}^{1\top} \quad \cdots \quad \mathbf{X}^{p\top}\right)^{\top}_{n^2 p \times m}$, and $\boldsymbol{\Phi} = \left(\mathbf{Y}^{1\top} \quad \cdots \quad \mathbf{Y}^{p\top}\right)^{\top}_{n^2 p \times 1}$. Then,

$$\begin{aligned}\hat{\boldsymbol{\alpha}} &= \underset{\boldsymbol{\alpha}}{argmin} \left(\boldsymbol{\Psi}\boldsymbol{\alpha} - \boldsymbol{\Phi}\right)^{\top} \left(\boldsymbol{\Psi}\boldsymbol{\alpha} - \boldsymbol{\Phi}\right). \\ &= \left(\boldsymbol{\Psi}^{\top}\boldsymbol{\Psi}\right)^{-1} \left(\boldsymbol{\Psi}^{\top}\boldsymbol{\Phi}\right).\end{aligned} \tag{3.10}$$

We find the least squares solution and divide $\hat{\boldsymbol{\alpha}}$ by its sum to normalize the values.

3.2.2 Experiments and results

For all the experiments, we used the dataset described in an earlier chapter. Total of 46 subjects were used out of which 23 subjects were taken for training the model and the model was tested on the remaining 23 subjects.

3.2.3 Parameter Selection and Analysis of the MKL Model

We partitioned the subject pool into two sets - training and testing sets. LASSO method can optimize for one vector instead of a matrix, hence we trained individual columns of $\boldsymbol{\Pi}$ separately. Ascending order of scales focus on further local connections. i.e. scale index 1 corresponds to global diffusion phenomenon and scale index 16 corresponds to local diffusion phenomenon. Rest of the scale indices correspond to intermediate diffusion phenomena in sequence.

3.2.3.1 Choice of scales

A scale of a diffusion kernel represents the extent of spread of the graph signal from the source node where it is deployed. Depending on the graph topology, a fixed scale for all graphs will result in different extents of spread of the signal on individual graphs. Diffusion kernels capture the extent of

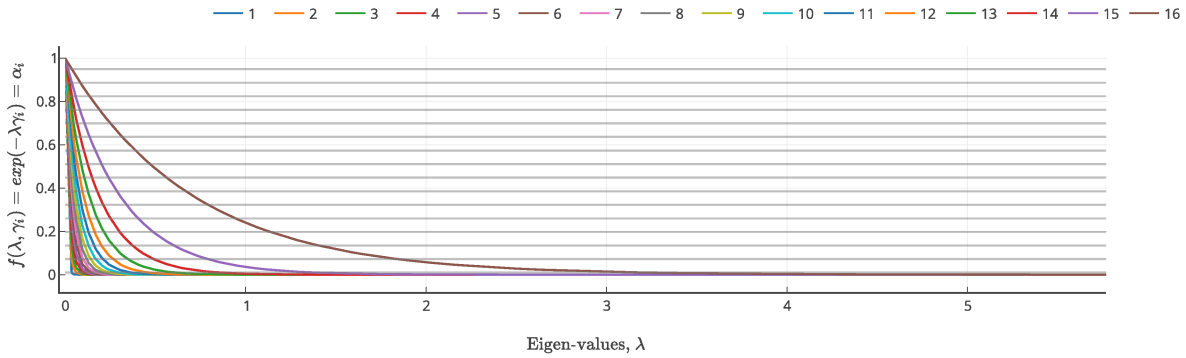

Figure 3.3: **Procedure for selection of scales**. The procedure for choosing scales from the fixed normalized exponential values and a chosen eigenvalue λ of $\mathbf{L}$. Laplacian matrix $\mathbf{L}$ of each SC is eigen decomposed whose 2^{nd} eigenvalue is used to determine subject-specific scale set from the normalized values, kept the same for all subjects. Each exponential curve is a function of the scale (γ) and represents the contribution of every eigen-component of the Laplacian matrix. Grey horizontal lines denote the fixed normalized scale values. If a larger eigen-value is chosen, then all the large scales will be ignored. Hence, the closer the eigen-value towards 0, the better is the scale variation. Hence, justifying the choice of second eigen-value. Intersection points of all the grey lines on the vertical line at second eigen-value allow only one exponential curve to intersect. The scales determining the exponential curves are the subject-specific scales.

spread with their scale parameter γ. Hence to normalize the spread across subjects in the cohort, we fixed the multiple spreads and selected graph (or subject) specific scales. Normalization of diffusion scales is very important as the diffusion scale value is relative to the graph structure/topology, a fixed value may not be suitable for all graphs. Therefore, we fix a set of exponential values α_i's which remain the same for all participants. Figure 3.3 shows the procedure for selecting the subject-specific scales, here for a subject. One fixed exponential value $f(\lambda, \gamma_i) = \alpha_i$ provides one diffusion scale. A diffusion scale is then calculated as:

$$\begin{aligned} \alpha_i &= e^{-\lambda\gamma_i} \\ \gamma_i &= {}^{-\ln(\alpha_i)}/_{\lambda}. \end{aligned} \tag{3.11}$$

Exponential curves represent the 16 selected scales for a sample subject.

3.2.3.2 Choosing sufficient number of scales

Here we answer the question of the required number of scales m for the proposed MKL model. This analysis also demonstrates the robustness of the MKL method with respect to the choice of the number of scales, i.e., the choice of the parameter m. Here we analyze with 5 different values of m using the same training and testing sets used to train the model. We ran the MKL model for each m separately and plotted box-plots for the same in figure 3.4. The yellow line passing through the boxes joins the mean performance of the models, dotted line. The figure suggests that model performance decreases as

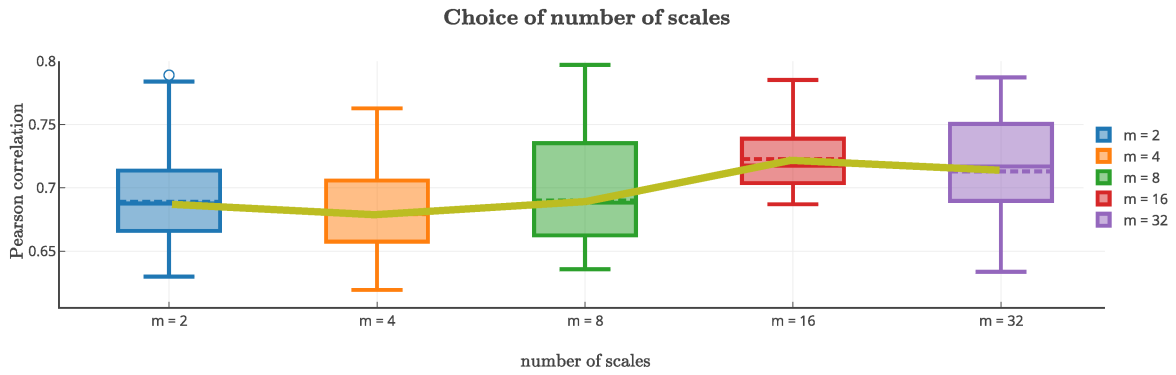

Figure 3.4: **Choice of number of scales, m.** Shown is the MKL model's performance on test subjects. Each bar-plot corresponds to a number_of_scales, m. The thick line inside each box and the dotted line are the median the mean correlation values respectively. As observed, performance increases from $m = 4$ to $m = 16$ and then slightly goes down. For $m = 16$, test performance has the lowest inter-subject variance and highest mean correlation, hence naturally becoming a choice in the design of the model.

m changes from 2 to 4 and then increases till $m = 16$. Further decrease in performance suggests that model might start over-fitting on the training data for scales beyond 16.

3.2.3.3 Configuration of scales

Next we intend to see how important the arrangement of scales is, i.e., how the configuration of scales affects the prediction of FC. To show that the chosen scale set is close to optimal, we randomly generated several scale sets, with uniform distribution between $[0, 1]$ (normalized scale space), and trained our model on each of them separately. The generated scale sets had the property that the scales may not be spread equally in the normalized space. Figure 3.5 plots a histogram of the Pearson correlation coefficients between the test subjects whose mean correlation is plotted in the histogram. The histogram suggests that not only should the scales span the entire space, but they also should be evenly spread in the space. Further it also suggests that the number of scales (16) may be more important than the particular scale values.

3.2.3.4 Model comparison

In the first experiment, we compared the results of SDK model [2] with our proposed MKL model. We use the Pearson correlation (PC) as a measure [58, 2] for comparing observed/ empirical FC and predicted FC. In the single kernel case, we are directly picking the best kernel and computing the PC values for the test subjects. On the other hand, for the MKL model, parameters are estimated from training data and PC values are computed for each of the remaining 23 test subjects. Figure 3.6 shows the comparative results.

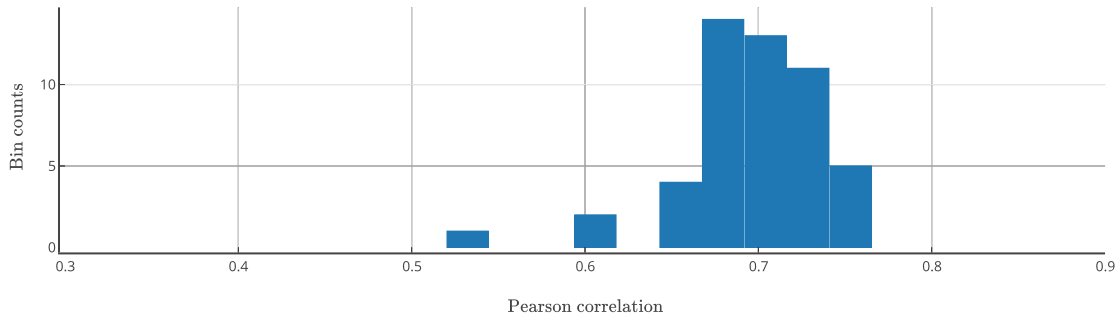

Figure 3.5: **Procedure for selection of scale configuration**. Behavior of the model is studied by varying scale sets, m being fixed at 16. Each scale set was uniformly sampled from the domain $[0, 1]$. Each scale set consists of m instances of normalized scales. The MKL model was trained and tested on the same split separately for each scale configuration. Histogram shows the mean performance of the models. Eigenvalue of Laplacian $\mathbf{L}$ at second index was used to determine equivalent subject-specific scales. Figure suggests that number of scales is more important than particular scale values. We have shown performance by keeping the normalized scales at uniform intervals.

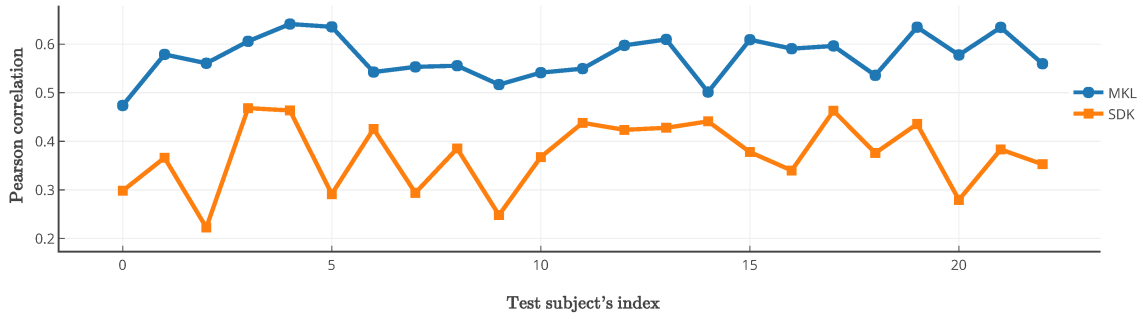

Figure 3.6: **Comparison of the proposed MKL model w.r.t. the single scale model**. As can be seen, the MKL model performs better than the single scale model. It is to be noted that optimal scale for the single scale model was selected on the test subjects' data by searching individually. On the other hand, the optimal parameters for the MKL model were learned through the optimization process on training data.

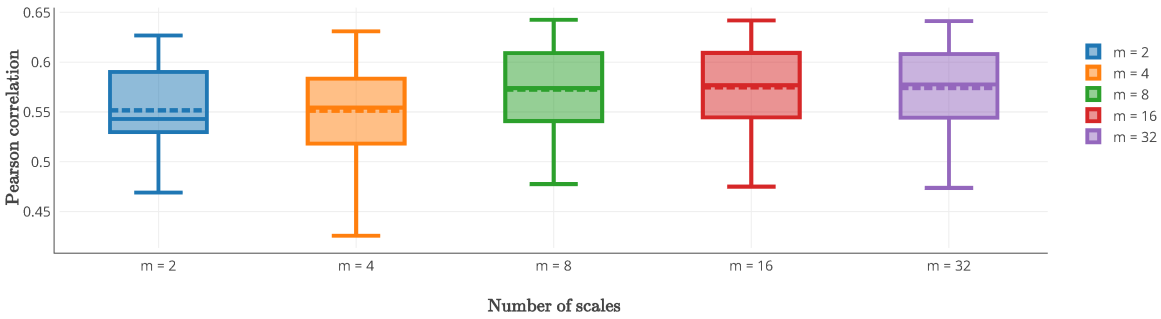

Figure 3.7: **Performance stability of the proposed MKL model for different values of number of scales parameter**. There are 5 box-plots one for each value of number for the number of scales, m. For a value of m, Pearson correlation for all the testing subjects was plotted in the corresponding box-plot. The dotted (continuous) line is the mean (median) across subjects.

Table 3.1: Pearson correlation w.r.t. different number of scales (parameter m).

m	Subjects				
	sub 1	sub 2	sub 3	sub 4	sub 5
02	0.4274	0.5921	0.5309	0.5854	0.6071
04	0.4257	0.5896	0.5438	0.5834	0.6223
08	0.4776	0.5740	0.5565	0.6117	0.6425
16	0.4749	0.5768	0.5604	0.6073	0.6419
32	0.4736	0.5787	0.5605	0.6057	0.6412

3.2.3.5 Robustness of the model

The next experiment demonstrates the robustness of the proposed method w.r.t. the choice of the number of scales i.e., parameter m. Here we experimented with 5 different values of m (using the same train and test set used in the first experiment) and we can see in Figure 3.7 that the model performance is relatively stable. As shown in Table 3.1 the performance of our method shown for five randomly chosen subjects improves with increasing values of m till $m = 8$ and then stabilizes. This was indeed the case with all other subjects. The increase in performance (from $m = 2$ to $m = 8$) is attributed to the fact that with higher multiscale resolution our MKL model perhaps leads to a better reconstruction of the observed FC.

In the final experiments, we try different configurations of scale values (i.e., $\boldsymbol{\tau}$) for $m = 8$. Table 3.2 shows the values for 6 different scale configurations. Figure 3.8 shows the corresponding plot of PC curves. We can clearly see that these PC curves are highly overlapping thereby suggesting that the choice of scale values does not affect the performance of our proposed MKL model.

Figure 3.8: **Performance of the MKL model across different scale sets or scale configurations**. For each of the testing subject, mean and $3\times$standard deviations are plotted in the error-bars. It is observed that as the standard deviations for all the subjects are very small, the model performance is robust with respect to change of configurations.

Table 3.2: Various set of scales $\boldsymbol{\tau}$

Scale	Configurations					
	conf 1	conf 2	conf 3	conf 4	conf 5	conf 6
t_1	25.17	5.27	4.48	4.18	4.04	3.86
t_2	11.64	2.43	2.10	1.94	1.87	1.79
t_3	8.08	1.70	1.44	1.35	1.30	1.24
t_4	5.95	1.25	1.06	0.99	0.95	0.92
t_5	3.22	0.67	0.57	0.54	0.51	0.50
t_6	2.24	0.47	0.40	0.37	0.35	0.34
t_7	1.41	0.30	0.25	0.24	0.23	0.21
t_8	0.05	0.12	0.01	0.01	0.01	0.01

3.3 Discussion

Inferring resting state functional connectivity FC from the underlying structure of the brain (SC) is a challenging open problem in computational neuroimaging. There are broadly two categories of models that attempt this problem - predictive versus generative. Simplistic network communication based models ([48], [106]) as well as diffusion kernel models fall in the former category. A range of generative models have also been proposed to this end using neuro-biologically detailed dynamical models ([32], [72]). Even though each model predicts FC fairly well, the onus of finding the right balance between biological realism and computational tractability remains on the modeler. Recently an elegant tractable dynamical model has been proposed by [2] which assumes linear dynamics between network nodes and predicts FC based on the assumption of macroscopic interactions of brain activity. However, our observation based on the simulation of the same model on another parcellation of SC suggests that the hypothesis of a single best-fitting diffusion kernel applicable across subjects seems to be not viable. This led us to

formulate a more detailed MKL model, which obviates the need for manually searching for the single optimal kernel. More importantly, MKL model involves *learning* of the SC-FC mapping parameters on training set which can be directly used on unseen individual test subjects.

The results demonstrate that the proposed method predicts individual (subject-specific) FC better than the previous model. Further, the model also has the power to explain inter-individual variability in SC-FC relationships. This possibly suggests the existence of latent variables across subjects, which when learnt, can explain the SC-FC relationship. This would in turn avoid the need for generating the long time course signals as is the case with more detailed computational models. Such machine learning approaches with the promise of simplicity might relieve the modelers from cumbersome subject-specific parameter tuning or an educated guess of parameters and initial conditions that are required in other non-linear dynamical models that are designed with a range of free parameters.

As part of future work, it will be interesting to find a better interpretation of the latent variables $\boldsymbol{\alpha}$'s, or some equivalent parameters, and associated kernel matrices. Additionally, we would like to automatically discover the optimal scale configurations instead of assuming them to be chosen a priori. Further, more complex optimization formulations will be explored in order to improve the performance of the SC-FC mapping. In the next chapter we will explore the generic multiple kernel learning framework that incorporates multi-scale analysis along with characterization of the initial states at each scale.

Chapter *4*

Multiple Kernel Learning

This chapter describes the bio-physical framework used to build the model. This framework will be linked to spectral graph theoretic constructs, diffusion kernels. This simplifies the analysis as only the parameters of the well-known diffusion kernels need to be tuned. This work was published in Nature/Scientific Reports [98].

4.1 Bio-physical attempts for relating SC to FC

The question of how SC shapes FC has been the object of computational modeling but remains an open question [19]. In the recent years, connectivity analysis using whole brain computational models and graph theoretic techniques have given unprecedented insights about brain-wide correlations during rest and task conditions [34, 37, 78]. Computational models are designed to expand our understanding and explaining the functioning of the brain. The more biologically real the model is, the more computationally expensive it is. Hence, gaining analytical insights becomes increasingly difficult with complex models.

In the realm of noise-induced correlated deviations, there are linear and non-linear mean field models that attempt to answer this open question incorporating various kinds of dynamics and biological details [46, 9, 57, 2]. As described in detail in an earlier chapter, a biophysical attempt to relate SC to FC is a linear model based on graph diffusion of brain dynamics, the diffusing quantity, firing rate of the neuronal population, undergoing random walk on the SC graph. This linear diffusion model considers that the mean regional activity diffuses over the anatomical fibers governed by a 'deterministic' linear differential equation [2]. The analytically tractable solution becomes the graph diffusion kernel which is hypothesized to resemble the FC. This model fixes one global parameter across all subjects. Another model proposed by Saggio et al. [89] considers a linear auto-regressive model with additive Gaussian white noise, coupling matrix being SC. This model becomes a linear system of coupled 'stochastic' first order differential equations, specifically OrnsteinUhlenbeck process, in which the BOLD activities diffuse on the anatomical constraints, i.e. SC. This model computes covariance between regional activities whose analytical expression works out to be a function of SC. Such a model would find it difficult to account for inter-subject variability in the functional expression. Extending the idea of linearity to super-critical

bifurcations and multi-stability, a series of non-linear stochastic models have been proposed that explain the underlying biological behavior efficiently [33, 31, 52]. These models differ in their representation scheme for the ROIs [75]. Whereas Kuramoto oscillator model [67] abstracts out the biophysical details, Deco and Jirsa's mean-field-models [31, 33] consider dynamics of specific biological analogues such as mean firing rate and mean activity of the regions. These neural and meso-scopic models can be seen as variants of reaction-diffusion system at the heart of which lie the Wilson-Cowan equations [111, 112]. Wilson-Cowan equations, a variant of reaction-diffusion systems, provide a coarse-grained description of the large-scale neuronal network in terms of oscillatory self-organizing patterns. New experimental evidence supports these equations [39].

Recently, a new paradigm of understanding the oscillatory patterns of cortico-cortical activity is proposed that utilizes spectral analysis of the connectome or structural connectivity (SC) [6]. It has been observed that these connectome-specific harmonics predict oscillatory functional networks of the human brain possibly through interplay of excitation; for instance mediated by the glutamatergic principal cells, and inhibition; for instance mediated by the GABAergic interneurons. The push-and-pull between diffusing excitatory cells and suppressing inhibitory cells can result in self-organizing pattern formation. The emergent harmonics or the standing waves are the allowed spatial frequencies, or the eigenfunctions of the graph Laplacian operator on the anatomically constrained SC largely determined by the selection of the diffusion parameters of excitation and inhibition. Surampudi et al. [97] observed that physical diffusion on large-scale graphs, i.e. SC, at multiple *diffusion scales* exhibits scale-dependent relationships among various regions of interest (ROIs) [97]. These multi-scale diffusion kernels are similarly motivated to capture reaction-diffusion systems operating on a fixed underlying connectome (SC) and hence can be interpreted as components of FC at different diffusion scales. However, our investigations revealed that a combination of multiple diffusion kernels was not sufficient to explain the self-organizing resting state patterns found in FC and hence necessitates the need of additional explanatory parameters.

The extant whole brain computational models can be characterized along two dimensions – interpretability and complexity, where the linear and non-linear models lie at the opposite ends of the spectrum. The former are analytical models with few parameters that can be interpreted and tuned easily, whereas the latter are fairly complex models with richer dynamics but tend to be analytically intractable. The proposed model possesses the analytical beauty of linear models and yet is complex enough to capture the biological details. We hypothesize that the presence of regional multi-scale co-activations that initiate diffusion would be necessary to bridge the gap between structurally confined diffusion phenomenon and empirically observed FC and that these co-activations would be common across the cohort. We further provide a plausible mathematical reasoning for the existence of these co-activations along with diffusion kernels by linearizing a variant of reaction-diffusion model and extending it to generate FC. Moreover, we also describe a succinct *multiple kernel learning* (MKL) procedure to retrieve these co-activations by formulating it as an optimization formulation. MKL techniques are well explored in the machine learning community [68, 47]. Our proposed model while retaining the parsimony of a simple linear

approach, proposes a novel learning scheme for optimizing the best-fitting kernels for SC-FC mapping. Our detailed empirical results demonstrate the validity of the proposed model on a larger dataset.

4.2 Existing frameworks

4.2.1 Dynamic Mean Field models

We used the reduced dynamic mean field model as the non-linear model for comparative analysis [36]. This approach considers models with synaptic gating variable with passive decay differential equation along with Gaussian fluctuations. Firing rate was approximated based on input-output sigmoid function of the synaptic gating variable. The whole dynamics of each local network of excitatory and inhibitory populations of spiking neurons interconnected via excitatory synapses can be expressed by a single one-dimensional equation. The global brain dynamics of the network of interconnected local networks can be described by the following set of coupled non-linear stochastic differential equations [36]:

$$\frac{dS_i}{dt} = -\frac{S_i}{\tau_S} + (1 - S_i))\gamma H(x_i) + \sigma\nu_i(t) \tag{4.1}$$

$$H(x_i) = \frac{ax_i - b}{1 - exp(-d(ax_i - b))} \tag{4.2}$$

$$x_i = wJ_N S_i + GJ_N \sum_j C_{ij} S_j + I_0 \tag{4.3}$$

Here S_i is synaptic gating variable of area i. x_i is population mean firing rate for region i. J_N is the excitatory synaptic coupling. ν_i in (4.1) is uncorrelated standard Gaussian noise with noise amplitude $\sigma = 0.001$ nA. I_0 is the external input current. C_{ij} represents entries of the SC matrix which captures the structural connectivity between regions i and j. Parameter values were selected as in Deco et al. [36]. A forward BOLD model was used that converts the local synaptic activity of a given cortical area into an observable BOLD signal. The simulated BOLD signal was down-sampled at 2 secs to have the same temporal resolution as in the empirically measured BOLD signal. Simulation length for computing the model FC was equivalent to 8 minutes. The coupling parameter G (see Equation (4.3)) is varied between 0 to 3. We use individual empirical SC - FC matrices for exploration of subject-wise parameters for optimal fit. The optimal G value varied among the subjects from 0.5 to 3. The mode of the distribution of the parameters obtained for training subjects was taken as the optimal Gs for the training cohort and was found to be 2.85. The same value was used to estimate predicted FCs for all the test subjects.

4.2.2 Reaction-diffusion systems

Fields of neural activity exist because of mutual interaction between the elements of the complex system, based on which self-organizing patterns form. The mathematical framework that explains such a

spatio-temporal change in the field is called Reaction-Diffusion systems. Reaction-Diffusion systems have been employed to model interaction among populations of neurons and the emerging patterns of functional connectivity among neural ensembles [62, 101, 66, 5]. The excitatory and inhibitory neural elements react and the resultant neural activity spreads over the structural pathways. Because of the difference in the parameters of reacting elements, the collective activity evolves spontaneously and forms non-linear patterns. A variant of Reaction-Diffusion system is Wilson-Cowan model that explains the evolution of neural field. Just as statistical thermodynamics relates brownian motion of fluid particles to mean motion of a whole fluid, Wilson-Cowan equations characterize the macro-scopic statistical behavior of mean fields of the resulting neural activities [112, 65].

At time t and at a spatial location $x \in \mathbf{R}^3$ let $E(x,t)$ and $I(x,t)$ be the local spatio-temporal mean neuronal activity. Their time evolution of these activities obeys the following system of coupled differential equation:

$$\begin{aligned} \tau_s \frac{\partial}{\partial t} E(x,t) &= -d_E E(x,t) + S\left(\alpha_{EE}\mathcal{D}_{EE}[E(x,t)] - \alpha_{IE}\mathcal{D}_{IE}[I(x,t)]\right) \\ \tau_s \frac{\partial}{\partial t} I(x,t) &= -d_I I(x,t) + S\left(\alpha_{EI}\mathcal{D}_{EI}[E(x,t)] - \alpha_{II}\mathcal{D}_{II}[I(x,t)]\right), \end{aligned} \tag{4.4}$$

where $\mathcal{D}_{EE}, \mathcal{D}_{IE}, \mathcal{D}_{EI}, \mathcal{D}_{II}$ are the spatial diffusion operators separately acting on the excitatory and inhibitory populations with their corresponding diffusion strengths $\alpha_{EE}, \alpha_{IE}, \alpha_{EI}, \alpha_{II}$ respectively. S denotes the sigmoidal activation function. d_E, d_I are the excitatory and inhibitory decay rates. τ_s denotes the characteristic time constant that determines the speed of evolution or the frequency range of oscillations [6]. In the continuous domain the diffusion phenomenon is understood as integration against Gaussian kernels, in case of of discrete domains the diffusion operator takes the form of graph-diffusion-kernel [6].

4.3 Proposed MKL model

We propose the multiple kernel learning model as a variant of Reaction-diffusion (RD) systems [74] wherein the regional mean activities diffuse on the graph determined by anatomical pathways (SC). Recent models incorporate the random-walk stochastic process on network of connected components and model the process as an RD system [5]. Atasoy et al. [6] embed anatomical constraints in terms of the graph Laplacian matrix of the SC matrix in the Wilson-Cowan equations to explain the macro-scale excitatory and/or inhibitory interactions of the regional activities. These excitatory and/or inhibitory interactions result in the formation of complex functional patterns such as RSNs. We extend our model from Atasoy et al. [6] and explain the formation of FC through RSNs. We hypothesize that the cumulative mean activities of all the regions is generated by intra-regional micro-scale dynamics which diffuses inter-regionally on the structural connectome. We propose a physical model that implicitly captures the pairwise functional interactions between ROIs by explicitly associating them with their extent of influence through the diffusion kernels on the SC.

4.3.1 Notations

Please refer to the table 4.1 for all the notations used in the MKL model.

4.3.2 Biophysics of the model

The derivation of the expression for FC consists of five major stages. We consider that FC matrix encompasses effects of diffusion from multiple reactions. In the first stage, we formulate the differential equation for the time evolution of regional activities (Eq. 4.5 - 4.7). In second stage, we characterize the time evolution of the regional activities in an arbitrarily small time interval (Eq. 4.8). In the third stage, we integrate the diffusion process over all the connectome harmonics (Eq. 4.9). In the fourth stage we accumulate the diffusions happening in various time intervals to generate the complete expression for FC (Eqs. 4.10 - 4.17). This FC assumes the form of a combination of diffusion kernels weighted by scale-specific parameters (Eq. 4.17). In the final stage, we propose an optimization framework for estimating these global parameters (Eqs. 4.18 - 4.19).

Let the cumulative mean activities for all regions be denoted by $\mathbf{u}(t)_{n\times 1}$ at time t. We assume that these activities belong to either excitatory and/or inhibitory interactions. The temporal evolution of regional activities are modeled as the following linear variant of Wilson-Cowan equations:

$$\tau \frac{\partial}{\partial t}\mathbf{u}(t) = -\mathbf{u}(t) + \mathcal{D}\left[\mathbf{u}(t)\right]. \tag{4.5}$$

where $\mathcal{D}$ is the spatial propagation operator. τ is a characteristic time scale that speeds up or slows down the evolution of the system. Mean activity of a region i, $u_i(t)$, can be abstracted out from biological details as a one-dimensional (1-D) time varying signal. A vector of these 1-D signals indexed by the nodes of the graph represents a *graph signal*. We represent the graph signal in terms of its Fourier components using graph Fourier transform [94]:

$$\mathbf{u}(t) = \mathbf{\Psi}\boldsymbol{\beta}(t), \tag{4.6}$$

where $\mathbf{\Psi}$ is the eigenvector matrix of graph Laplacian and $\boldsymbol{\beta}(t)$ is its Fourier representation at time t. With this decomposition temporal dynamics is explicitly represented using spatial basis functions. Further we conceptualize the spatial operator $\mathcal{D}$ in the form of a diffusion kernel defined at scale $\sigma^2/2$ on the structural brain graph Laplacian (Λ) corresponding to the time interval τ between two consecutive reaction instances:

$$\mathcal{D}[\mathbf{u}(t)] = \mathbf{\Psi}e^{-\mathbf{\Lambda}\,\sigma^2/2}\mathbf{\Psi}^\top\mathbf{u}(t) = \mathbf{\Psi}e^{-\mathbf{\Lambda}\,\sigma^2/2}\boldsymbol{\beta}(t). \tag{4.7}$$

Substituting Equations (4.6) and (4.7) and combining the fact that $\mathbf{\Psi}$ is invertible, differential Equation (4.5) can be solved for $\boldsymbol{\beta}(t)$ which represents the signal evolution in the time interval between two

Object	Description
n	Number of ROIs or the number of nodes in the brain graph.
p	Number of training subjects.
SC	Structural connectivity matrix.
SC^s	SC matrix for subject s.
D^s	Degree matrix for subject s; sum of edge weights for every region.
FC	Functional connectivity matrix.
FC^s	FC matrix for subject s. $[f_1^s, \cdots, f_n^s]$
$\mathbf{W}_{n\times n}$	Weighted adjacency matrix of a graph.
$\mathbf{D}_{n\times n}$	Degree matrix of a graph, computed by taking the sum of all weights on every node and diagonalizing the vector.
$\mathbf{L}^s_{n\times n}$	Laplacian matrix of subject s.
$\mathbf{\Psi}^s_{n\times n}$	Eigenvector matrix of the graph Laplacian of subject s.
$\mathbf{\Lambda}^s_{n\times n}$	Eigenvalue matrix, diagonal matrix with increasing order of eigenvalues, of the graph Laplacian of subject s.
γ_i	A scale at which diffusion kernel is defined.
$\mathbf{H}^s_{i\,n\times n}$	Diffusion kernel at scale γ_i for subject s.
m	Number of scales
$\mathbf{H}^s_{n\times mn}$	Collection of all m diffusion kernels of a subject s. $\begin{bmatrix}\mathbf{H}^s_{1\,n\times n} & \cdots & \mathbf{H}^s_{m\,n\times n}\end{bmatrix}$
$\boldsymbol{\pi}_{i\,n\times n}$	Interregional co-activations corresponding to scale γ_i.
$\mathbf{\Pi}_{mn\times n}$	Interregional co-activations collectively represented at all scales. $\begin{bmatrix}\boldsymbol{\pi}_{1\,n\times n}\\ \vdots \\ \boldsymbol{\pi}_{m\,n\times n}\end{bmatrix} = \begin{bmatrix}{\boldsymbol{\pi}^1}_{mn\times 1} & \cdots & {\boldsymbol{\pi}^n}_{mn\times 1}\end{bmatrix}$
$\boldsymbol{X}_{pn\times mn}$	$\begin{bmatrix}\mathbf{H}^1\\ \vdots \\ \mathbf{H}^p\end{bmatrix}$
$\boldsymbol{Y}_{pn\times n}$	$\begin{bmatrix}{\text{FC}^1}_{n\times n}\\ \vdots \\ {\text{FC}^p}_{n\times n}\end{bmatrix} = \begin{bmatrix}f_1^1 & \cdots & f_n^1\\ & \vdots & \\ f_1^p & \cdots & f_n^p\end{bmatrix} = \begin{bmatrix}Y_{1\,pn\times 1} & \cdots & Y_{n\,pn\times 1}\end{bmatrix}$
$\mathbf{C}^s_f$	Predicted FC $\sum_{i=1}^m \mathbf{H}^s_i \boldsymbol{\pi}_i$
$\mathbf{C}_f\vert_{k_0}$	Functional connectivity FC when reaction only happens at $k_0\tau$.

Table 4.1: **Notations**. The table shown here summarizes all the notations used in the models and optimization formulation in this chapter.

reaction instances, as follows:

$$\begin{aligned}\tau\ \boldsymbol{\Psi}\frac{d}{dt}\boldsymbol{\beta}(t) &= -\boldsymbol{\Psi}\boldsymbol{\beta}(t) + \boldsymbol{\Psi}e^{-\boldsymbol{\Lambda}\sigma^2/2}\boldsymbol{\beta}(t)\\ \frac{d}{dt}\boldsymbol{\beta}(t) &= -\frac{1}{\tau}(\mathbf{I}_n - e^{-\boldsymbol{\Lambda}\sigma^2/2})\boldsymbol{\beta}(t)\\ \boldsymbol{\beta}(t) &= e^{-1/\tau(\mathbf{I}_n - e^{-\boldsymbol{\Lambda}\sigma^2/2})t}\boldsymbol{\beta}_0,\end{aligned} \tag{4.8}$$

where $\boldsymbol{\beta}_0$ represents the initial mean activity. Equation (4.8) depicts how the mean activity ($\boldsymbol{\beta}_0$) of every region diffuses on the graph. Finally the graph signal between two reaction times can be expressed in a closed form as follows:

$$\mathbf{u}(t) = \boldsymbol{\Psi}e^{-1/\tau(\mathbf{I}_n - e^{-\boldsymbol{\Lambda}\sigma^2/2})t}\boldsymbol{\beta}_0 = \boldsymbol{\Psi}e^{-1/\tau(\mathbf{I}_n - e^{-\boldsymbol{\Lambda}\sigma^2/2})t}\boldsymbol{\Psi}^\top\mathbf{u}_0, \tag{4.9}$$

where, $\mathbf{u}_0 = \boldsymbol{\Psi}\boldsymbol{\beta}_0$ captures initial activity just after reaction, or at the start of diffusion. $\mathbf{u}_0$ depends on the magnitude of reaction phenomenon, hence may change after every reaction instance. Given the temporal evolution of graph signal, we will next derive how this leads to the evolution of functional connectivity and RSNs. RSNs have unique correspondence with graph-harmonics/eigenvectors of the structural graph Laplacian [6]. We develop the model for a single graph-harmonic, i.e., for all RSNs corresponding to that graph-harmonic. Finally, we superpose all the patterns of the resting state networks and explain the formation of FC.

The graph signal $\mathbf{u}_0$ may not change significantly in every reaction. Equation (4.9) represents the diffusive phenomenon of the graph signal over the characteristic time τ. Let $\mathbf{u}_0$ change significantly at scalar multiples of τ, i.e., $t + k_0\tau$, $t + k_0\tau + k_1\tau$, $\cdots$ with corresponding amplitudes $a_0, a_1, \cdots$, respectively. For now we consider generating the functional connectivity ($\mathbf{C}_f|_{k_0}$) for the time interval between two consecutive reactions; at times $t + k_0\tau$ and $t + k_0\tau + k_1\tau$:

$$\begin{aligned}\mathbf{C}_f|_{k_0} &= \int_{t+k_0\tau}^{t+k_0\tau+k_1\tau}\mathbf{u}(t)\mathbf{u}(t)^\top dt\\ &= \int_{t+k_0\tau}^{t+k_0\tau+k_1\tau}\boldsymbol{\Psi}e^{-1/\tau(\mathbf{I}_n - e^{-\boldsymbol{\Lambda}\sigma^2/2})t}\boldsymbol{\Psi}^\top(a_0\mathbf{u}_0)(a_0\mathbf{u}_0^\top)\boldsymbol{\Psi}e^{-1/\tau(\mathbf{I}_n - e^{-\boldsymbol{\Lambda}\sigma^2/2})t}\boldsymbol{\Psi}^\top dt.\end{aligned} \tag{4.10}$$

As $\mathbf{u}_0$ is also a signal on graph, we can express the positive semi-definite (PSD) matrix $\mathbf{u}_0\mathbf{u}_0^\top$ in terms of its eigen-decomposition. And as it is only a single harmonic, Δ is a diagonal matrix with only one non-zero entry as follows:

$$\mathbf{u}_0\mathbf{u}_0^\top = \boldsymbol{\Psi}\Delta\boldsymbol{\Psi}^\top. \tag{4.11}$$

Hence, $\mathbf{C}_f|_{k_0}$ takes the following form:

$$\begin{aligned}
\mathbf{C}_f|_{k_0} &= a_0^2 \int_{t+k_0\tau}^{t+k_0\tau+k_1\tau} \mathbf{\Psi} e^{-1/\tau(\mathbf{I}_n - e^{-\mathbf{\Lambda}\sigma^2/2})t} \Delta e^{-1/\tau(\mathbf{I}_n - e^{-\mathbf{\Lambda}\sigma^2/2})t} \mathbf{\Psi}^\top dt \\
&= a_0^2 \int_{t+k_0\tau}^{t+k_0\tau+k_1\tau} \mathbf{\Psi} e^{-2/\tau(\mathbf{I}_n - e^{-\mathbf{\Lambda}\sigma^2/2})t} \Delta \mathbf{\Psi}^\top dt \\
&= a_0^2 \int_{t+k_0\tau}^{t+k_0\tau+k_1\tau} \{\mathbf{\Psi} e^{-2/\tau(\mathbf{I}_n - e^{-\mathbf{\Lambda}\sigma^2/2})t} \mathbf{\Psi}^\top\} \{\mathbf{\Psi} \Delta \mathbf{\Psi}^\top\} dt \\
&= \mathbf{\Psi} \int_{t+k_0\tau}^{t+k_0\tau+k_1\tau} e^{-2/\tau(\mathbf{I}_n - e^{-\mathbf{\Lambda}\sigma^2/2})t} dt \; \mathbf{\Psi}^\top \{a_0^2 \boldsymbol{\theta}_{k_0}\}.
\end{aligned} \tag{4.12}$$

We can denote the initial activity matrix as $a_0^2 \boldsymbol{\theta}_{k_0}$. As reaction instances are not usually far apart in time, instead of double exponentiation we utilize the first order Taylor approximation for the exponent of the integrand; i.e. $\mathbf{I}_n - e^{-\mathbf{\Lambda}\sigma^2/2} \approx \mathbf{\Lambda}\sigma^2/2$. Hence, $\mathbf{C}_f|_{k_0}$ becomes:

$$\mathbf{C}_f|_{k_0} = (\mathbf{\Psi} e^{-\sigma^2/\tau \mathbf{\Lambda}(t+k_0\tau)} \mathbf{\Psi}^\top - \mathbf{\Psi} e^{-\sigma^2/\tau \mathbf{\Lambda}(t+k_0\tau+k_1\tau)} \mathbf{\Psi}^\top)(a_0^2 \tau/\sigma^2 \mathbf{\Lambda}^{-1} \boldsymbol{\theta}_{k_0}). \tag{4.13}$$

We call the matrix independent of time as

$$\boldsymbol{\pi}_0 = a_0^2 \frac{\tau}{\sigma^2} \mathbf{\Lambda}^{-1} \boldsymbol{\theta}_{k_0} \tag{4.14}$$

Now with multiple reactions happening at multiples of τ, we sum over all the reaction instances to get the functional connectivity matrix:

$$\mathbf{C}_f = \sum_i \mathbf{\Psi} e^{-\sigma^2/\tau \mathbf{\Lambda} k_i} \mathbf{\Psi}^\top \boldsymbol{\pi}_i, \tag{4.15}$$

where,

$$\boldsymbol{\pi}_i = (a_i^2 - a_{i-1}^2)\tau/\sigma^2 \mathbf{\Lambda}^{-1} \boldsymbol{\theta}_{k_i}. \tag{4.16}$$

Observing the structure of the FC matrix, FC is conceptualized as being represented by diffusion kernels and their corresponding inter-regional mean activities. So, the larger the value of k_i, the lesser is its contribution to FC. This means that summation on a finite number of diffusion scales is sufficient for reproducing FC (we considered 16 diffusion scales based on pilot simulations). Now after combining the functional patterns of all the graph-harmonics, we approximate empirical FC with m number of diffusion scales, γ_i's. The model thus takes the form as follows:

$$\begin{aligned}
\mathbf{C}_f &= \sum_{i=1}^{m} \mathbf{\Psi} e^{-\mathbf{\Lambda}\gamma_i} \mathbf{\Psi}^\top \boldsymbol{\pi}_i \\
&= \sum_{i=1}^{m} \mathbf{H}_i \boldsymbol{\pi}_i,
\end{aligned} \tag{4.17}$$

where $\mathbf{H}_i$ denotes the diffusion kernel at scale γ_i. Further the model in Equation (4.17) suggests that the scale of diffusion is determined by a characteristic time constant (τ), spatial diffusion variance (σ^2) and

the time interval between consecutive reaction instances. Matrix $\boldsymbol{\pi}_i$ represents the scale-specific initial relationships in the mean regional activities. Proposed model represents the functional connectivity in terms of diffusion kernels operating on scale-specific matrices. It can be inferred that Adelnour et al. [2] envisage FC comprising only one diffusion kernel defined at an optimal scale. The optimal kernel operates on an identity matrix; meaning only the concerned region has non-zero mean activity independent of other regions. Surampudi et al [97] demonstrated that FC can be decomposed into multiple diffusion kernels whose combination coefficients are unique to the cohort. In addition to the multiple scales, proposed model provides inter-regional relationships instead of individually active regions. The proposed model generalizes both the aforementioned models as statistical dependence between two regions may be modulated by some intermediate regions without physical proximity that too at multiple resolutions or scales. Moreover, the model provides a biological interpretation of the diffusion scales and has an organic relationship to the reaction-diffusion system.

4.3.3 Optimization framework

We hypothesize that the global parameters $\boldsymbol{\pi}_i$'s are estimated from the training subjects (indexed by s and varies from 1 to p) and remain fixed for all the test subjects. In order to estimate $\boldsymbol{\pi}_i$'s we utilize an optimization formulation that minimizes an objective function J comprising the mean squared error between empirical and predicted FCs.

$$\begin{aligned} \mathrm{J}\ ^{1} &= \sum_{s=1}^{p} \|\mathbf{C}_f^s - \mathrm{FC}^s\|_F^2 \\ &= \sum_{s=1}^{p} \|\sum_{i=1}^{m} \mathbf{H}_i^s \boldsymbol{\pi}_i - \mathrm{FC}^s\|_F^2 \\ &= \sum_{s=1}^{p} \|\mathbf{H}^s \boldsymbol{\Pi} - \mathrm{FC}^s)\|_F^2 \end{aligned} \tag{4.18}$$

where, $\|\cdot\|_F$ denotes the Frobenius norm, $\mathbf{H}^s = \left(\mathbf{H}_1^s, \cdots, \mathbf{H}_m^s\right)$, and $\boldsymbol{\Pi} = \left(\boldsymbol{\pi}_1^\top, \cdots, \boldsymbol{\pi}_m^\top\right)^\top$. Let, $\boldsymbol{X} = \left(\mathbf{H}^{1\top}, \cdots, \mathbf{H}^{p\top}\right)^\top$, and $\boldsymbol{Y} = \left(\mathrm{FC}^{1\top}, \cdots, \mathrm{FC}^{p\top}\right)^\top$. We solve this objective function one column at a time, and to keep the activation matrix sparse, we employ L_1 norm on each of the j^{th} column of $\boldsymbol{\Pi}$, i.e. $\boldsymbol{\Pi_j}$:

$$\mathrm{J} = \sum_{j=1}^{n} \|\boldsymbol{X}\boldsymbol{\Pi}_j - \boldsymbol{Y}_j\|_F^2 + \lambda\|\boldsymbol{\Pi}_j\|_1, \tag{4.19}$$

where $\boldsymbol{Y}_j$ is the j^{th} column of $\boldsymbol{Y}$. The objective function takes the form well known in regression analysis as *least absolute shrinkage and selection operator* (LASSO) that performs both variable selection and regularization.

[1] The equations here are corrected version of the optimization formulation. Equations in SciRep need an erratum.

4.4 Results

4.4.1 Model performance

We compared performance of the proposed model with two previously proposed approaches: single-diffusion-kernel (SDK) model of Abdelnour et al. [2] and the non-linear dynamic-mean-field (DMF) model described in Deco et al. [36]. To remain consistent with the previous studies, we used Pearson correlation coefficient between empirical and predicted functional connectivities (FC) as the measure of model performance. To obtain a benchmark, we computed the Pearson correlation between empirical SC-FC pairs for all subjects and found mean value for these correlations to be 0.3 with a standard deviation of 0.02. These values are taken as baseline correlation values henceforth.

Fig. 4.1 shows the performance comparison of the proposed method with other two models in three different setups. In the first setup, a randomly chosen set of half of the subjects was used for training (23 pairs) and the other half (23 pairs) for testing. Fig. 4.1(a) shows the model performance for all the test participants for the three models. Since SDK and DMF models do not incorporate learning in their formulation, we gleaned the optimal values based on the training subjects. The optimal parameter settings were taken as the values at the mode of the performance distribution histogram for the training set and the same were used for estimating FC for test subjects. We took the best fitting scale on the training subjects for the SDK model and similarly selected the optimal global coupling parameter, G, for the DMF model. Optimal scale for SDK model worked out to be 0.8 and similarly optimal value of G for DMF was 2.85.

As can be seen from Figs. 4.1(a) and 4.1(b), the MKL model performs consistently better for each test subject when compared to the other two models. In the remaining two setups, in order to crosscheck whether MKL model suffers from over-fitting, we computed leave-one-out (Fig. 4.1(b)) and 5-fold cross-validation (Fig. 4.1(c)) results. These results clearly show the consistency in the performance of MKL model and indicate that the performance is not due to over-fitting nor it is due to any particular optimistic train-test split.

In all the experiments and for all the three models in order to compare group statistics, we compute the predicted FC for each test subject and then find the Pearson correlation coefficient with the corresponding empirical FC, followed by taking the mean of all these correlation coefficients. We designate the resulting mean correlation as mean FC in the rest of the paper.

4.4.2 Edge-based and Seed-based Connectivity Analysis

Mean FCs are visualized primarily in two modes, via the edge-connectivity pattern analysis and using the seed-based connectivity analysis. To understand the edge and node distribution across the communities, we rendered the mean predicted FCs on brain surface. The visualization of edge-connectivity patterns of four mean FCs is shown in Fig. 4.2. In the figure, the colors demarcate the communities for a particular model on the corresponding brain surface. It can be seen that the community structure of the mean FC predicted by the MKL model (shown in Fig. 4.2(b)) best resembles that of the mean

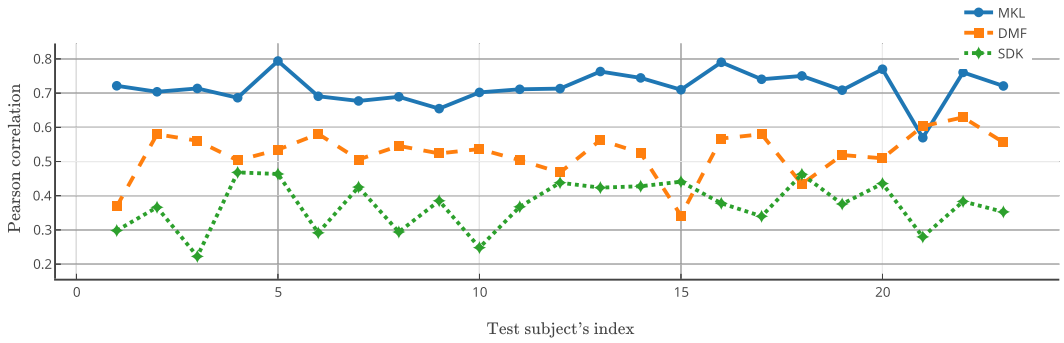

(a) Performance of models.

(b) Leave-one-out validation.

(c) 5-fold cross-validation

Figure 4.1: **Comparison of Model Performance on Individual Test subjects.** (a) Pearson correlation between empirical and predicted FCs of all the test subjects by multiple kernel learning (MKL) model and performance comparison with the predictions by the other two models. While MKL model has superior performance compared to that of dynamic mean field (DMF) and single diffusion kernel (SDK), DMF model performs slightly better than the SDK model. (b) Results of leave-one-out cross-validation on the test subjects also yield similar comparative performance. Note that the subject indices are kept identical between sub-figures (a) and (b). This plot suggests that MKL model can handle an increase in the number of training subjects without necessarily any over-fitting. (c) Box-plots of Pearson correlation measure on 9 randomly chosen validation subjects for each of the 5 folds for the MKL model. Points lying outside the quartiles are the suspected outliers. Compactness of boxes suggests inter-subject consistency of model's performance. Further, these 5-fold cross-validation results suggest that MKL model performs consistently well on unseen subjects.

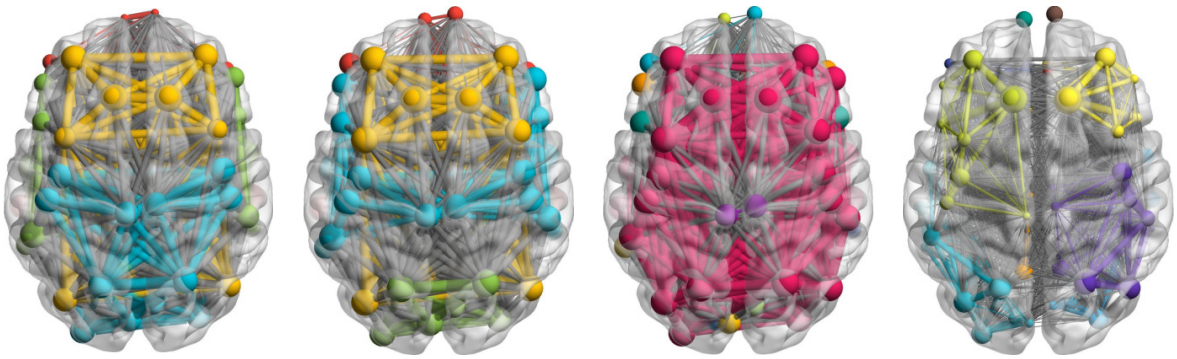

(a) Emp **(b)** MKL **(c)** DMF **(d)** SDK

Figure 4.2: **Functional Connectivity (FC) Networks Derived from Group-Mean FCs of the Test Dataset**. The mean FC networks depict edge-connectivity patterns for (a) Empirical FC and FCs predicted by (b) MKL model; (c) DMF model [36]; and (d) SDK model [2], respectively. Note the similarity of the MKL model and the empirical FC in terms of community assignment and inter-hemispheric connections. DMF model predicts a denser network while the single scale model predicts coarser network than the empirically observed FC. Brain-net-viewer [113] was used for visualization of the four communities detected from the Louvian algorithm available in brain-connectivity-toolbox [87]. Colors of the edges and nodes are only to demarcate the communities observed and do not have any correspondence across brain surfaces for different models. Thus the comparison of community structure across models is qualitative in nature.

empirical FC (shown in Fig. 4.2(a)). The other two models predict either a denser FC network (as shown in Fig. 4.2(c) for the DMF model) or a sparser FC network (as shown in Fig. 4.2(d) for the SDK model), where both the scenarios are far from the empirically observed network. Additionally, the predicted mean FC by MKL model and the empirical mean FC seem similar in terms of community assignment and inter-hemispheric connections.

Further, to see element-wise variance in the mean predicted FCs, we also drew scatter plots between the predicted and empirical FCs in Fig. 4.3, where only the non-diagonal lower triangular matrix entries were displayed. These plots suggest that MKL model preserves the global structure of the empirical FC as well as the element-wise connectivity patterns significantly better than the other models.

To further validate the nature of reconstruction of the connectivity patterns for various ROIs, we performed a seed-based correlation analysis using the mean FC matrices predicted from the three models. We chose the left posterior cingulate cortex (PCC) as a seed region since it has been known to have an important functional role as a hub region of the default mode network [28]. Fig. 4.4 plots the correlation values between left PCC and all other regions on the brain surface reconstructed from the Desikan-Killiany atlas [38]. Cool (hot) colors suggest low (high) connectivity (correlation) of that particular region with the left PCC (shown as dark red color in the mean empirical FC). The MKL model could reconstruct the connectivity pattern with higher precision than the other two models. It appears that due to very high correlation of left PCC with all other regions, DMF model could not as clearly distinguish

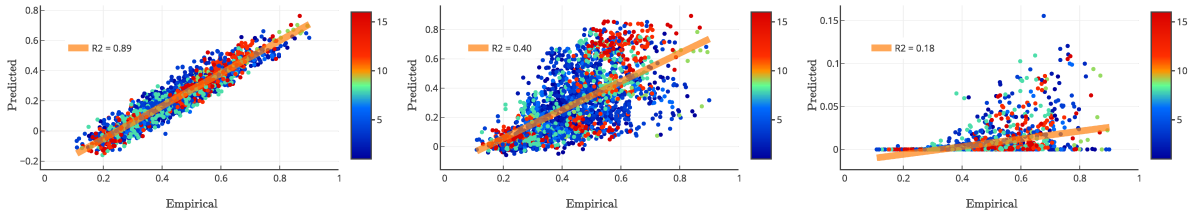

(a) MKL **(b)** DMF **(c)** SDK

Figure 4.3: **Comparison of Scatter Plots**. Scatter plots for mean FCs of the test-subject-wise empirical vs predicted FCs for (a) MKL; (b) DMF; and (c) SDK models. Only the non-diagonal lower triangular matrix from all the FCs has been taken to generate the plots. Each connection was identified as belonging to one of the four different lobes represented by their color codes; resulting in 16 colors representing 4×4 inter-hemispheric connections. Higher R^2 value for the MKL model suggests tighter bound on the element-wise error while predicting FC. Even though prediction of DMF model appears to be closer to that of MKL model, predicted elements are much more scattered for the DMF model.

the boundary between regions. SDK model could not possibly distinguish them due to very sparse connectivity between left PCC and all other regions.

4.4.3 Effect of Thresholding

The rich-club organization of the structural connectivity (SC) matrix is previously demonstrated to be the backbone for generating the functional connectivity patterns [103, 25, 91]. Therefore we set out to investigate the impact of using thresholded SCs for predicting FCs. We pruned the SCs of all subjects by keeping only top T% of the connections. Each of these sparse matrices was passed as input to the learned MKL model. For each sparse SC, corresponding FC was predicted. Pre-learned $\boldsymbol{\pi}_i$'s were used for predicting FCs in the MKL model. Similarly, fixed diffusion scale and G parameters were used for SDK and DMF models for comparative evaluation. Fig. 4.5 shows the mean correlation between empirical FC and predicted FCs for each of the sparse SC matrices. As can be seen, DMF and SDK models attain their respective optimum performance even when only few (as low as 10%) strongest edges in SC remained.

On the other hand, MKL model requires both strong edges and few local edges, and hence its performance starts increasing from $\mathrm{T} = 15\%$ and is significantly superior at all thresholds above this value. This result suggests that functional patterns may be primarily decided by the initial co-activations captured by $\boldsymbol{\pi}_i$'s and that the structural constraints of individual SCs provide paths for these activities to diffuse, giving support to our hypothesis. Nevertheless, stable performance with sparsification as high as with $\mathrm{T} = 20\%$ indicates that all the models obey the basic rich-club principle.

Interestingly, MKL model captures the differences in sparsity levels better when compared to the other two models, especially when SC was pruned to keep the strongest edges between $10 - 20\%$. This behavior suggest that pre-trained $\boldsymbol{\pi}_i$'s in MKL model do not compensate for major loss of information in sparsified SCs, thereby indicating avoidance of overfitting.

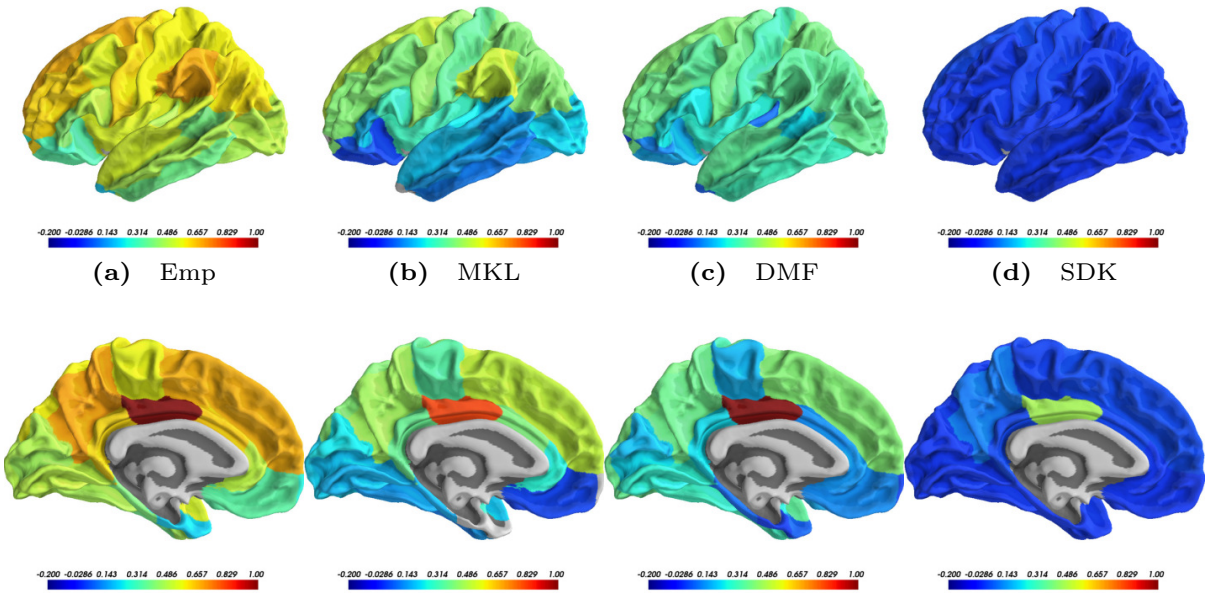

(a) Emp **(b)** MKL **(c)** DMF **(d)** SDK

(e) Emp **(f)** 0.71 **(g)** 0.52 **(h)** 0.37

Figure 4.4: **Results of Seed-based Correlation**. Mean correlation maps resulting from considering the left Posterior Cingulate Cortex as a seed region and then calculating the seed-based correlations of all other regions. These maps are rendered on the left lateral sagittal view in the top sub-figures (a)-(d) and on the medial sagittal surface in the bottom sub-figures (e)-(h). While sub-figures (a) and (e) depict the maps for Empirical FC, the maps from the predicted FCs of MKL model are in (b) and (f); those of DMF in (c) and (g); and those of SDK in (d) and (h), respectively. Captions in the top row mention the model name and those in the bottom row indicate the mean correlation value on the test subjects. As can be observed, the correlation maps of MKL model seem to have greater correspondence with those of the mean empirical FC. Moreover, as depicted by the contrasts in the colors, MKL model is able to distinguish between the correlations at a better resolution than the other two models.

To keep edges more than T% of the maximum edge weight, we defined $0 \leq \epsilon \leq 1$ as the factor for thresholding. Based on the mean SC, we selected 6 values for ϵ which are (0.0960, 0.0657, 0.0354, 0.0152, 0.0051, 0.0000) and applied them to get the thresholded empirical SCs. We only selected elements of SC above ϵ times the maximum value of SC. This mask was applied on SC to generate the set of thresholded SCs. Equation 4.20 describes the process succinctly in the form of a MATLAB® pseudocode statement.

$$\text{SC} \leftarrow (\text{SC} > \epsilon \max(\text{SC})) \odot \text{SC}, \tag{4.20}$$

where $\odot$ is element-wise product.

4.4.4 Robustness of the MKL Model

The proposed model learns a latent representation, $\mathbf{\Pi}$ that maps the relationship between SC and FC. This being the crucial difference between MKL and other models, we performed extensive robustness

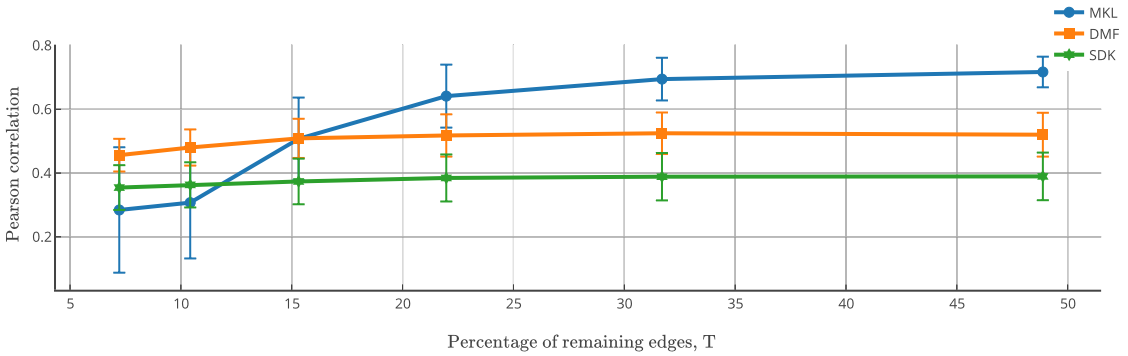

Figure 4.5: **Model Performance on Sparse / Thresholded SCs**. Structural Connectivity (SC) matrices for each subject were sparsified using 9 sparsification values. The three models were tested using these sparsified SCs. The plot shows the mean correlation values along with the standard deviation across subjects at each sparsification level. While MKL model was pre-trained with the un-sparsified SCs, a single optimal parameter was derived from the training data for each of the DMF and SDK models and used for estimating FC for the test subjects. The performance of MKL model starts to be superior after the sparsification level of 15% of the remaining edges. It appears that since MKL model selects the scales closely based on the SCs, the model performance degrades at very high sparsification levels.

tests to verify the usefulness of learning the $\boldsymbol{\pi}_i$'s. To ascertain that the model's representation learns important features and does not capture the SC-FC mapping by chance, we conducted the following four randomization experiments. In the first one we randomize the input to the model (i.e., SCs) (see Fig. 4.6) and in the second the learning itself is conducted based on perturbed SCs. In the third experiment we disturb the scale-specific relation between the learned $\boldsymbol{\pi}_i$'s and $\mathbf{H}_i$'s (see Eq. 4.17) and finally in the fourth experiment the constituent rows of $\boldsymbol{\pi}_i$'s are randomly permuted (see Fig. 4.8).

4.4.4.1 Procedure for perturbation of input

We generated random SC matrices respecting the power law distribution of the connectivities of the ROIs. These are the following steps:

1. We assume that power law distribution takes the form $p_K(k) = k^{1/\alpha+1}$. k being the edge value. We chose α as 2.

2. We generated a random matrix using uniform distribution and applied this function element-wise on the random matrix.

3. Addition of the transpose to itself followed by division with the maximum matrix element provides us with a random SC.

4. We repeated this procedure for all the subjects 250 times.

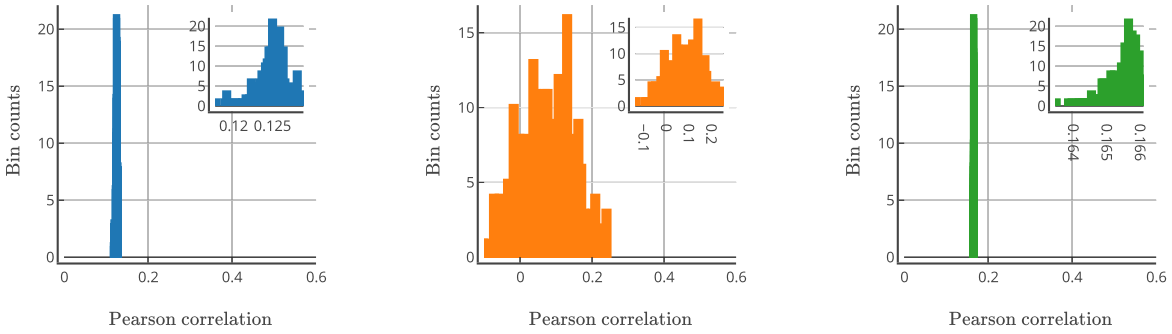

(a) MKL **(b)** DMF **(c)** SDK

Figure 4.6: **Model Performance with Perturbed Structural Connectivity (SC) Matrices.** Randomly perturbed SCs ($N = 250$ sets) of the test subjects were used for estimating the FCs with the trained models. Sub-figures depict histograms of model's mean performance (Pearson correlation between empirical and predicted FCs): (a) MKL; (b) DMF; and (c) SDK model, respectively. The sub-plots (top right corners) within these sub-figures zoom in on the histograms for clarity. As expected, all the models depict degradation in performance with perturbed SCs.

4.4.4.2 Perturbing the model input

To verify whether the model learns the SC-FC relationship correctly or predicts the average FC independent of SC, we provided the MKL model with perturbed SCs in two possible scenarios: first, while testing, and second, while training.

Each subject-wise SC was perturbed $N = 250$ times, hence forming 250 sets of subject-wise perturbed SC-empirical FC pairs. In the first perturbation analysis, we trained the MKL model with the original subject-wise training SC-FC pairs, and tested the model with these 250 perturbation sets. These same sets were used for evaluating the other two models. We calculated the mean correlation values between predicted and empirical FCs, thus obtaining 250 mean correlation values for every model. Figs. 4.6(a), 4.6(b), and 4.6(c) show the histograms of these mean correlation values for MKL, DMF and SDK models, respectively. As expected, all the three models have significant drop in their performance indicating their sensitivity towards meaningful SC matrices while arriving at predictions.

In the second perturbation analysis, we trained $N = 250$ MKL models using the 250 perturbed sets and evaluated them using the subject-wise empirical SC-FC pairs. We did not have to perform this analysis for the other two models as this analysis is the same as that of the above for these models. Fig. 4.7 shows the histogram of the 250 mean correlation values that is distributed across a wide range of correlation values instead of peaking at a particular value, thus indicating a *garbage-in, garbage-out* phenomenon from a machine learning perspective! This result, along with the results in Fig. 4.5, demonstrate that MKL model is not learning just a transformation from a subgraph of SC to an average FC but that the learning is holistic.

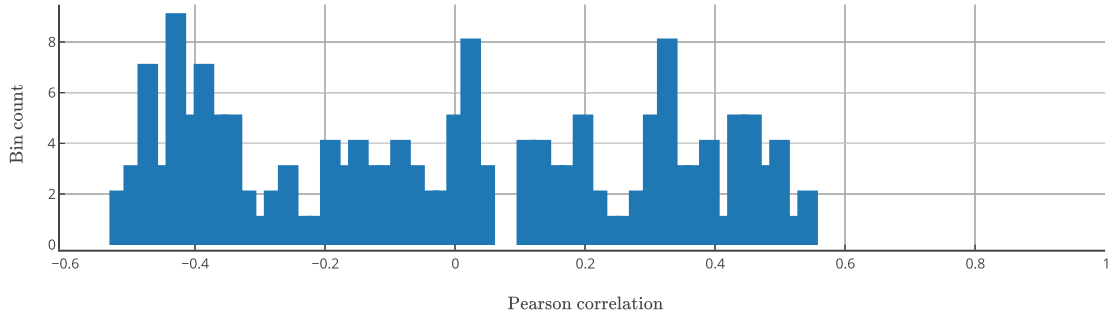

Figure 4.7: **Input perturbation while training MKL model**. The 250 perturbed sets of SCs were used train independent MKL models. These trained models were used for testing with the correct test SC-FC pairs. Histogram shows the mean performances across all the sets. As observed, most of the mean correlations are around -0.2.

4.4.4.3 Altering the model parameters

After confirming that the model does not learn a random mapping between SC-FC pairs, we alter the learned mapping to further confirm model's robustness. We considered two ways of altering the model parameters ($\boldsymbol{\pi}_i$'s). These parameters are mathematically represented as a set of m matrices ($\boldsymbol{\pi}_i$'s) corresponding to m diffusion scales (m here is set to 16, also see Equation 4.17). We sought to experimentally verify that $\boldsymbol{\Pi}$ can be interpreted as holding complementary information of a cohort of SCs. Hence it is likely that any perturbation of $\boldsymbol{\Pi}$ would disturb the synergistic correspondence to empirical SCs and cause performance degradation. In order to experimentally validate this intuition, we ran two types of permutation tests.

Firstly, we sought to estimate the importance of the arrangement of $\boldsymbol{\pi}_i$'s, i.e., the ordering of the scale-specific matrices constituting $\boldsymbol{\Pi}$. For this we swapped every matrix $\boldsymbol{\pi}_i$ $(1 \leq i \leq m)$ one at a time with $\boldsymbol{\pi}_m$ (corresponding to the lowest scale, i.e., $\boldsymbol{\pi}_{16}$). Fig. 4.8(a) shows the mean correlation while performing swapping. Pearson correlations are plotted against the swapped indices. Because of no-swap the last correlation (corresponding to $i = 16$) depicts optimal performance. The sub-figure suggests that indeed the constituent parameter matrices share their similarity with their corresponding scales. Constituent matrices learnt against larger scales of diffusion ought not be similar to those against local scales of diffusion. Component of $\boldsymbol{\pi}$ corresponding to global scale of diffusion represents co-activation patterns of regions topologically far apart, and component of $\boldsymbol{\pi}$ corresponding to local scales capture co-activations in the neighborhood . Thus, this is an empirical verification that when swapped performance of the model decreases. This plot suggests that indeed matrices have positional significance (in other words, scale-specificity), so they cannot be reorganized to predict FC. This is a property that is also subtly captured in Equation (4.17) in the sense that these matrices have a strict correspondence to their scales, consequently they embed scale-specific diffusion kernels to enable correct prediction of FC.

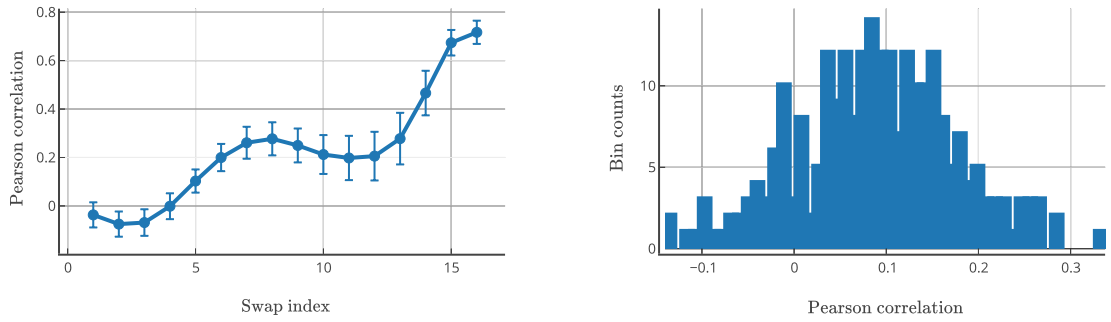

(a) Constituent matrices of $\mathbf{\Pi}$ are swapped with the lowest scale constituent matrix.

(b) Histograms of Pearson correlations when $\mathbf{\Pi}$ is altered. Rows of constituting $\mathbf{\Pi}$ are permuted.

Figure 4.8: **Investigation of the Impact of Altering the Scale-specificity of the Parameters π's**. Two studies are conducted where the first study (a) looks at the impact of changing the scale-specificity of the $\boldsymbol{\pi}$'s and the second study (b) looks at the impact of a larger-scale alteration when the components of individual $\boldsymbol{\pi}$ matrices are themselves altered. (a) This sub-figure depicts the result of swapping each of the $\boldsymbol{\pi}_i$ matrices with the last matrix, i.e., with $\boldsymbol{\pi}_{16}$. For example, the first data point shows the mean performance when $\boldsymbol{\pi}_1$ is swapped with $\boldsymbol{\pi}_{16}$, the second data point corresponds to the case when $\boldsymbol{\pi}_2$ is swapped with $\boldsymbol{\pi}_{16}$ and so on for each of the 16 $\boldsymbol{\pi}_i$ matrices being swapped with the last matrix $\boldsymbol{\pi}_{16}$. Thus the last data point corresponds to the case when the original order was retained. The error bars represent the standard deviation. The results suggest scale-specificity of the learned parameters, i.e., in the sense that the performance degrades drastically if the $\boldsymbol{\pi}$ matrices of one scale are swapped with a $\boldsymbol{\pi}$ matrix of a distant scale. (b) The histogram of Pearson correlations depicts the performance when all the $\boldsymbol{\pi}_i$ matrices are stacked together and the rows of the resulting stacked $\mathbf{\Pi}$-matrix are swapped randomly 250 times. Such global alteration drastically degrades the performance. Together, these results indicate that the learned parameters do not predict FCs by chance but play a crucial role in the MKL model.

Secondly, we sought to estimate regional importance of the entries of $\boldsymbol{\pi}_i$ matrices across scales. We concatenate all m $\boldsymbol{\pi}_i$'s into a single matrix ($\mathbf{\Pi}$) of size $mn \times n$. We permute the rows of this matrix and test the model performance. A row of $\mathbf{\Pi}$ captures regional co-activations at that scale between the region corresponding to that row and all other regions. In this sense, this analysis amounts to permuting the rows of the $mn \times n$ matrix. We permute the rows of this large matrix 250 (N). Each newly generated $\mathbf{\Pi}$ is used for testing the model performance. Fig. 4.8(b) shows the histogram of the mean correlations of all the N permutations. Clearly the plot shows that permuted $\mathbf{\Pi}$ significantly deteriorates the model performance. This figure underlines the importance of maintaining the structure of co-activation between pairs of regions.

4.5 Application of MKL for Identifying Inter-group Variations

Here we describe an application using $\mathbf{\Pi}$. We used $\mathbf{\Pi}$ to learn the functional patterns in two age groups, young and old. Before learning $\mathbf{\Pi}$'s for both age groups, we sought to validate the requirement

of multiscale model instead of a single-scale one. We are using the dataset after thresholding the SC matrices. The data set comprises of young-age group covering ages less than 30 years and old-age group comprising more than 50 years. Fig. 4.9 shows Pearson correlation curves for subjects categorized by their age groups. Albeit data tends to satisfy single-scale hypothesis, the optimum scale seems to be same for both the age-groups. However, the scales and the actual $\mathbf{\Pi}$'s for the two age groups are significantly different as can be inferred from Figure 4.10.

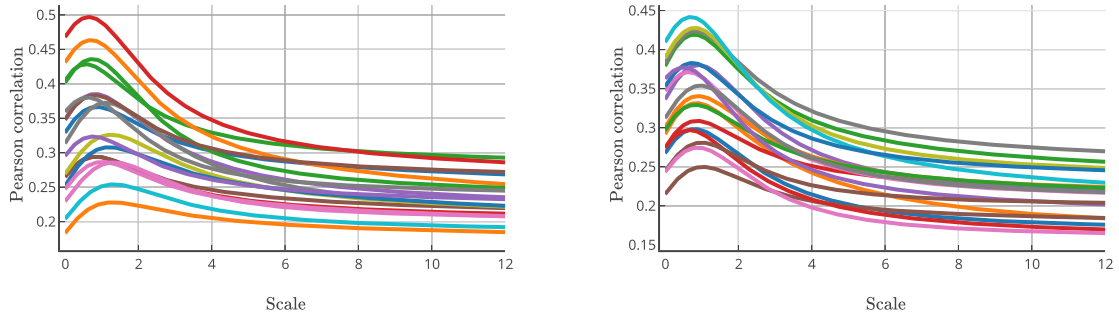

(a) Young age group **(b)** Old age group

Figure 4.9: **Inter-group variations**. Pearson Correlation curves for two age groups: (a) Young age group; (b) Old age group. Looking at the figure, it is difficult to comment on the age group of the subject.

Figure 4.10 shows the differences $\mathbf{\Pi}$ captures between the two age groups. Clearly, elements of $\mathbf{\Pi}$ span different ranges at global scales and these ranges come closer near local scales of diffusion (that is, for higher indices in Figure 4.10). Moreover, different regions participate in diffusion process in the young and old age groups. We call $\mathbf{\Pi}$ learned from young age group as $\mathbf{\Pi}_{young}$ and similarly that from old group as $\mathbf{\Pi}_{old}$. To further highlight the differences, we used $\mathbf{\Pi}_{young}$ and $\mathbf{\Pi}_{old}$ for predicting subject specific FCs. Fig. 4.11 captures the predictive power of $\mathbf{\Pi}$'s learned separately for the two age groups. We compared subject-wise Pearson correlations with the native and other age group's $\mathbf{\Pi}$. The two plots clearly show that native $\mathbf{\Pi}$'s predict subject-specific FCs better than other group's $\mathbf{\Pi}$'s.

4.6 Model Inversion

This section describes a procedure to recover the structural connectivity (SC) from the functional connectivity (FC) data, given $\mathbf{\Pi}$. The procedure is very simple and described in the following steps.

1. Find the set of diffusion kernels for subject s by solving the linear system of equations.

$$[\boldsymbol{\pi}_1, \cdots, \boldsymbol{\pi}_m] \begin{bmatrix} \mathbf{H}_1^s \\ \vdots \\ \mathbf{H}_m^s \end{bmatrix} = \mathrm{FC}^s. \tag{4.21}$$

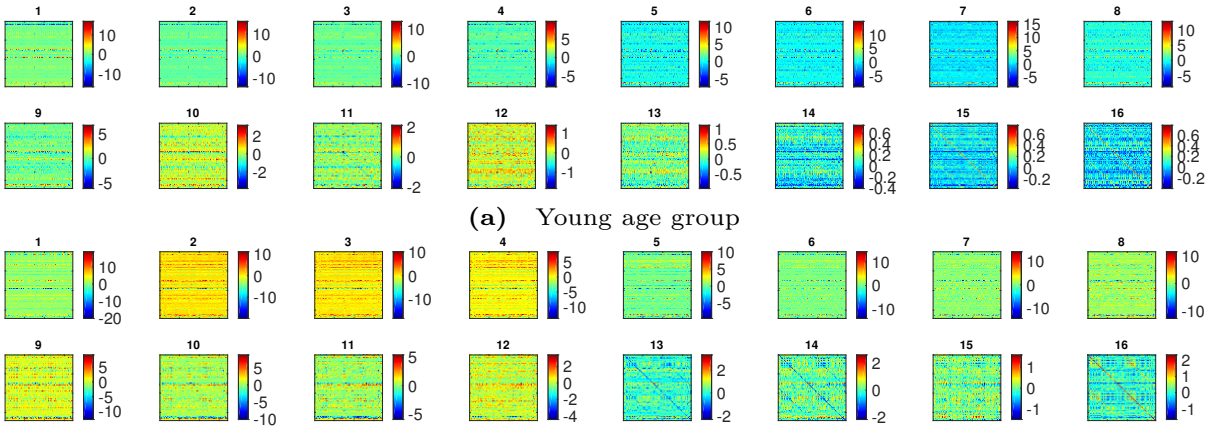

(a) Young age group

(b) Old age group

Figure 4.10: **Age-group specific Π's**. Different age groups learn significantly different **Π**'s. Clearly, the set of regions influencing other regions are different in both the age groups. Moreover, ranges of **Π**'s even for individual scale-components are also different. The numbers in the title of each sub figure index the scale-components. Thus, **Π** can be considered as a viable model for classification.

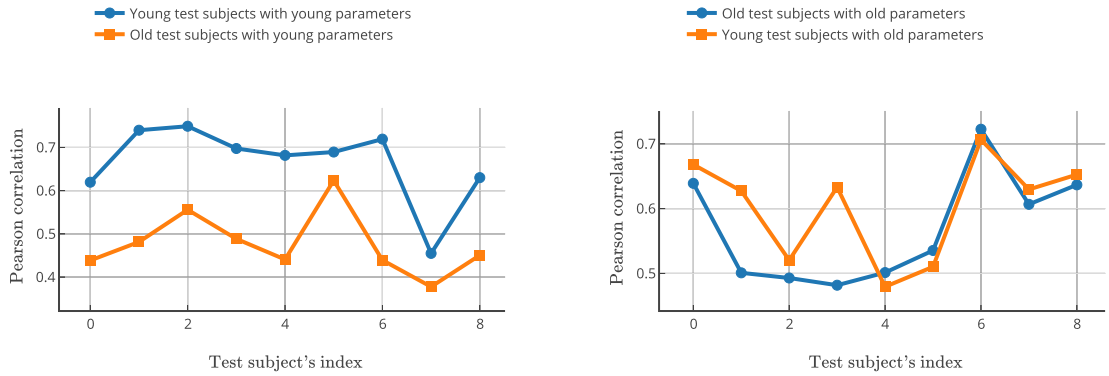

(a) Young age group.

(b) Old age group.

Figure 4.11: **Comparing the performances of the learned Π's on both age-groups**. Performance of the young age group was tested on both $\mathbf{\Pi}_{young}$ and $\mathbf{\Pi}_{old}$. Similarly old age group's performance was also tested with both the **Π**'s. As seen, **Π**'s capture behavior of both groups and are able to distinguish between them.

2. As the set of exponential values is known, and we choose second index of eigenvalues for finding the scale set; when each diffusion kernel is eigen-decomposed, the second eigenvalue of these $\mathbf{H}_i$'s should be 1.

$$\mathbf{H}_i^s = e^{-\mathbf{L}^s \gamma_i} = \mathbf{\Psi}^s e^{-\mathbf{\Lambda}^s \gamma_i} \mathbf{\Psi}^{s\top} \tag{4.22}$$

$$\mathbf{\Lambda}^s = \begin{bmatrix} \lambda_1^s/\lambda_2^s & & & \\ & 1 & & \\ & & \ddots & \\ & & & \lambda_1^s/\lambda_2^s. \end{bmatrix} \tag{4.23}$$

3. Laplacian $\mathbf{L}^s$ can be obtained from the eigenvector-eigenvalue matrices obtained from the previous step.

$$\mathbf{L}^s = \mathbf{\Psi}^s \mathbf{\Lambda}^s \mathbf{\Psi}^{s\top} = \mathrm{D}^s - \mathrm{SC}^s.$$

4. Removing the diagonal entries of $\mathbf{L}^s$ and negating the remaining values, we obtain SC^s.

Note that this method has some numerical inconsistencies which need to be resolved before it can be deployed.

4.7 Discussion

The holy grail in cognitive neuroscience is understanding how the static brain structure gives rise to dynamic function both during rest and task conditions. Several models have been proposed to characterize the structure-function relationship [81]. Simple linear diffusion models [2, 89] as well as complex non-linear, whole-brain computational models [36] have been proposed. Linear graph models [2] admit closed form deterministic and testable solution to macroscopic interactions of brain activity without requiring any details of neural coding or their biophysical substrate. On the other hand nonlinear complex drift-diffusion models based on excitatory and inhibitory neuronal populations, though not analytically tractable, give rise to rich dynamics [36].

Abdelnour et al. [2] conceived a model of functional connectivity (FC) with only one diffusion kernel defined at an optimal scale. This optimal kernel operates on an identity matrix, meaning that the amount of activity reaching other regions from a single source is representative of the statistical dependence between those regions. This statistical dependence resembles activity heat maps which exhibit inter-individual variations. However, Surampudi et al. [97] showed that single kernel models do not generalize to a larger cohort and demonstrated that FC can be decomposed into multiple diffusion kernels with subject non-specific combination coefficients.

We proposed a *multiple kernel learning* (MKL) method that learns inter-regional co-activations (denoted as $\boldsymbol{\pi}_i$'s) and reshapes the structurally confined diffusion kernels to give rise to functional

connectivity estimates. MKL model is a generalization of the SDK diffusion model. Resting state functional connectivity could be considered as a signal on a brain graph expressed at multiple different spatio-temporal scales. Our approach essentially finds a way to unfold these solutions on the brain graph combining multiple scales to accurately estimate the empirical FC. One way to interpret the proposed multi-scale diffusion model is to treat it as a variant of a reaction-diffusion system on the graph determined by the underlying structural connectivity (SC) matrix.

We adopt the representation of the graph signal in terms of eigenvectors of the graph Laplacian similar to what has been recently proposed [6]. The proposed MKL framework devises a scheme for learning the hidden parameters ($\boldsymbol{\pi}_i$'s) to estimate FC. The initial regional activity $\mathbf{u}_0$ in the reaction-diffusion type model is a vector, hence the matrix $\mathbf{u}_0\mathbf{u}_0^\top$ is a rank 1 matrix. As it is a positive semi-definite (PSD) matrix, it will only have one non-zero eigenvalue. Eigen-decomposition in Eq. (4.11) suggests a possible physical interpretation, that the initial mean activity distribution, an eigenvector of the graph Laplacian, resembles standing wave patterns on the graph. Total number of such standing waves is equal to the number of nodes of the graph. Hence our hypothesis is that the initial regional co-activations ($\boldsymbol{\pi_i}$'s) correspond to one of the standing waves present at some time $k_i\tau$ significantly changing the pattern at that reaction instance (please refer to subsection 4.3.1 for notations). Functional connectivity can then be articulated as a superposition of such standing wave patterns and their regional co-activations.

In order to predict FC from the proposed diffusion model, we estimated $\mathbf{\Pi}$ by solving a LASSO optimization formulation. We hypothesized that these hidden parameters are learnable from the training data and remain fixed at the time of testing. Consequently different FC matrices for the test subjects would be arising by virtue of the underlying differences in the respective structural connectivity matrices (SCs). This would mean that the parameters $\mathbf{\Pi}$ are not merely a derivative of SCs but instead they complement the missing aspects by capturing the statistical dependence between two regions that are modulated by some intermediate region that may not be in physical proximity and that too operating at multiple resolutions or scales. Thus by incorporating the inter- and intra-hemispheric functional connectivity terms for a brain region, the learned optimal $\mathbf{\Pi}$ parameters enable more accurate matching of the structure-function correlation. All the computational models can be visualized to lie on the spectrum spanned by biological interpretability and analytical ease. Whereas linear models enjoy simplicity of solution of their models, non-linear models tend to explain the complex biological reality. MKL model seems to find a sweet spot and enjoys best of both by analytically providing the solution and explaining the patterns in terms of large-scale excitatory-inhibitory interactions. Since LASSO optimization is the most expensive computational step, the computational complexity of the proposed MKL model would be dominated by the cost of LASSO optimization.

In summary, on the model continuum, the proposed MKL model lies somewhere between simple linear, SDK diffusion models [89, 2] and complex non-linear drift diffusion models [36]. Consequently, we compared our simulation results predicting BOLD functional connectivity using the proposed model with models at either end of the complexity spectrum. The experimental results showed that the correlation structure of BOLD functional resting state brain networks is significantly well captured by our model.

Prediction accuracy of the MKL model for the 23 test subjects is close to 0.70 whereas that of the non-linear model comes second best at 0.52 and that of the SDK model around 0.37. We conducted a series of tests that perturbed the inputs to the model as well as permuted the learned parameters $\mathbf{\Pi}$. The test results attest to the robustness of the proposed model. Interestingly the model not only captures the variability of scales across participants but also demonstrates a possible application in characterizing age-related differences in learning optimal parameters for the accurate estimation of FC (refer to section 4.5). Even in the face of considerable amount of variability present in the data, the proposed MKL model is still able to predict subject-specific FCs with high accuracy. Beyond this, functional connectivity subsumes the influence of different regions across scales and age groups providing a viability of $\mathbf{\Pi}$ being a useful parameter for classification purposes for other domains of application in health and disease. Overall, our method might be considered the missing link in the estimation and improvement of predicting subject-specific resting-state functional connectivity that remained elusive so far for complex non-linear and linear models. Given the strength of the analytical approach and tractability, the proposed model could be a suitable method for predicting task-based functional connectivity across different age groups.

One major limitation of our work is that it is not so straightforward like the linear diffusion model to invert the FC to recover the SC matrix. Currently, in the MKL model the procedure to predict SC from FC would rely on a given $\mathbf{\Pi}$. One way of finding SC is by estimating the diffusion kernels for individual subjects by solving the same system of linear equations used to find FC. Laplacian of a graph could then be estimated. Carefully recovering multiple diffusion kernels might turn out to cause numerical instability to the Laplacian (please refer to section 4.6) and this issue needs to be resolved in the future. While in the current formulation we are empirically determining the number of scales (m) and their spacing, optimization formulation could be modified to estimate these automatically. Moreover, the current model does not consider the non-stationary nature of functional connectivity, the so called functional connectivity dynamics (FCD).

In the next Chapter, we investigate optimization procedures of MKL for modeling the dynamic functional connectivity which is more realistic than modeling stationary FC.

Chapter *5*

Temporal Multiple Kernel Learning

5.1 Temporal dynamics in the BOLD time series

Since its discovery over two decades ago, there has been a keen interest in investigating the slow correlated fluctuations in the functional magnetic resonance images (fMRI) when subjects are at rest and not engaged in any task [16]. Studies capturing the resting-state blood-oxygen level-dependent (BOLD) functional magnetic resonance imaging signals (rs-fMRI) have usually analyzed patterns of functional connectivity that are static within the duration of the scanning. The spontaneous patterns of co-activity across pairs of regions of interest (ROIs) is measured by computing the Pearson correlation coefficient between the rs-fMRI time series of the two regions. The resulting matrix of correlation coefficients is termed the functional connectivity (FC) matrix. The topography of the brain anatomy, called the structural connectivity (SC) is estimated from diffusion tensor images (DTI). How the static SC sculpts the FC has been a challenging open research problem in the brain connectome research domain. Recently it has been recognized that time-averaged grand FCs (gFC) ignore the temporal fluctuations that occur in the rs-fMRI time series within a scanning session. In the last five years the field has moved on to characterizing temporal fluctuations in the functional connectivity within a session, referred to as *dynamic functional connectivity (dFC)* [60, 22, 82]. A straight forward approach for incorporating temporal fluctuations is using windowed FCs (wFCs) estimated by sliding a window over the rs-fMRI time series and calculating the Pearson correlation coefficient as a co-activation measure between pairs of regions of interest (ROIs), thus giving rise to dFC over consecutive temporal windows within a session [54, 35, 105]. This way we obtain a sequence of wFC matrices that in turn can be used to assess the temporal structure of the fluctuations in a session.

This simple approach has several shortcomings, the primary one being the uncertainty as to whether the observed fluctuations in the wFC time sequence are due to noise or due to statistical uncertainty [56]. The other weakness is the lack of models for identifying time-varying brain states and for quantifying transition probabilities between brain states. A related issue is the uncertainty about the alignment of the brain states across the fMRI time series of different participants. Recently hidden Markov model

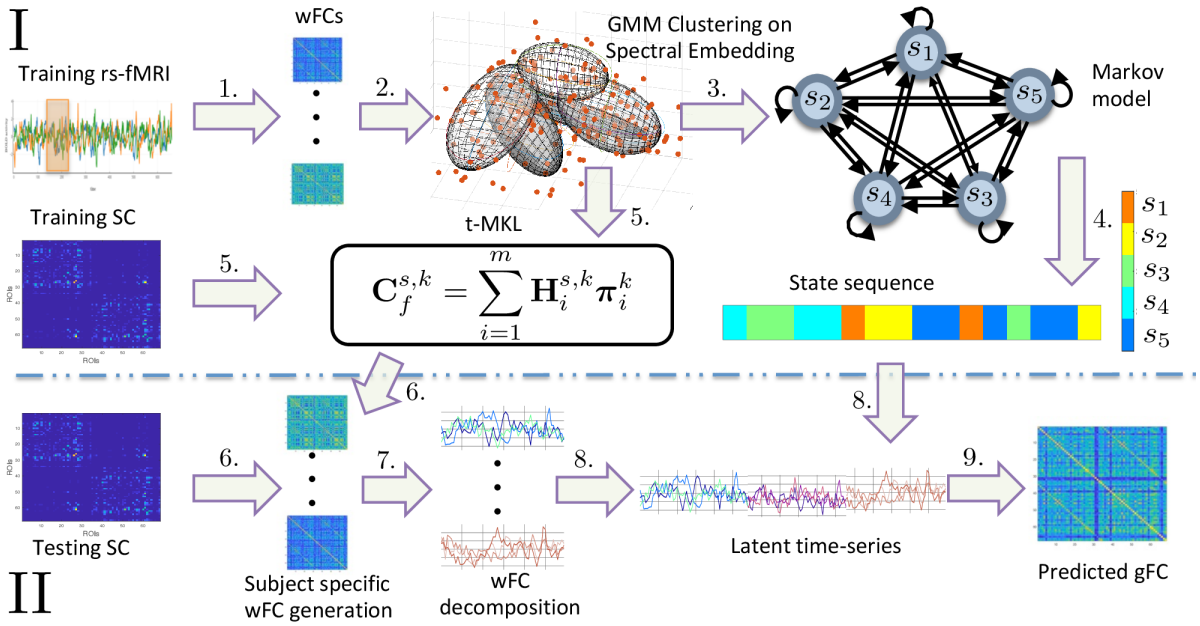

Figure 5.1: **Outline for temporal Multiple Kernel Learning (tMKL) model**. Figure shows the entire pipeline for predicting grand FC for a testing subject. The model incorporates subject specificity along with temporal variation characterization. Part (I) of the model, training phase, consists of three blocks. The first one, learns temporal variations in terms of distinct states via GMM clustering over the underlying manifold of wFCs (steps 1. and 2.). The second block utilizes the empirical transitions between these distinct states and captures dynamics in the first order Markov chain (steps 3. and 4.). The third block learns subject-specificity by modeling each state by its MKL model [98] (step 5.). Part (II) of the model validates its generalizability on unseen subjects. Importantly, only SC of a testing subject is required (step 6.). Each state for the testing subject is characterized in step 7.. Each state-specific predicted FC is decomposed into a latent time series which are then concatenated using the steady state distribution of the Markov chain (steps 4. and 8.). Finally, grand average FC is predicted for that subject (step 9.).

(HMM) based schemes have been proposed to characterize the dynamic connectivity patterns among a small number of resting state networks (RSNs) [88].

They use selected few ROIs and modeled clusters of individual fMRI time-points as the transient brain states while considering the covariance matrix of each cluster as the corresponding transient network dFC. Thus, their state representation is not subject-specific and hence the learned HMM model can not be used for subject-specific characterization.

Linear models based on graph diffusion of brain dynamics have been proposed recently wherein neuronal firing rates are hypothesized to perform random walks on the SC graph to give rise to FC [3]. The linear diffusion models consider that the mean regional activity diffuses over the anatomical fibers governed by a system of coupled 'deterministic' differential equations whose solution becomes the graph diffusion kernel which is hypothesized to resemble the FC. However these models consider static FCs and consequently temporal fluctuations in the FC are not directly modeled.

To address these issues, we propose a novel solution for characterizing the dynamic evolution of functional connectivity patterns over time. This is achieved by proposing two novel constructs: 1) *t-MKL* model that learns the static SC to dynamic FC mapping for generating transient state wFC for each of the states; 2) first-order Markov model that learns the state transition probabilities. The proposed solution obtains gFC from SC by predicting multiple wFCs along with capturing their temporal evolution. This is achieved by characterizing the transitions between transient states using a first-order Markov model. This model is used for generating a long state sequence using the steady state distribution of Markov random walk. This state sequence is further replaced by sequence of corresponding wFCs generated by the t-MKL model. Finally, these wFCs are factorized to recover a latent time-series sequence. gFC is then computed on the reconstructed time series and compared with the empirical FC. The proposed model recovers the gFCs that are very close to empirical FCs as the wFCs recovered with the t-MKL model enable realization of subject-specific functional dynamics. Further, various perturbation experiments demonstrate the robustness and validity of the proposed scheme. The specific contributions of the work are the following:

- Novel approach for learning the SC-FC mapping through characterizing the dynamic functional connectivity (dFC) over time windows.
- Proposal of a novel multiple diffusion kernel model that learns to predict wFCs from SC (t-MKL model).
- Characterizing the transition of transient brain states in the rs-fMRI time series using first-order Markov model.
- Estimating the latent fMRI time series by using the Markov transition probability matrix in conjunction with the t-MKL model.

5.2 Proposed Model

In this section we describe in detail the whole pipeline of the proposed parametric-model to map the relation between SC and FC for a cohort at rest. The proposed model considers the importance of underlying anatomical constraints to generate the temporal richness as well as to characterize and assess whole-brain FC dynamics. Figure 5.1 shows a flowchart of the essential elements of the whole pipeline. Proposed model partitions aspects of the whole-brain dynamics succinctly into two parts: characterizing temporal dynamics through identification of latent transient states and linking them to the underlying structural geometry. These two aspects are parameterized using a novel combination of unique methods. The model utilizes wFCs for identifying states and SC-wFC pairs for learning dependence from the structure. Once these two parts successfully characterize the above mentioned aspects by tuning respective parameters, the model is tested for its generalizability on unseen subjects.

For identifying latent states within the dynamics, we discover the underlying globally-nonlinear-manifold over which all the wFCs lie, thus recovering the lower-dimensional space for a meaningful characterization. We employ a probabilistic framework for estimating the number of states and shape of each state in the lower-dimensional space, ensuring soft assignments of wFCs to its neighboring states. These soft assignments are further used to estimate the transition dynamics between these states. With respect to second aspect of the model, we adapt the multiple kernel learning (MKL) framework [98] for parameterizing the dependence of SC on wFCs for each state. We observe that the parameters to be learned form a non-convex combination, necessitating an iterative algorithm. Thus we formulate the learning objective into an optimization formulation and adapt an iterative algorithm for solving this non-convex combinations of these parameters.

The model predicts state-specific FCs for an unseen subject. These sFCs are decomposed into a latent time-series which further is concatenated using the relative frequency of occurrence of states to generate a global time-series for calculating the static FC of a subject. Thus, for a new subject, given the SC, static FC along with its state-specific FCs are predicted by the proposed model. In the subsequent subsections we elaborately describe each part of the proposed model. From now on, let $D = \{\mathbf{F}_w^1, \cdots, \mathbf{F}_w^s, \cdots, \mathbf{F}_w^p\}$ be the set of all wFC matrices obtained by sliding a window of fixed size ω over the n-dimensional fMRI time-series belonging to all the training subjects.

5.2.1 Spectral Embedding

We propose to soft-cluster these wFC matrices into K states, first by vectorizing the lower triangular part to a size of $\frac{n(n-1)}{2} \times 1$. These wFCs are sparsely spaced in this higher-dimensional space, but may originally lie on an intrinsic space that may be a globally non-linear manifold [13]. Spectral embedding method is employed to reduce the dimensionality of the data, by finding a mapping to a lower dimensional manifold over which these wFCs reside [14]. The graph constructed over the data points provides discrete approximation of this continuous manifold. The solution embedding is provided from the eigenmaps (eigenvectors) of the Laplacian operator over the graph, which approximates a natural mapping onto the entire manifold. The Laplacian eigenmaps preserve the local structure in the graph, thus keeping the solution embedding robust to outliers and noise.

The spectral embedding method is applied as follows. Firstly, an affinity matrix is created by applying a radial basis function over the L1 distance between every pair of wFCs. This matrix captures pairwise relationship between wFCs in a relational graph. Next, we form the corresponding normalized graph Laplacian matrix and use the eigenvectors corresponding to its lowest K eigenvalues to define the basis vectors embedding space [108, 79, 92]. The value of these eigenvectors against each wFC represent its resulting transformation into the embedding space. Finally these K-dimensional embedded wFCs are clustered using GMM, as explained in the next subsection.

5.2.2 GMM Clustering

Following the discovery of an approximation to the continuous lower-dimensional manifold, we now parameterize the local density distribution of wFCs over the manifold into a probabilistic framework, Gaussian mixture model (GMM) [15]. Gaussian mixture model is a factor analysis model that represents the probability density of a sample as a weighted combination of component Gaussians. Such a representation facilitates them to represent a large class of sample distributions. Specifically, distribution of wFCs over the manifold are modeled as a GMM.

Let the density of $\mathbf{F}_w^s$ be a linear combination of K component Gaussian densities, represented as follows:

$$\begin{aligned} p(\mathbf{F}_w^s; \mathbf{\Theta}) &= \sum_{k=1}^{K} \Psi^k(s) \mathcal{N}(\mathbf{F}_w^s; \mu^k, \mathbf{\Sigma}^k) \\ \sum_{k=1}^{K} \Psi^k(s) &= 1, \forall s = 1, \cdots, S \end{aligned} \tag{5.1}$$

where p denotes the probability density of a wFC. Each component Gaussian is a K-variate Gaussian probability density function of the form:

$$\mathcal{N}(\mathbf{F}_w^s; \mu^k, \mathbf{\Sigma}^k) = \frac{1}{(2\pi)^{K/2} \det(\mathbf{\Sigma}^k)^{1/2}} \exp\left\{ (\mathbf{F}_w^s - \mu^k)^\top \mathbf{\Sigma}^{k^{-1}} (\mathbf{F}_w^s - \mu^k) \right\}.$$

GMM thus represents the manifold as a set of Gaussian densities and parameterizes it in terms of $\mathbf{\Theta}$:

$$\mathbf{\Theta} = \left\{ \Psi^k(\cdot), \mu^k, \mathbf{\Sigma}^k \right\}, k = 1, \cdots, K. \tag{5.2}$$

As the collection of these component Gaussians forms the manifold, the component Gaussians can be interpreted as a *latent transient state* visited by the brain. Each state is a Gaussian but at different locations and shapes governed by μ^k and $\mathbf{\Sigma}^k$ respectively in the manifold.

5.2.3 State Transition Markov Model

The wFCs now being quantized into these finite states $S = \{s_1, \cdots s_K\}$ by GMM clustering, transitions between these states is representative of the dynamics in time series. We assume first-order dependence amongst these transitions and learn the Markov transition probability matrix, $\mathbf{T}_{K \times K}$. Figure 5.2 shows a depiction of Markov model for $K = 5$ and corresponding transition probability matrix. Each edge $t_{i,j}$ captures the probability of transition from state i to state j. Similarly, self-loop edges $t_{i,i}$ depict the probability of remaining in the same state. For each state i we compute $t_{i,j}$ by counting the number of first-order transitions to state j in the state sequence. Finally, we normalize each row of $\mathbf{T}$ to make it a transition probability matrix. This Markov matrix learned on training wFCs is used to generate a random state sequence. As any Markov chain converges to its steady state distribution regardless of its initial distribution with time, we find the steady state distribution over transition matrix and use this distribution as frequency of occurrence of states over the time course. This gives us a state transition sequence.

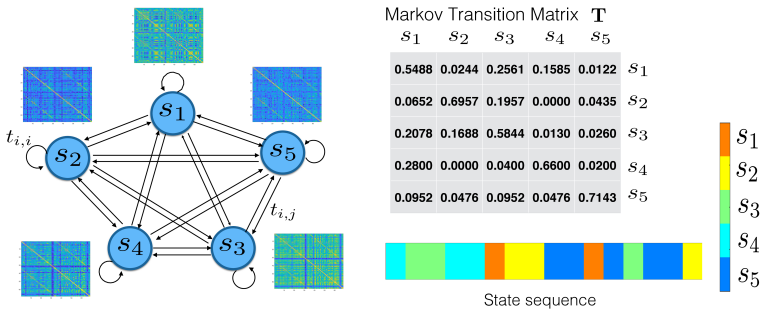

Figure 5.2: **Graphical depiction of proposed Markov state transition model**. An illustration of the first-order Markov chain used as a part of the proposed tMKL model. Each state has its unique distribution of FCs, represented as a Gaussian in the embedding space, from which subject-specific FCs can be sampled. The corresponding transition matrix (for K=5) and an example state sequence generated with a Markov random walk over the transition matrix is also depicted.

Subsequently, we obtain the wFC matrix for each of the states using the input SC matrix of the testing subject and the learned t-MKL model. This is achieved by first defining diffusion kernels over the SC matrix of a testing subject and then multiplying them with $\mathbf{\Pi}^k$s learned for each state using t-MKL model. This would yield state-specific wFCs for that subject. In summary, based on a realization of the Markov chain, a sequence of wFCs is generated.

5.2.4 tMKL Model

Mean regional activities of all regions are assumed to be in a random walk over the SC graph. This phenomenon is represented by a linear differential equation whose analytical solution is the diffusion kernel over the graph defined by SC which is hypothesized to be representing FC [3]. [97] discover that physical diffusion over such large scale graphs exhibits multi-scale relationships with FC, thus a linear combination of multiple diffusion kernels is considered more representative of FC (this model is referred to as MKL_NIPS from now on). The linear combination coefficients are scalar values which equally weigh all regional activities at each diffusion-scale. But it may so happen that activities of non-physically connected regions may be modulated by other regions. To represent this phenomenon we introduce the variables $\boldsymbol{\pi}_i$s of size $n \times n$, that capture the inter-regional co-activation patterns at diffusion-scale i, $\forall i = 1, \cdots, m$, m being the number of diffusion-scales.

Let a diffusion kernel defined at scale i be denoted by $\mathbf{H}_i$.

$$\mathbf{H}_i = e^{-\tau_i \mathbf{L}} \tag{5.3}$$

Here τ_i is the spatio-temporal scale of heat diffusion and $\mathbf{L}$ is the Laplacian matrix corresponding of the SC. We propose that a wFC matrix can be decomposed into a set of diffusion kernels multiplied with

their co-activation pattern:

$$\mathbf{C}_f = \sum_{i=1}^{m} \mathbf{H}_i \boldsymbol{\pi}_i, \tag{5.4}$$

$\mathbf{C}_f$ denoting the predicted wFC. We hypothesize that co-activation patterns of a state will be distinct than those of other states and hence we add a superscript index k to get $\boldsymbol{\pi}_i^k$. As the parameter $\boldsymbol{\pi}_i^k$s are state dependent, the state specific predicted functional connectivity, $\mathbf{C}_f^{s,k}$, will be as following:

$$\mathbf{C}_f^{s,k} = \sum_{i=1}^{m} \mathbf{H}_i^{s,k} \boldsymbol{\pi}_i^k = \sum_{i=1}^{m} e^{-\tau_i^k \mathbf{L}^s} \boldsymbol{\pi}_i^k \tag{5.5}$$

Here $\mathbf{L}^s$ is the Laplacian matrix of the SC corresponding to wFC^s. This results in the following optimization problem for $\boldsymbol{\Pi}^k$ and $\boldsymbol{\tau}^k$:

$$\begin{aligned} \underset{\boldsymbol{\Pi}^k, \boldsymbol{\tau}^k}{\text{minimize}} \quad & \sum_{s=1}^{p} \left\| \Psi^k(s) \left(\mathbf{F}_w^s - \mathbf{C}_f^{s,k} \right) \right\|_F^2 + \sum_{i=1}^{m} \|\boldsymbol{\pi}_i^k\|_1 + \sum_{i=1}^{m} \|\boldsymbol{\pi}_i^k\|_2 \\ \text{subject to} \quad & \mathbf{C}_f^{s,k} = \sum_{i=1}^{m} e^{-\tau_i^k \mathbf{L}^s} \boldsymbol{\pi}_i^k \\ & \boldsymbol{\pi}_i^k \in \mathcal{S}_+^n, i = 1, \cdots, m \\ & \boldsymbol{\tau}^k \succeq \mathbf{0}. \end{aligned} \tag{5.6}$$

Here $\mathcal{S}_+^n$ is the convex set of positive semi-definite matrices. The objective function takes the form well known in regression analysis as *least absolute shrinkage and selection operator* (LASSO) that performs both variable selection and regularization. We arrived at the model parameters experimentally, for example, the number of scales m is empirically chosen (see Subsection 5.3.1).

5.2.5 Factorization of predicted wFCs for time series generation

Pearson correlation between two time-series A, B is $\rho(A, B) = \frac{cov(A,B)}{\sigma_A \sigma_B}$. Hence for a zero-mean and unit variance time-series $Z_{n \times \omega}$, wFC matrix is the covariance of times-series. we factorize the wFC as follows:

$$\begin{aligned} \mathbf{F}_w &= \mathbf{U} \boldsymbol{\Lambda} \mathbf{U}^\top \\ &= (\sqrt{\boldsymbol{\Lambda}} \mathbf{U}^\top)^\top (\sqrt{\boldsymbol{\Lambda}} \mathbf{U}^\top) \\ \hat{Z} &= \sqrt{\boldsymbol{\Lambda}} \mathbf{U}^\top. \end{aligned} \tag{5.7}$$

Thus, using Eq. 5.7, we recover latent time-series matrix $\hat{Z}$ that can be taken as approximated time-series used for obtaining wFC. For a subject, each cluster-specific wFC is decomposed into latent time-series and these are concatenated into a grand time-series. The latent time series are concatenated by considering the steady state distribution of the Markov chain. Steady state distribution is the probability of being in a state which remains the same throughout transitions. Every random walk over the transition matrix approximates this distribution after infinitely long time. Finally, as Pearson correlation is order agnostic, calculating Pearson correlation matrix of the grand time-series generates the predicted gFC for that input testing subject.

5.3 Experiments & Results

5.3.1 Parameter Selection

- **Performance Evaluation:** Performance of the proposed solution was evaluated in the following setup. We use Pearson correlation coefficient between empirical and predicted FCs to keep the measure of model performance consistent with the extant literature[3, 10]. Half of the cohort, 23 subjects, were randomly selected for training, and the remaining half were included in the testing set.

- **Choice of ω:** Within extant literature, the choice of a suitable sliding window size is an open problem with respect to the analysis of temporal dynamics in rs-fMRI [82]. The sliding window size should be small enough so as not to miss the state transitions and should be large enough to capture the state transitions reliably. Keeping this in mind, we followed [4] by using a sliding window of $\omega = 22$ TRs. The window was tapered at the ends by convolving it with a Gaussian of $\sigma = 3$ TRs and was slid with a stride of 5 TRs to create wFCs.

- **Choice of GMM parameters:** Each *latent transient state* in which these wFCs lie is represented using a component Gaussian of the GMM. In order to choose the optimal number of these states, K, we selected the GMM model corresponding to minimum BIC score. Bayesian information criterion (BIC) is a statistical measure based on the log-likelihood function used for selecting a model amongst a finite set, where the model corresponding to the lowest BIC score is chosen. The plot in Figure 5.3 shows BIC scores for the models obtained by fitting GMM for a large range of K, where the minimum value was reported for $K = 12$. To retain generality of the component Gaussians, we ran our experiments by considering a unique full covariance matrix for each component Gaussian.

- **Choice of m:** The scale values were sorted in ascending order, where lower values correspond to local diffusion phenomenon and higher values correspond to global diffusion phenomenon. Scale values lying in-between correspond to intermediate diffusion phenomena. In order to be consistent with that of MKL model, we chose the number of scales as $m = 16$.

5.3.2 Grand average FC (gFC) prediction

We compare the performance of the proposed model with several existing approaches: Abdelnour et al. [3] (SDK), the non-linear dynamic-mean-field (DMF) model of [36] and Multiple Kernel Learning model of [98]. To our knowledge, ours is the only model that incorporates structural information along with temporal dynamics for predicting grand average FC, hence we are comparing with these models. DMF and SDK models do not incorporate learning in their formulation and tune the parameters for each subject separately. DMF model inherently captures non-stationarity, therefore it is directly used for gFC prediction without computing wFCs. We estimated the optimal parameters of the DMF and SDK

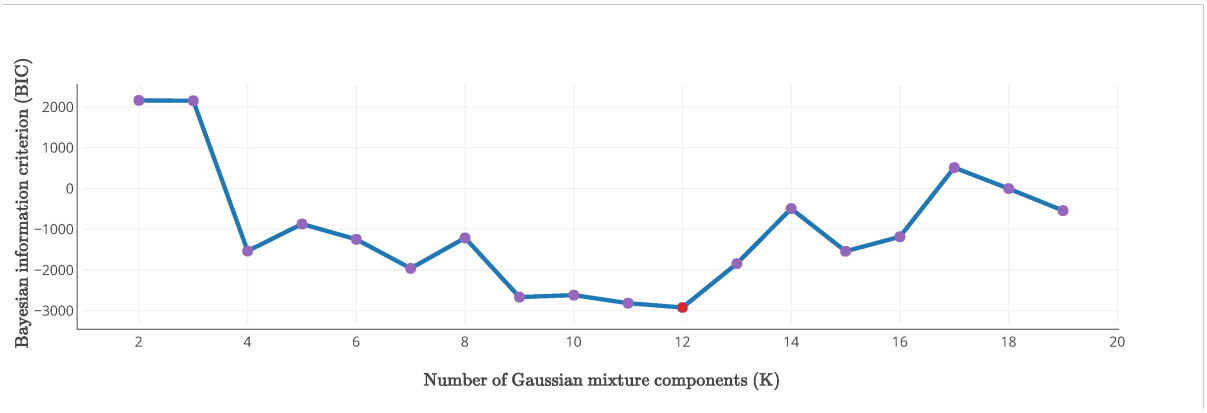

Figure 5.3: **Bayesian information criterion (BIC) score for selecting the number of components in Gaussian mixture model**. The GMM is fit over the training wFCs lying in the lower dimensional manifold. The BIC score is reported by varying the number of component Gaussians (K) from 2 till 19. The Gaussian mixture model corresponding to $K = 12$ (shown in red) has the lowest BIC score among others and is therefore preferred. The plot shows local minima at $K = 4, 7$, and 15 which may mislead the user while selecting the optimum model. This local minima suggests the choice of number of components in Allen et al. [4].

models from the training wFCs and predicted the gFCs of testing subjects based on this subject-specific parameter. The mode of the performance distribution histogram for the training set was used to select the optimal model parameters. Figure 5.4 shows that tMKL has superior performance compared to others.

5.3.3 Robustness of the model

In order to validate the robustness of our model we performed various experiments to assess whether our solution overfits the training data and also whether the prediction of the grand average FC is agnostic to the particular SC matrix.

- **Reproducibility of states** As mentioned in Section 5.2.2, the GMM yields K soft assignment vectors for the training wFCs. We validated reproducibility of this clustering by ensuring replication of the same for testing subjects' wFCs. We generated wFCs for all the testing subjects using the sliding window approach. Soft assignment vectors were generated for these testing wFCs using the GMM employed on the training data, which is then used to compute the Markov transition matrix and the corresponding steady state distribution. Figure 5.5 shows an example of the steady state distribution for our proposed method . We evaluated the similarity between the Markov transition matrix and steady state distributions of the training and testing wFCs by finding the Pearson correlation coefficients. Table 5.1 shows that the states are highly replicable for multiple training-testing splits of the data.

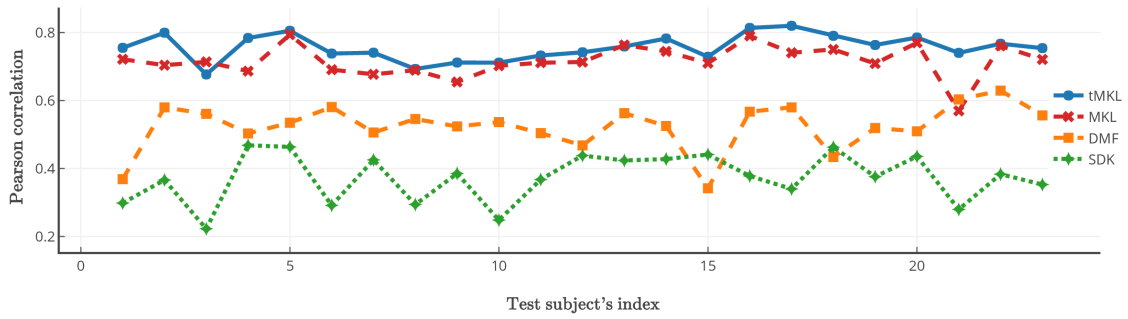

Figure 5.4: **Model performance comparison between tMKL and existing models**. Pearson correlation between the empirical and predicted gFCs for all the testing subjects is shown for all models. As can be seen, MKL model outperforms other two models, and tMKL model is at par or better than MKL for all but one testing subjects. Even though there is marginal gain in the overall prediction quality, tMKL provides rich insights into the temporal dynamics thus gaining its superiority over extant models.

- **Cross-validation experiments** We performed k-fold cross-validation experiment whose results are listed in Table 5.2. These results suggest that performance of our solution is consistent across various splits, hence supporting our claim of generalizability of our model on unseen data.

- **Perturbation experiments** Each testing subject SC was perturbed $N = 150$ times and using the learned model we predict the grand average FC. We perturbed every SC by randomly generating it from the power law distribution followed by its elements. The generated state-specific wFCs may have non-positive eigenvalues. Here we considered only the real part of the generated time series in order to estimate (predict) grand average FC. Figure 5.6 shows this observation over all the 23 testing subjects. Box plots for each subject depict the range of correlation values for random SCs. Here we observe less correlations between empirical and predicted gFCs using the perturbed SC, validating that our model respects the topology of input SC. This suggests that the model is not overfitting the data and is sensitive to perturbation in SC.

5.3.4 Analysis of states

Empirically, fluctuations in the wFC sequence are shown to give rise to distinct transient wFC states that are reproducible in random re-sampling of subjects [4]. Our model also achieves reproducibility of these states for random splits of training subjects (See Table. 5.1). As wFCs lying on the lower-dimensional manifold are clustered using GMM, a wFC belongs to all states (component Gaussians) with different probabilities, $\Psi^k(\cdot)$. A wFC is assigned to a state which it belongs to with the maximum probability of belongingness. Further, two wFCs assigned to the same state should have a higher correlation with each other in contrast to a lower correlation value when assigned to distinct states. Our

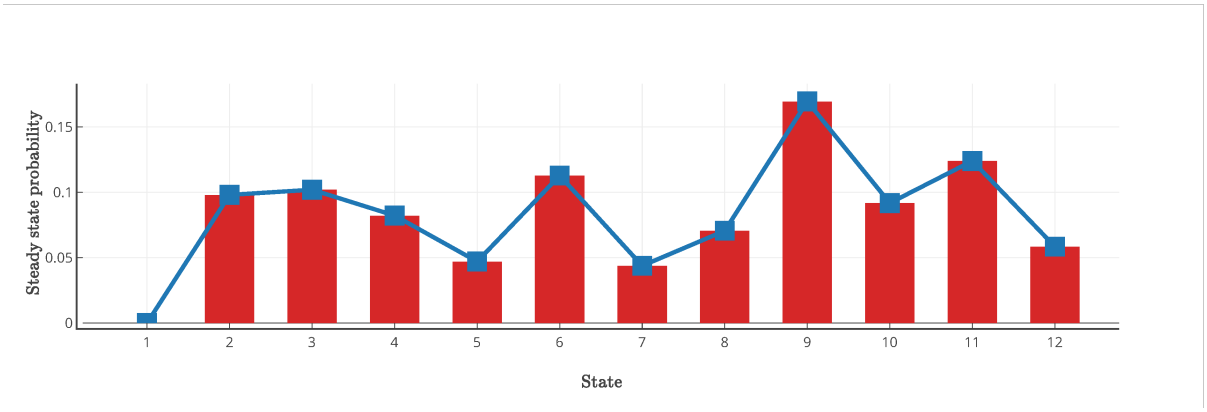

Figure 5.5: **Markov chain steady state distribution**. After the states are retrieved using GMM, the Markov chain transition matrix was learnt over the resulting state-sequences of the training subjects' wFCs. The figure shows the steady state distribution of the transition matrix, which represents the probability distribution of occurrence of a state after infinite amount of time.

Run Index	ρ_{TM}	ρ_{TM}	e_{TM}	e_{SSD}
1	0.9947	0.9509	0.1337	0.0564
2	0.8683	0.8546	0.7379	0.2703
3	0.9440	0.8839	0.5120	0.1433
4	0.9035	0.9809	0.7154	0.1004
5	0.8624	0.9604	0.7094	0.1332
6	0.9665	0.8337	0.3824	0.1119
7	0.9131	0.8563	0.6263	0.1107
8	0.9746	0.6824	0.3381	0.1521
9	0.9275	0.8691	0.6671	0.0950
10	0.8623	0.9599	0.7299	0.1608
11	0.9777	0.9596	0.3250	0.0482
mean	0.9301	0.8692	0.5068	0.1358
stdev	0.0501	0.1155	0.2093	0.0636

Table 5.1: **Comparison of Markov chain transition matrix (TM) and its steady state distribution (SSD) between training and testing subjects.** Comparison is done computing the Pearson correlation coefficient (ρ) and the L2 distance (e) between the training-TM, testing-TM and training-SSD, testing-SSD respectively. This experiment is repeated for 11 training-testing splits of the data. Consistent high values of ρ and low values of e across multiple splits show similarity of the states and their transition behavior across training-testing subjects, therefore establishing reproducibility of states.

k	fold-1	fold-2	fold-3	fold-4	fold-5	mean
2	0.757	0.732	-	-	-	0.745
3	0.771	0.811	0.778	-	-	0.787
5	0.785	0.809	0.813	0.809	0.808	0.805

Table 5.2: **Cross-validation experiments suggesting generalizability of tMKL model**. Mean k-fold cross-validation results for $k = 2, 3, 5$ are shown in the corresponding rows for k-values. As the number of training samples increases with the number of folds, the mean performance also increases suggesting that the model is learning well with increased samples ans is able to replicate the same for testing subjects.

model should inherit this distinctness of states which should further be reflected on testing subjects. This property of the model is validated in the following ways.

During the training phase of the pipeline, the tMKL framework parameterizes the dependence of these clustered wFCs on the SC for each state, as captured in $\boldsymbol{\pi}^k$s. In other words, the learnt state-specific $\boldsymbol{\pi}^k$s are expected to be distinct from each other. This property is shown in Figure 5.7. Following, in the testing phase of the pipeline, the framework is used to predict the state-specific FCs given the SC of a training subject. Also, the predicted state-specific FCs should be distinct from each other as well as should belong to their respective component Gaussians with a greater probability in comparison to other components. These properties are quantitatively justified via accuracy experiments in Figure 5.8. Overall accuracy of this state-belongingness for the testing subjects is 82.25%. Figure 5.9 qualitatively shows the communities identified in the mean state-specific FC predictions across all test subjects. Clearly, regions in each state show distinct interaction patterns among themselves whose temporal alignment, along with these communities, is recovered by our model, thus playing a major role in the model's superior performance than other models.

5.4 Discussion

Besides understanding the relationship between the anatomical architecture and the functional dependencies, over the last decade, characterization of the temporal richness also has been the major trend in the field of cognitive neuroscience. Several approaches have been proposed to understand this inherent richness observed in the intrinsic activity. Operator-based formulations of neural dynamics [86, 36] propose a generative model to predict functional connectivity from structural connectivity via incorporating temporal dynamics into the model. Another class of techniques introducing spectral graph theoretic methods [3, 1] focus on mapping the eigen-spectrum of SC and FC of individual subjects, but with minimal focus on the temporal richness. This class of models needs further investigation for a better prediction. Allen et al. [4] and subsequent works have focused only on the temporal structure of the windowed FCs and were able to characterize state transitions well, but without relation to the underlying structure.

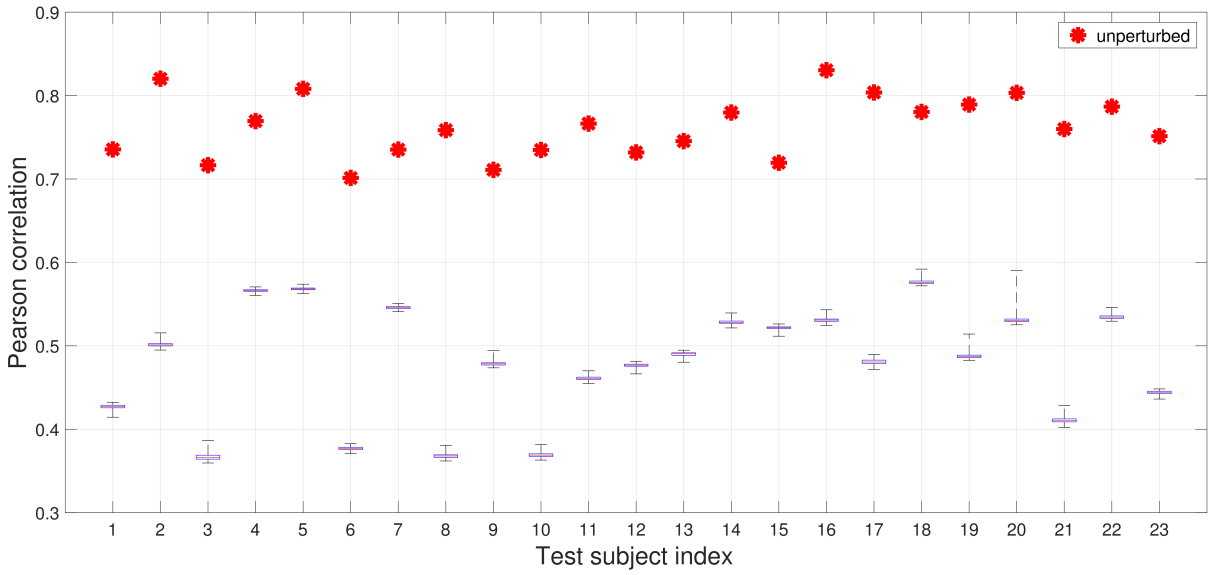

Figure 5.6: **Effect on performance of tMKL model due to perturbation of SC matrices of test subjects**. Shown here are the box plots (blue) of Pearson correlation between empirical and predicted grand FCs when SCs are perturbed for all the testing subjects. Red dots at the top of each box plot indicates the actual subject-wise model performance, i.e. with unperturbed SCs. SCs were perturbed with the procedure mentioned in the Subsubsection 4.4.4.1. This suggests that proposed solution does not overfit the data and is sensitive to perturbation in SC.

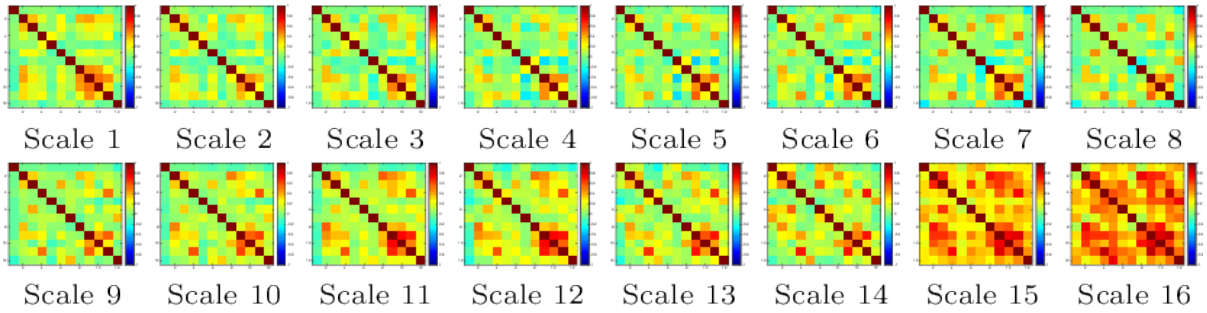

Figure 5.7: **Distinctness of $\boldsymbol{\pi}_i^k$s**. After state-specific MKL models are learnt, we check the distinctness of $\boldsymbol{\pi}_i^k$s for every scale value ranging from $i = 1$ to m using Pearson correlation coefficient between every pair of states. In general the off-diagonal entries in these pairwise correlation matrices are mostly zero, indicating the distinctness $\boldsymbol{\pi}_i^k$s. As observed, $\boldsymbol{\pi}_i^k$s are significantly distinct for global scales (lower values of i) in comparison to local scales (higher values of i), where they are similar.

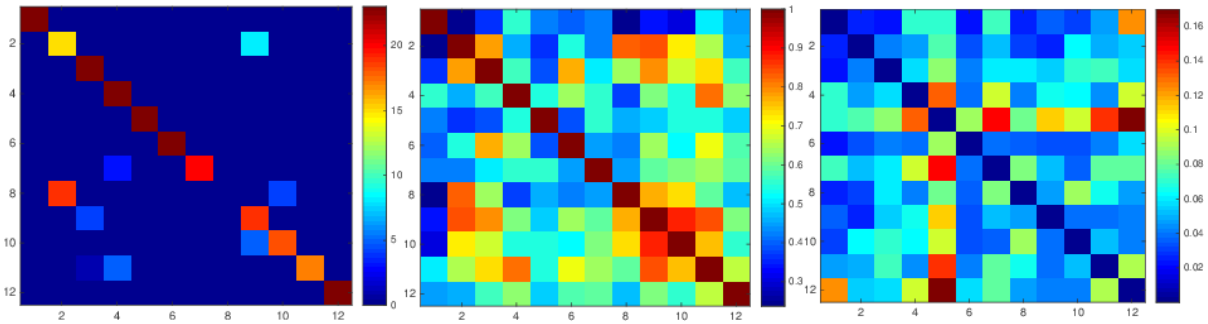

(a) Confusion matrix (b) Mean (c) Standard deviation

Figure 5.8: **Quantitative state specificity of the model**. This simulation experiment measures the accuracy of state-specific predictions. For each testing subject there are K number of state-specific FCs. The state label against which a state-specific FC is predicted from tMKL model serves as the ground truth for this experiment. Empirically, each state-specific FC must be nearer to the training wFCs belonging to that state than from the training wFCs belonging to other states, thus attesting the accuracy of model prediction. For this purpose, we searched for 21 nearest neighbors for each state-specific FC and voted for the empirical state-belongingness sequence, serving as the prediction only for this simulation experiment. (a) shows the confusion matrix to measure the accuracy of the prediction of each state. Rows (columns) depict the actual (predicted) states. Overall accuracy of tMKL model prediction is 82.25%. It can be seen that non-zero off-diagonal entries result in reduced accuracy. To get a subject-specific measure of the state-specificity, we ran the same experiment for all the testing subjects independently. Pearson correlation between all the possible pairs of the K state-specific FCs for a subject was calculated and stored in a $K \times K$ matrix. Element-wise mean and standard deviation across all the subject-specific matrices is shown in (b) and (c) respectively. Noticeably, mean matrix is similar to the confusion matrix with very less standard deviation.

Allen et al. collect all the wFCs from the training subjects and fit a k-means clustering model to discover distinct latent states visited by the brain that are common to the cohort. In our preliminary attempts to replication of results and to link the structural constraints with the temporal structure discovered by Allen et al., we trained MKL model for each of the states identified with k-means clustering technique over the wFCs. Even though the overall grand average FC was predicted with high Pearson correlation values, the reproducibility of states in the predicted state-specific FCs is not accurate (see Figure 5.10).

One of the apparent problems might be confrontation with the curse of dimensionality for applying any of the unsupervised techniques. A wFC during clustering ought to be assigned to the same state as that of its neighbors. wFCs lie in a high dimensional space, but based on their similarity with respect to their neighbors, they may lie on an intrinsic lower-dimensional manifold. This lower dimensional manifold becomes the space over which temporal structure can be precisely identified. Spectral embedding techniques utilize this similarity between the neighboring wFCs to discover the underlying manifold. After representing the temporal structure as a manifold, the next task was to parameterize this lower-dimensional structure. K-means clustering would yield spherical clusters, limiting the shape and size of states, whereas GMM clustering is a generalized clustering scheme. We parameterized the local

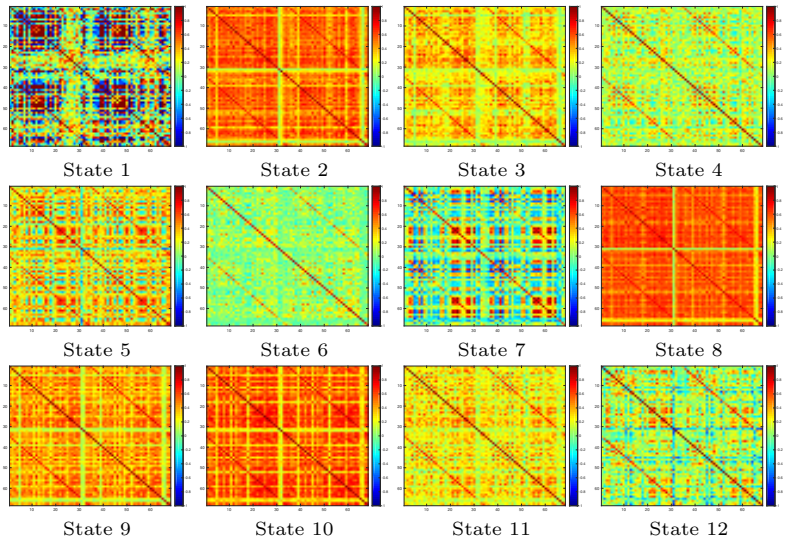

(a) State-specific FCs

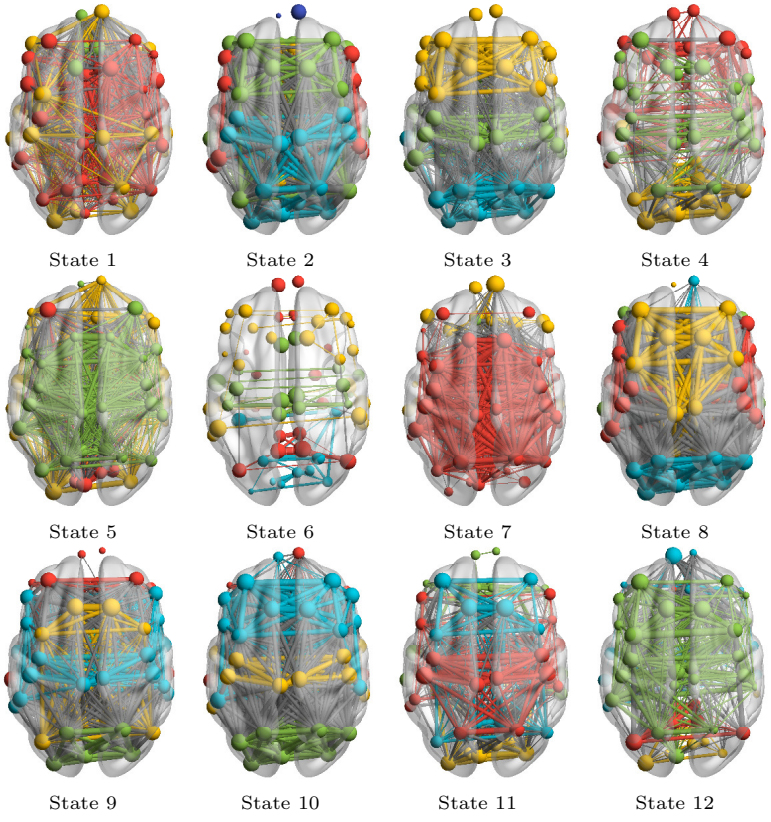

(b) Visualization of states

Figure 5.9: **Qualitative state specificity** State specific FCs predicted for every subject are averaged across all testing subjects. (a) Visually distinct FC matrices are shown for all the 12 states. (b) Communities are identified for these mean FCs using Louvian algorithm available in brain-connectivity-toolbox [87] and Brain-net-viewer [113] was used for visualization of these communities. The distinct community structures clearly suggest that transient states are modeling different brain dynamics.

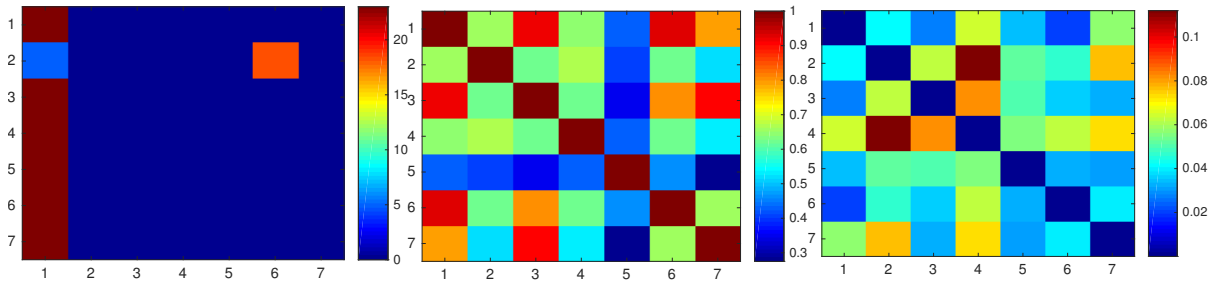

(a) Confusion matrix **(b)** Mean **(c)** Standard deviation

Figure 5.10: **State specificity of k-means**. This figure illustrates similar experiments as shown in Figure 5.8 to demonstrate state specificity of the model when using k-means to cluster the state-specific FCs for the testing subjects in their *original space* as one in Allen et al. [4]. With respect to k-means clustering of training wFCs, K was chosen to be 7 according to the elbow criterion which is computed as the ratio between within-cluster distance to between-cluster distance. The ground truth state label for each state-specific FC remains the same as mentioned before. For the K such FCs for every testing subject, each state-specific FC is assigned its state label according to the nearest cluster centroid. The confusion matrix in (a) clearly evidences the poor reproducibility of the clustering in testing data, where almost all of the state-specific FCs are misclassified to belong to state 1. Overall accuracy of the prediction is 14.23%. (b) and (c) show the element-wise mean and standard deviation matrices of the Pearson correlation between all pairs of the state-specific FCs across all testing subjects. Evidently, the mean matrix has more high-valued off diagonal entries in comparison to the mean matrix in our method, suggesting lack of distinctness of states when using k-means on this dataset.

density-distribution of wFCs over the manifold into a factor analysis model that further represents the manifold as a set of component Gaussians at various locations whose shape, orientation, and size depend on the local densities of the wFCs.

The proposed model is cohort based and hence the underlying assumption is of the generalizability of the model to unseen subjects. We have learned the Markov transition probability matrix on training wFCs and used this to generate long sequences of time series of testing subjects. Concatenation of the latent time-series of the predicted state-specific FCs results into the grand average FC well. This implies that the transitions are generalizable over the cohort and are not restricted only to the subjects used for learning. Thus, the temporal dynamics of fMRI time series are well represented by the learned Markov model. One of the future directions would be to investigate the relation between the latent time-series and the actual BOLD time-series. State-specific FCs were eigen-decomposed, hence one possibility is that the latent time-series might correspond to the connectome harmonics.

We have characterized the SC-FC mapping by gaining understanding of the temporal dynamics. We learn the distinct states of dynamics, and their transitions. The proposed model first learns the intermediate relationship between SC and wFCs and use this relation to predict grand average FC. In order to verify whether the state-specific FCs predicted for a subject are distinct, hence showing its efficacy in learning meaningful states, we performed community detection over these matrices. Figure 5.9 shows the communities identified in distinct states by taking average over all the testing subjects. Clearly,

regions in each state show distinct interaction patterns among themselves whose temporal alignment, along with these communities, is recovered by our model, thus playing a major role in the model's superior performance than other models. Importantly, the model was learned only over the individual states without any global error measure. Still the grand average FC prediction is at par or better than that of the MKL model. This seems to be possible only because of characterizing the latent temporal structure. As part of the future work, it will be interesting to explore the bio-physical meaning of the model parameters and better characterize the dynamics and hence predicting the time series themselves.

Chapter *6*

Conclusions and Future Work

Since spontaneous brain activity has been observed in 1980's, its purpose has been questioned and yet not fully understood. Investigations using task based paradigms had assumed that this metabolic activity is sufficiently random for it to be averaged out. But many studies have observed spatial patterns in spontaneous activity coherent with their respective task conditions [80, 93]. Such observations initiated the study on characterizing this spontaneous activity through its metabolic markers such as BOLD activity. These studies were converging at observing spatially distributed patterns of activity, known as resting state networks (RSNs), primarily default mode network (DMN) [16, 83]. A common understanding of the importance of intrinsic activity was emerging, that the spontaneous activity was not random but highly structured. This led to investigating this activity through computational models as these provide an access to the bio-physics.

Initial attempts on understanding this activity via relating it to the underlying anatomy promised some results but not fully conclusive, thus leading to representing the dynamics over the structure a possible way for a better appreciation of the cognitive role of the intrinsic activity [33]. Another line of investigation looked at network theoretic perspective of the RSNs [96]. This chain of thought summarized RSNs in terms of networks properties such as node-degree, modularity, centrality etc. The notion of structural core [51, 50], moved the field in understanding the importance of ROIs in allowing dynamics to flow through them thereby becoming central to pathways of inter-regional communications.

Bio-physical computational models and network theoretic models provide different perspectives of the functioning of the brain at rest. While the former variety of models incorporate details of the underlying bio-physics, the latter framework abstracts out all those details and takes a general network perspective to brain function. Consequently there is a need to find a fundamental basis linking both of these viewpoints. Atasoy et al. [6] points towards the link between the two via eigenmodes: eigenmodes of the connectome play a major role in shaping the intrinsic temporal dynamics and RSNs show unique correspondences to these graph-eigenmodes. Thus the graph-eigenmodes or the harmonics of the connectome seem to bridge the gap between biological detail and abstraction. Concretely, the emerging field of graph signal processing (GSP) [94] can be used as the mathematical tool to analyze the transient network properties

of the resting brain incorporating biological details and yet simplifying them into abstract concepts of signals and systems over graphs.

This thesis extends this bridge into further relating a well known computational framework known as the Reaction-Diffusion systems, especially Wilson-Cowan equations. A linear variant of Wilson-Cowan equation(s) was segmented into two components, one responsible for interactions over the space (connectome) and the other responsible for temporal patterns. The spatial and temporal components manifest into diffusion kernels and $\mathbf{\Pi}$ respectively. Moreover, this signal-system abstraction provides additional insights into the mechanism. In terms of reaction-diffusion system, $\mathbf{\Pi}$ capture the reactions at multiple spatio-temporal scales of diffusion whose diffusion is governed by the diffusion kernels. Moreover, as $\mathbf{\Pi}$ captures the initial inter-regional co-activation patterns, it also points towards the phenomenon of *modulation* even at rest.

In general, the proposed multiple kernel learning scheme has been shown to be bio-physically well motivated and tested on its performance in both static and dynamic paradigms. Apart from abstraction, the MKL model preserves some important properties like sensitivity towards input and parameter changes. The model does not overfit to the training subjects. Model performance degrades when input and parameters are changed, thus preserving subject-specificity and cohort-specificity respectively. This property has been verified by showing that the learned $\mathbf{\Pi}$s for the two age groups are very different.

As MKL was a pioneer proving itself to be a state-of-the-art model for linking structure and static function, it was extended into a broader problem of temporal dynamics constrained by the structure. Temporal patterns of the spontaneous activity repeat themselves at different frequencies in time. The patterns tend to have a definite temporal-structure [4]. In this context, there are two graphs that need to be related via signal processing tools: one is the anatomical network and the second is the temporal-network, both having their own topologies and interacting with each other. Before characterizing this relationship, prior task was to identify the temporal topology and parameterize its local density distribution. This density then could be related to the anatomy. Eigen decomposition of the graph-Laplacian holds the topology in a finite set of eigenvector-value pairs. The necessary bio-physics of these local densities, also called latent transient states, is stored into their topologies and state-specific $\mathbf{\Pi}$s.

Another important aspect, subtly present in this work, is subject-specificity of the models. Predictions are for individual subjects and not for the mean SC-FC pair of the cohort. Given the SC, the model outputs a prediction unique to the subject significantly different from the mean FC prediction. This aspect is also present in the tMKL framework as each state is a Gaussian density of non-zero size. This means that the subjects are spread around within the component, and the only way to recover those non-center points is through subject's SC. This aspect must be improved in future for many clinical applications.

Broadly, to complete such a signal processing perspective of the resting state dynamics and its relation to the anatomy, in future this framework can be used to predict the structure from the BOLD time series (FC-to-SC, the model inversion problem). An initial theoretical attempt was made by inverting the MKL model to obtain the graph-Laplacian of the structural connectivity. This model can be improvised by principally forming an optimization framework and solving it. Similar treatment can be followed for

the optimization framework of MKL. The current framework, LASSO, regresses the diffusion kernel combinations with empirical FCs to estimate $\mathbf{\Pi}$ only considering sparsity constraint. In the tMKL framework, convex optimization is solved to estimate $\mathbf{\Pi}$, but it is computationally expensive. It would be advantageous to have an iterative framework that has a higher convergence rate. Another future investigation would be to look into community structures found in each $\mathbf{\Pi}$. This might provide some insights into how the structural communities interact through the 'communities' of $\mathbf{\Pi}$ to form the functional communities.

In a nutshell, bio-physics can be abstracted out in a principled way through graph-signal-processing techniques and this thesis contributes towards this goal and beyond.

Appendix *A*

Attempts on generating HCP Data

Human Connectome Project is a huge consortium dedicated to build a network map of the human brain. This map provides minimally preprocessed datasets for structural, functional, and diffusion MRI within the healthy and diseased participant cohorts. These minimal processing pipelines over the unprocessed MRI data ensure a standard of data quality and also avoid duplication of preprocessing of unprocessed data, in anticipation investigators being less interested in the complications of preprocessing required and being more interested in direct analysis over the preprocessed HCP data. One of publicly available studies, "HCP Young Adult" dataset, is a 1206 Subjects Release which includes behavioral and 3T MR imaging data from 1206 healthy young adult participants. For our purposes, the dataset contains minimally pre-processed high-resolution data-files of both DTI and rfMRI modalities.

This dataset was attempted to be downloaded and preprocessed for use in our model. The first problem was of downloading and storing the data. HCP website recommends to use a third party web-based application that does not launch because of network proxy and port issues. The workaround was to search files in Amazon S3's HCP bucket, which has a complex directory structure. HCP provides datasets with all ranges of preprocessing done on the unprocessed data, leading to several folders. The documentation for these folders is not trivial without prior pre-processing knowledge, leading to difficulty in choosing appropriate files. The next issue to resolve was to storage of the files locally. Files for DTI are around 1.3 GB and those for the rfMRI are around 5 GB, which when processed generate connectome files are around 70 KB. Even to generate one connectome file at a time, a standard and principled procedure was needed to be followed.

Due to lack of exposure in pre-processing, we failed to process DTI because of many factors: selecting inappropriate files for the pipeline, and tweaking procedural parameters that parallelize the code for efficient run-time. The tutorial followed is in the following link : $http://mrtrix.readthedocs.io/en/latest/quantitative\_structural\_connectivity/ismrm_hcp_tutorial.html$. Original pipeline took around 15 days to run, we brought it down to 2 days and deployed the code on the server. The generated structural and functional connectomes were with the dataset acquired at Charité University, Berlin, Germany. Albeit, few HCP subjects' SC matrices were resembling those of acquired in Berlin, the HCP SC matrices were very similar with each other which is not realistic. Later it was realized that the preprocessing resolution

parameters were low which led to the observed similarity. Optimal (highest) resolution parameters in the tutorial needed to be used as the connectome though looked realistic, was not. rfMRI preprocessing is straightforward. One of the major issues was due to the misalignment of the input files leading to problems in their registration. The preprocessed voxel-wise time-series lies in the standard MNI space whereas the region-wise masks lies in the native space causing the problem of registration between native and MNI space.

Now after gaining knowledge and experience in the pre-processing literature, the correct list of files and procedures have been identified and results are verified. We hope to get the connectome matrices soon.

Related Publications

1. Surampudi, Sriniwas Govinda, Shruti Naik, Avinash Shrama, Raju Surampudi Bapi, and Dipanjan Roy. "Combining Multiscale Diffusion Kernels for Learning the Structural and Functional Brain Connectivity." bioRxiv (2016): 078766, NIPS2016 Workshop - Bits and Brains.

2. Surampudi, Sriniwas Govinda, Shruti Naik, Raju Bapi Surampudi, Viktor K. Jirsa, Avinash Sharma, and Dipanjan Roy. "Multiple Kernel Learning Model for Relating Structural and Functional Connectivity in the Brain." Scientific reports 8, no. 1 (2018): 3265.

3. Surampudi, Sriniwas Govinda, Joyneel Misra, Dipanjan Roy, Avinash Sharma, Raju Bapi. "Temporal Multiple Kernel Learning Model for Predicting Resting State FC via Characterizing fMRI Connectivity Dynamics." Under submission to Neuroimage.

Bibliography

[1] F. Abdelnour, M. Dayan, O. Devinsky, T. Thesen, and A. Raj. Functional brain connectivity is predictable from anatomic network's laplacian eigen-structure. *NeuroImage*, 172:728–739, 2018.

[2] F. Abdelnour, H. U. Voss, and A. Raj. Network diffusion accurately models the relationship between structural and functional brain connectivity networks. *Neuroimage*, 90:335–347, 2014.

[3] F. Abdelnour, H. U. Voss, and A. Raj. Network diffusion accurately models the relationship between structural and functional brain connectivity networks. *Neuroimage*, 90:335–347, 2014.

[4] E. A. Allen, E. Damaraju, S. M. Plis, E. B. Erhardt, T. Eichele, and V. D. Calhoun. Tracking whole-brain connectivity dynamics in the resting state. *Cerebral cortex*, 24(3):663–676, 2014.

[5] C. N. Angstmann, I. C. Donnelly, and B. I. Henry. Pattern formation on networks with reactions: A continuous-time random-walk approach. *Physical Review E*, 87(3):032804, 2013.

[6] S. Atasoy, I. Donnelly, and J. Pearson. Human brain networks function in connectome-specific harmonic waves. *Nature communications*, 7, 2016.

[7] A.-L. Barabási. Scale-free networks: a decade and beyond. *science*, 325(5939):412–413, 2009.

[8] A.-L. Barabási and R. Albert. Emergence of scaling in random networks. *science*, 286(5439):509–512, 1999.

[9] L. Barnett, C. L. Buckley, and S. Bullock. Neural complexity and structural connectivity. *Physical Review E*, 79(5):051914, 2009.

[10] C. O. Becker, S. Pequito, G. J. Pappas, M. B. Miller, S. T. Grafton, D. S. Bassett, and V. M. Preciado. Spectral mapping of brain functional connectivity from diffusion imaging. *Scientific reports*, 8(1):1411, 2018.

[11] T. Behrens, H. Johansen-Berg, M. Woolrich, S. Smith, C. Wheeler-Kingshott, P. Boulby, G. Barker, E. Sillery, K. Sheehan, O. Ciccarelli, et al. Non-invasive mapping of connections between human thalamus and cortex using diffusion imaging. *Nature neuroscience*, 6(7):750, 2003.

[12] T. E. Behrens, H. J. Berg, S. Jbabdi, M. F. Rushworth, and M. W. Woolrich. Probabilistic diffusion tractography with multiple fibre orientations: What can we gain? *Neuroimage*, 34(1):144–155, 2007.

[13] M. Belkin and P. Niyogi. Laplacian eigenmaps and spectral techniques for embedding and clustering. In *Advances in neural information processing systems*, pages 585–591, 2002.

[14] M. Belkin and P. Niyogi. Laplacian eigenmaps for dimensionality reduction and data representation. *Neural computation*, 15(6):1373–1396, 2003.

[15] C. M. Bishop. *Pattern Recognition and Machine Learning*. Springer-Verlag New York, 2016.

[16] B. Biswal, F. Z. Yetkin, V. M. Haughton, and J. S. Hyde. Functional connectivity in the motor cortex of resting human brain using echo-planar MRI. *Magnetic Resonance in Medicine*, 34(4):537–541, 1995.

[17] B. Biswal, F. Zerrin Yetkin, V. M. Haughton, and J. S. Hyde. Functional connectivity in the motor cortex of resting human brain using echo-planar mri. *Magnetic resonance in medicine*, 34(4):537–541, 1995.

[18] S. P. Borgatti. Centrality and network flow. *Social networks*, 27(1):55–71, 2005.

[19] S. L. Bressler and V. Menon. Large-scale brain networks in cognition: emerging methods and principles. *Trends in cognitive sciences*, 14(6):277–290, 2010.

[20] J. A. Brown, J. D. Rudie, A. Bandrowski, J. D. Van Horn, and S. Y. Bookheimer. The ucla multimodal connectivity database: a web-based platform for brain connectivity matrix sharing and analysis. *Frontiers in neuroinformatics*, 6:28, 2012.

[21] E. Bullmore and O. Sporns. Complex brain networks: graph theoretical analysis of structural and functional systems. *Nature Reviews Neuroscience*, 10(3):186, 2009.

[22] J. Cabral, M. Kringelbach, and G. Deco. Functional connectivity dynamically evolves on multiple time-scales over a static structural connectome: Models and mechanisms. *NeuroImage*, 160:84–96, 2017.

[23] J. Cabral, M. L. Kringelbach, and G. Deco. Functional graph alterations in schizophrenia: a result from a global anatomic decoupling? *Pharmacopsychiatry*, 45(S 01):S57–S64, 2012.

[24] F. R. Chung. *Spectral graph theory*, volume 92. American Mathematical Soc., 1997.

[25] G. Collin, O. Sporns, R. C. Mandl, and M. P. van den Heuvel. Structural and functional aspects relating to cost and benefit of rich club organization in the human cerebral cortex. *Cerebral cortex*, 24(9):2258–2267, 2014.

[26] D. Cordes, V. M. Haughton, K. Arfanakis, J. D. Carew, P. A. Turski, C. H. Moritz, M. A. Quigley, and M. E. Meyerand. Frequencies contributing to functional connectivity in the cerebral cortex in resting-state data. *American Journal of Neuroradiology*, 22(7):1326–1333, 2001.

[27] R. C. Craddock, G. A. James, P. E. Holtzheimer, X. P. Hu, and H. S. Mayberg. A whole brain fmri atlas generated via spatially constrained spectral clustering. *Human brain mapping*, 33(8):1914–1928, 2012.

[28] J. Damoiseaux, S. Rombouts, F. Barkhof, P. Scheltens, C. Stam, S. M. Smith, and C. Beckmann. Consistent resting-state networks across healthy subjects. *Proceedings of the national academy of sciences*, 103(37):13848–13853, 2006.

[29] M. De Luca, C. Beckmann, N. De Stefano, P. Matthews, and S. M. Smith. fmri resting state networks define distinct modes of long-distance interactions in the human brain. *Neuroimage*, 29(4):1359–1367, 2006.

[30] M. De Luca, S. Smith, N. De Stefano, A. Federico, and P. M. Matthews. Blood oxygenation level dependent contrast resting state networks are relevant to functional activity in the neocortical sensorimotor system. *Experimental brain research*, 167(4):587–594, 2005.

[31] G. Deco, V. Jirsa, A. R. McIntosh, O. Sporns, and R. Kötter. Key role of coupling, delay, and noise in resting brain fluctuations. *Proceedings of the National Academy of Sciences*, 106(25):10302–10307, 2009.

[32] G. Deco and V. K. Jirsa. Ongoing cortical activity at rest: criticality, multistability, and ghost attractors. *The Journal of Neuroscience*, 32(10):3366–3375, 2012.

[33] G. Deco, V. K. Jirsa, and A. R. McIntosh. Emerging concepts for the dynamical organization of resting-state activity in the brain. *Nature reviews. Neuroscience*, 12(1):43–56, 2011.

[34] G. Deco and M. L. Kringelbach. Great expectations: using whole-brain computational connectomics for understanding neuropsychiatric disorders. *Neuron*, 84(5):892–905, 2014.

[35] G. Deco, M. L. Kringelbach, V. K. Jirsa, and P. Ritter. The dynamics of resting fluctuations in the brain: metastability and its dynamical cortical core. *Scientific Reports*, 7(3095), 2017.

[36] G. Deco, A. Ponce-Alvarez, D. Mantini, G. L. Romani, P. Hagmann, and M. Corbetta. Resting-state functional connectivity emerges from structurally and dynamically shaped slow linear fluctuations. *Journal of Neuroscience*, 33(27):11239–11252, 2013.

[37] G. Deco, E. T. Rolls, and B. Horwitz. what and where in visual working memory: a computational neurodynamical perspective for integrating fmri and single-neuron data. *Journal of Cognitive Neuroscience*, 16(4):683–701, 2004.

[38] R. S. Desikan, F. Ségonne, B. Fischl, B. T. Quinn, B. C. Dickerson, D. Blacker, R. L. Buckner, A. M. Dale, R. P. Maguire, B. T. Hyman, et al. An automated labeling system for subdividing the human cerebral cortex on mri scans into gyral based regions of interest. *Neuroimage*, 31(3):968–980, 2006.

[39] A. Destexhe and T. J. Sejnowski. The wilson–cowan model, 36 years later. *Biological cybernetics*, 101(1):1–2, 2009.

[40] N. U. Dosenbach, D. A. Fair, F. M. Miezin, A. L. Cohen, K. K. Wenger, R. A. Dosenbach, M. D. Fox, A. Z. Snyder, J. L. Vincent, M. E. Raichle, et al. Distinct brain networks for adaptive and stable task control in humans. *Proceedings of the National Academy of Sciences*, 104(26):11073–11078, 2007.

[41] M. D. Fox, M. Corbetta, A. Z. Snyder, J. L. Vincent, and M. E. Raichle. Spontaneous neuronal activity distinguishes human dorsal and ventral attention systems. *Proceedings of the National Academy of Sciences*, 103(26):10046–10051, 2006.

[42] M. D. Fox and M. E. Raichle. Spontaneous fluctuations in brain activity observed with functional magnetic resonance imaging. *Nature reviews neuroscience*, 8(9):700, 2007.

[43] P. Fransson. How default is the default mode of brain function?: Further evidence from intrinsic bold signal fluctuations. *Neuropsychologia*, 44(14):2836–2845, 2006.

[44] L. C. Freeman. A set of measures of centrality based on betweenness. *Sociometry*, pages 35–41, 1977.

[45] K. J. Friston, L. Harrison, and W. Penny. Dynamic causal modelling. *Neuroimage*, 19(4):1273–1302, 2003.

[46] R. F. Galán. On how network architecture determines the dominant patterns of spontaneous neural activity. *PloS one*, 3(5):e2148, 2008.

[47] M. Gonen and E. Alpaydin. Multiple kernel learning algorithms. *Journal of Machine Learning Research*, 12:2211–2268, 2011.

[48] J. Goñi, M. P. van den Heuvel, A. Avena-Koenigsberger, N. V. de Mendizabal, R. F. Betzel, A. Griffa, P. Hagmann, B. Corominas-Murtra, J.-P. Thiran, and O. Sporns. Resting-brain functional connectivity predicted by analytic measures of network communication. *Proceedings of the National Academy of Sciences*, 111(2):833–838, 2014.

[49] R. Guimera and L. A. N. Amaral. Functional cartography of complex metabolic networks. *nature*, 433(7028):895, 2005.

[50] P. Hagmann, L. Cammoun, X. Gigandet, R. Meuli, C. J. Honey, V. J. Wedeen, and O. Sporns. Mapping the structural core of human cerebral cortex. *PLoS biology*, 6(7):e159, 2008.

[51] P. Hagmann, M. Kurant, X. Gigandet, P. Thiran, V. J. Wedeen, R. Meuli, and J.-P. Thiran. Mapping human whole-brain structural networks with diffusion mri. *PloS one*, 2(7):e597, 2007.

[52] G. Hahn, A. Ponce-Alvarez, C. Monier, G. Benvenuti, A. Kumar, F. Chavane, G. Deco, and Y. Frégnac. Spontaneous cortical activity is transiently poised close to criticality. *PLOS Computational Biology*, 13(5):e1005543, 2017.

[53] D. K. Hammond, P. Vandergheynst, and R. Gribonval. Wavelets on graphs via spectral graph theory. *Applied and Computational Harmonic Analysis*, 30(2):129–150, 2011.

[54] E. C. Hansen, D. Battaglia, A. Spiegler, G. Deco, and V. K. Jirsa. Functional connectivity dynamics: modeling the switching behavior of the resting state. *Neuroimage*, 105:525–535, 2015.

[55] Y. He, Z. J. Chen, and A. C. Evans. Small-world anatomical networks in the human brain revealed by cortical thickness from mri. *Cerebral cortex*, 17(10):2407–2419, 2007.

[56] R. Hindriks, M. H. Adhikari, Y. Murayama, M. Ganzetti, D. Mantini, N. K. Logothetis, and G. Deco. Can sliding-window correlations reveal dynamic functional connectivity in resting-state fmri? *Neuroimage*, 127:242–256, 2016.

[57] J. Hlinka and S. Coombes. Using computational models to relate structural and functional brain connectivity. *European Journal of Neuroscience*, 36(2):2137–2145, 2012.

[58] C. Honey, O. Sporns, L. Cammoun, X. Gigandet, J.-P. Thiran, R. Meuli, and P. Hagmann. Predicting human resting-state functional connectivity from structural connectivity. *Proceedings of the National Academy of Sciences*, 106(6):2035–2040, 2009.

[59] M. D. Humphries, K. Gurney, and T. J. Prescott. The brainstem reticular formation is a small-world, not scale-free, network. *Proceedings of the Royal Society of London B: Biological Sciences*, 273(1585):503–511, 2006.

[60] R. M. Hutchison, T. Womelsdorf, E. A. Allen, P. A. Bandettini, V. D. Calhoun, M. Corbetta, S. Della Penna, J. H. Duyn, G. H. Glover, J. Gonzalez-Castillo, et al. Dynamic functional connectivity: promise, issues, and interpretations. *Neuroimage*, 80:360–378, 2013.

[61] A. A. Ioannides. Dynamic functional connectivity. *Current opinion in neurobiology*, 17(2):161–170, 2007.

[62] J. S. Isaacson and M. Scanziani. How inhibition shapes cortical activity. *Neuron*, 72(2):231–243, 2011.

[63] H. Johansen-Berg and M. F. Rushworth. Using diffusion imaging to study human connectional anatomy. *Annual review of neuroscience*, 32:75–94, 2009.

[64] D. K. Jones, A. Simmons, S. C. Williams, and M. A. Horsfield. Non-invasive assessment of axonal fiber connectivity in the human brain via diffusion tensor mri. *Magnetic Resonance in Medicine*, 42(1):37–41, 1999.

[65] Z. P. Kilpatrick. Wilson-cowan model. *Encyclopedia of Computational Neuroscience*, pages 3159–3163, 2015.

[66] S. Kondo and T. Miura. Reaction-diffusion model as a framework for understanding biological pattern formation. *Science*, 329(5999):1616–1620, 2010.

[67] Y. Kuramoto. *Chemical oscillations, waves, and turbulence*, volume 19. Springer Science & Business Media, 2012.

[68] G. R. Lanckriet, N. Cristianini, P. Bartlett, L. E. Ghaoui, and M. I. Jordan. Learning the kernel matrix with semidefinite programming. *Journal of Machine Learning Research*, 5(Jan):27–72, 2004.

[69] V. Latora and M. Marchiori. Efficient behavior of small-world networks. *Physical review letters*, 87(19):198701, 2001.

[70] L. Lee, L. M. Harrison, and A. Mechelli. A report of the functional connectivity workshop, dusseldorf 2002. *Neuroimage*, 19(2):457–465, 2003.

[71] P. Lennie. The cost of cortical computation. *Current biology*, 13(6):493–497, 2003.

[72] A. Messé, D. Rudrauf, A. Giron, and G. Marrelec. Predicting functional connectivity from structural connectivity via computational models using mri: an extensive comparison study. *NeuroImage*, 111:65–75, 2015.

[73] S. Mori and P. van Zijl. Fiber tracking: principles and strategies–a technical review. *NMR in Biomedicine*, 15(7-8):468–480, 2002.

[74] P. Morrison. The undecidable: Basic papers on undecidable propositions, unsolvable problems and computable functions, 1965.

[75] T. T. Nakagawa, M. H. Adhikari, and G. Deco. Large-scale computational models of ongoing brain activity. *Computational Models of Brain and Behavior*, pages 425–437.

[76] T. T. Nakagawa, M. H. Adhikari, and G. Deco. Large-scale computational models of ongoing brain activity. *Computational Models of Brain and Behavior*, page 425, 2017.

[77] T. T. Nakagawa, V. K. Jirsa, A. Spiegler, A. R. McIntosh, and G. Deco. Bottom up modeling of the connectome: linking structure and function in the resting brain and their changes in aging. *Neuroimage*, 80:318–329, 2013.

[78] S. D. Newman, P. A. Carpenter, S. Varma, and M. A. Just. Frontal and parietal participation in problem solving in the tower of london: fmri and computational modeling of planning and high-level perception. *Neuropsychologia*, 41(12):1668–1682, 2003.

[79] A. Y. Ng, M. I. Jordan, and Y. Weiss. On spectral clustering: Analysis and an algorithm. In *Advances in neural information processing systems*, pages 849–856, 2002.

[80] L. Nyberg, A. R. McIntosh, R. Cabeza, L.-G. Nilsson, S. Houle, R. Habib, and E. Tulving. Network analysis of positron emission tomography regional cerebral blood flow data: ensemble inhibition during episodic memory retrieval. *Journal of Neuroscience*, 16(11):3753–3759, 1996.

[81] A. S. Pillai and V. K. Jirsa. Symmetry breaking in space-time hierarchies shapes brain dynamics and behavior. *Neuron*, 94(5):1010–1026, 2017.

[82] M. G. Preti, T. A. Bolton, and D. Van De Ville. The dynamic functional connectome: State-of-the-art and perspectives. *NeuroImage*, 160:41–54, 2017.

[83] M. E. Raichle, A. M. MacLeod, A. Z. Snyder, W. J. Powers, D. A. Gusnard, and G. L. Shulman. A default mode of brain function. *Proceedings of the National Academy of Sciences*, 98(2):676–682, 2001.

[84] M. E. Raichle and M. A. Mintun. Brain work and brain imaging. *Annu. Rev. Neurosci.*, 29:449–476, 2006.

[85] J. Richiardi, S. Achard, H. Bunke, and D. Van De Ville. Machine learning with brain graphs: Predictive modeling approaches for functional imaging in systems neuroscience. *IEEE Signal Processing Magazine*, 30(3):58–70, 2013.

[86] P. Robinson. Interrelating anatomical, effective, and functional brain connectivity using propagators and neural field theory. *Physical Review E*, 85(1):011912, 2012.

[87] M. Rubinov and O. Sporns. Complex network measures of brain connectivity: uses and interpretations. *Neuroimage*, 52(3):1059–1069, 2010.

[88] S. Ryali, K. Supekar, T. Chen, J. Kochalka, W. Cai, J. Nicholas, A. Padmanabhan, and V. Menon. Temporal dynamics and developmental maturation of salience, default and central-executive network interactions revealed by variational bayes hidden markov modeling. *PLoS Computational Biology*, 12(12):e1005138, 2016.

[89] M. L. Saggio, P. Ritter, and V. K. Jirsa. Analytical operations relate structural and functional connectivity in the brain. *PloS one*, 11(8):e0157292, 2016.

[90] M. Schirner, S. Rothmeier, V. K. Jirsa, A. R. McIntosh, and P. Ritter. An automated pipeline for constructing personalized virtual brains from multimodal neuroimaging data. *Neuroimage*, 117:343–357, 2015.

[91] M. Senden, G. Deco, M. A. de Reus, R. Goebel, and M. P. van den Heuvel. Rich club organization supports a diverse set of functional network configurations. *Neuroimage*, 96:174–182, 2014.

[92] J. Shi and J. Malik. Normalized cuts and image segmentation. *IEEE Transactions on pattern analysis and machine intelligence*, 22(8):888–905, 2000.

[93] G. L. Shulman, J. A. Fiez, M. Corbetta, R. L. Buckner, F. M. Miezin, M. E. Raichle, and S. E. Petersen. Common blood flow changes across visual tasks: Ii. decreases in cerebral cortex. *Journal of cognitive neuroscience*, 9(5):648–663, 1997.

[94] D. I. Shuman, S. K. Narang, P. Frossard, A. Ortega, and P. Vandergheynst. The emerging field of signal processing on graphs: Extending high-dimensional data analysis to networks and other irregular domains. *IEEE Signal Processing Magazine*, 30(3):83–98, 2013.

[95] S. M. Smith, M. Jenkinson, H. Johansen-Berg, D. Rueckert, T. E. Nichols, C. E. Mackay, K. E. Watkins, O. Ciccarelli, M. Z. Cader, P. M. Matthews, et al. Tract-based spatial statistics: voxelwise analysis of multi-subject diffusion data. *Neuroimage*, 31(4):1487–1505, 2006.

[96] O. Sporns. *Networks of the Brain*. MIT press, 2010.

[97] S. G. Surampudi, S. Naik, A. Shrama, R. S. Bapi, and D. Roy. Combining multiscale diffusion kernels for learning the structural and functional brain connectivity. *bioRxiv*, page 078766, 2016.

[98] S. G. Surampudi, S. Naik, R. B. Surampudi, V. K. Jirsa, A. Sharma, and D. Roy. Multiple kernel learning model for relating structural and functional connectivity in the brain. *Scientific reports*, 8(1):3265, 2018.

[99] B. Thomas Yeo, F. M. Krienen, J. Sepulcre, M. R. Sabuncu, D. Lashkari, M. Hollinshead, J. L. Roffman, J. W. Smoller, L. Zöllei, J. R. Polimeni, et al. The organization of the human cerebral cortex estimated by intrinsic functional connectivity. *Journal of neurophysiology*, 106(3):1125–1165, 2011.

[100] D. S. Tuch, T. G. Reese, M. R. Wiegell, and V. J. Wedeen. Diffusion mri of complex neural architecture. *Neuron*, 40(5):885–895, 2003.

[101] A. M. Turing. The chemical basis of morphogenesis. *Bulletin of mathematical biology*, 52(1-2):153–197, 1990.

[102] V. G. van de Ven, E. Formisano, D. Prvulovic, C. H. Roeder, and D. E. Linden. Functional connectivity as revealed by spatial independent component analysis of fmri measurements during rest. *Human brain mapping*, 22(3):165–178, 2004.

[103] M. P. Van Den Heuvel and O. Sporns. Rich-club organization of the human connectome. *Journal of Neuroscience*, 31(44):15775–15786, 2011.

[104] A. Vattikonda, B. R. Surampudi, A. Banerjee, G. Deco, and D. Roy. Does the regulation of local excitation–inhibition balance aid in recovery of functional connectivity? a computational account. *NeuroImage*, 2016.

[105] K. Vemuri and B. R. Surampudi. An exploratory investigation of functional network connectivity of empathy and default mode networks in a free-viewing task. *Brain Connectivity*, 5(6):384–400, 2015.

[106] P. E. Vértes, A. F. Alexander-Bloch, N. Gogtay, J. N. Giedd, J. L. Rapoport, and E. T. Bullmore. Simple models of human brain functional networks. *Proceedings of the National Academy of Sciences*, 109(15):5868–5873, 2012.

[107] J. L. Vincent, A. Z. Snyder, M. D. Fox, B. J. Shannon, J. R. Andrews, M. E. Raichle, and R. L. Buckner. Coherent spontaneous activity identifies a hippocampal-parietal memory network. *Journal of neurophysiology*, 96(6):3517–3531, 2006.

[108] U. Von Luxburg. A tutorial on spectral clustering. *Statistics and computing*, 17(4):395–416, 2007.

[109] D. J. Watts and S. H. Strogatz. Collective dynamics of small-worldnetworks. *nature*, 393(6684):440, 1998.

[110] V. J. Wedeen, P. Hagmann, W.-Y. I. Tseng, T. G. Reese, and R. M. Weisskoff. Mapping complex tissue architecture with diffusion spectrum magnetic resonance imaging. *Magnetic resonance in medicine*, 54(6):1377–1386, 2005.

[111] H. R. Wilson and J. D. Cowan. Excitatory and inhibitory interactions in localized populations of model neurons. *Biophysical journal*, 12(1):1–24, 1972.

[112] H. R. Wilson and J. D. Cowan. A mathematical theory of the functional dynamics of cortical and thalamic nervous tissue. *Biological Cybernetics*, 13(2):55–80, 1973.

[113] M. Xia, J. Wang, and Y. He. Brainnet viewer: a network visualization tool for human brain connectomics. *PloS one*, 8(7):e68910, 2013.